12-2019

Evaluation of Fracture Principles in Asphalt Concrete Utilizing the SC(B) Geometry

Airam Marlee Morales Vega
University of Arkansas, Fayetteville

Citation

Morales Vega, A. M. (2019). Evaluation of Fracture Principles in Asphalt Concrete Utilizing the SC(B) Geometry. *Theses and Dissertations* Retrieved from https://scholarworks.uark.edu/etd/3477

Evaluation of Fracture Principles in Asphalt Concrete Utilizing the SC(B) Geometry

A dissertation submitted in partial fulfillment
of the requirements for the degree of
Doctor of Philosophy in Engineering

by

Airam Marlee Morales Vega
Technological University of Panama
Bachelor of Science in Civil Engineering, 2013
Technological University OTEIMA
Master in Education, 2014
University of Arkansas
Master of Science in Civil Engineering, 2016

December 2019
University of Arkansas

This dissertation is approved for recommendation to the Graduate Council.

Andrew F. Braham Ph.D.
Dissertation Director

Kevin D. Hall Ph.D.
Committee Member

Zahid Hossain Ph.D.
Committee Member

Gary Prinz Ph.D.
Committee Member

Abstract

Since cracking is one of the principal distresses to be considered in asphalt concrete, multiple fracture tests and geometries have been used to quantify cracking resistance. One of the most popular geometries that have been used in fracture tests is the Semi-Circular bend (SC(B)). However, for this geometry, most of the fracture test methods use different parameters such as thickness, testing temperatures, and loading rates. Thus, the purpose of this research was first to evaluate fracture energy by performing a ruggedness test based on ASTM E1169. Then, to apply fracture mechanics concepts to evaluate three specimen thicknesses (25, 50, and 100 mm) and three notch configurations (rectangular, semi-circular and fatigue pre-cracked). Also, with the selected thickness and notch configuration, the concept of time-temperature superposition was applied to characterize cracking in asphalt concrete by using four testing temperatures (-12, 0, 12, and 25 ˚C) and five loading rates (0.03, 0.5, 1.0, 30.0, 50.0 mm/min). The results showed that from the ruggedness test, the fracture energy is significantly influenced by the testing temperatures but not the loading rate. When applying fracture mechanics theories, the selected thickness and notch configuration selected were 50 mm and semi-circular, respectively. Finally, when using time-temperature superposition to plot fracture energy versus the loading rate to mimic the steps followed in the Dynamic Modulus |E*|, a typical sigmoidal was not obtained. However, a parabolic curve was found to better describe the cracking behavior. Utilizing this analysis, the concept of local fracture energy was defined as the peak fracture energy from each set of testing temperatures and loading rates. Using the local fracture energy, the global fracture energy was built and defined as the peak fracture energy from all the testing temperatures plotted. In conclusion, when properly applying fracture mechanics properties and the new concepts of local and global fracture energy,

these give a new perspective of how the cracking behavior can be quantified at different testing temperatures independently of the loading rate.

Acknowledgements

First, I would like to thank God Almighty for giving me the strength in hard times, my parents José Morales and María Vega, my husband Edgar Fuentes, and my brother, Josimar Morales, who supported me since the moment I decided to study abroad, without your support this would not have been possible.

I would like to thank my advisor, Dr. Andrew Braham, for including me in his research group “The Road Hogs” and allowing me to obtain my Ph.D. Also, for his help, support and guidance during these five years of graduate school.

Thanks to my committee members: Dr. Kevin Hall, Dr. Gary Prinz, and Dr. Zahid Hossain for their advice and guidance. Thanks to all my professors at the University of Arkansas for your knowledge and for making unforgettable my professional journey at Fayetteville, Arkansas.

Special thanks to my colleagues: Sadie Casillas, Shu Yang, Elvis Castillo, Erica Bowie, Logan Kiihnl, Matthew Johnson, and Chase Henrichs who worked with me during these five years where we shared our thoughts and knowledge but also build a wonderful friendship.

I would like to thank the people that help me with the fabrication of the asphalt samples in the asphalt laboratory: Tanner Poor, Chase Allison, Anabella Monterroso, David Olatunji, Kaley Collins, and Pedro Diaz. Thank you so much for your amazing job. Also, thanks to the research technologists: David Peachee and Mark Kuss, who always helped me when having issues at the lab.

Finally, thanks to the government of Panama who allowed me to accomplish my graduate studies with a scholarship through the program IFARHU-UTP.

Dedication

To my parents José Morales and María Vega, and my brother Josimar Morales for their support and words of encouragement.

To my husband Edgar Fuentes, for his unconditional love and for always supporting me in my decisions.

And finally, to the memory of my grandfather José Vega, who passed away before the completion of this thesis, but he always encouraged me to keep going with my studies.

Table of Content

Chapter 1 Introduction to Semi-Circular Bend Test Methods in Asphalt Concrete 1
1.1 Introduction to Cracking in Asphalt Concrete 1
1.2 Fracture Mechanics 3
1.3 Fracture Mechanics in Asphalt Concrete 4
1.3.1 Asphalt Geometries used in Fracture Tests 4
1.3.2 SC(B) Test Methods 6
1.4 The Current Problem: Fracture Mechanics vs. AASHTO Procedures............................... 11
1.4.1 Thickness 12
1.4.2 Notch Configuration 14
1.5 Viscoelastic Behavior of Asphalt Concrete 16
1.5.1 Loading Rate and Testing Temperature 17
1.5.2 Time-Temperature Superposition.. 18
1.5.3 Cracking Resistance Master Curve Development 24
1.6 Dissertation Objectives 26
1.7 Dissertation Organization.. 26
1.8 References 27
Chapter 2 Ruggedness Test of Fracture Energy and Flexibility Index using Semi- Circular Bend Test 32
Abstract 32
2.1 Introduction 33
2.1.1 Test Methods 33
2.1.1.1 Fracture Indices... 34
2.1.1.2 Ruggedness Test (ASTM E1169) 35
2.1.2 Objectives 37
2.2 Materials and Methods 37
2.2.1 Materials 37
2.2.2 Test Methods 38
2.2.2.1 Fracture Energy... 38
2.2.2.2 Flexibility Index:... 39
2.2.2.3 Factors and Levels 40
2.3 Results and Discussion.. 43
2.3.1 Fracture Energy and Flexibility Index 46

2.4 Conclusions 48
2.5 References 49
Chapter 3 Evaluation of Semi-Circular Bend (SC(B)) Geometric Properties for Asphalt Concrete Testing*[1] 52
Abstract 52
3.1 Introduction 53
  3.1.1 Thickness 54
  3.1.2 Notch Configuration 60
  3.1.3 Research Objective 63
3.2 Materials and Methods 63
  3.2.1 Materials 63
  3.2.2 Test Methods 64
3.3 Results and Discussion 67
  3.3.1 Thickness 68
    3.3.1.1 Plane Strain 69
    3.3.1.2 Representative Volume Element 71
  3.3.2 Notch Configuration 72
    3.3.2.1 Crack Initiation 72
  3.3.3 ANOVA Analysis 76
3.4 Conclusion 78
3.5 References 79
Chapter 4 Developing a Master Curve for SC(B) test to Evaluate Cracking Resistance using Fracture Energy versus Loading Rate*[2] 81
Abstract 81
4.1 Introduction 82
  4.1.1 Time-Temperature Superposition Principle 84
  4.1.2 Research Objective 85
4.2 Materials and Methods 86
  4.2.1 Materials 86
  4.2.2 Test Methods 87
4.3 Results and Discussion 89
  4.3.1 Fracture Energy 89
  4.3.2 Master Curves 91
  4.3.3 Local and Global Fracture Energy 94

    - 4.3.3.1 Local Fracture Energy 96
    - 4.3.3.2 Global Fracture Energy 100
  - 4.4 ANOVA Analysis 104
  - 4.5 Conclusions 106
  - 4.6 References 107

Chapter 5 Conclusions and Recommendations 109
  - 5.1 Review of chapter objectives 109
  - 5.2 Conclusions 110
  - 5.3 Recommendations 112

Appendix A Tables from Chapter 3 114
Appendix B Tables, Equations and Figures from Chapter 4 117

List of Tables

Table 1.1 Semi-Circular Geometry Methods 10
Table 2.1 Asphalt Binder Content 38
Table 2.2 Experimental Matrix 38
Table 2.3 Factors considered for the ruggedness test 41
Table 2.4 Recommended design up to 7 factors from ASTM E1169 42
Table 2.5 Calculations of the main effect for fracture energy 44
Table 2.6 Statistics results for main effects for fracture energy 45
Table 2.7 Calculation of the main effect for flexibility index 46
Table 2.8 Statistics results for main effects for flexibility index 46
Table 3.1 Experimental Matrix 64
Table 3.2 Fracture Energy Results 67
Table 3.3 Plane Strain Thickness Calculations at -24 ˚C 70
Table 3.4 Plane Strain Thickness Calculations at -12 ˚C 71
Table 3.5 Initial and Final Crack Degree for -12°C 74
Table 3.6 Initial and Final Crack Degree for -24°C 75
Table 3.7 ANOVA Factorial Design 77
Table 4.1 Asphalt Binder Content 87
Table 4.2 Experimental Matrix 89
Table 4.3 Local maximum values from fitted parabola (LR is loading rate) 98
Table 4.4 Maximum Global Fracture Energy values from fitted parabolas 104
Table 4.5 P-Value Summary of ANOVA for Fracture Energy 105
Table 4.6 Analysis of Variance of Fracture Energy for Loading Rate at different temperatures 106
Table A.1 Plane Strain Thickness Calculations at - 24°C 114
Table A.2 Plane Strain Thickness Calculations at - 12°C 115
Table A.3 General Factorial Design Matrix 116
Table B.1 Initial Fracture Energy values to fit parabolas 117
Table B.2 Analysis of Variance of Fracture Energy at -12 °C 126
Table B.3 Analysis of Variance of Fracture Energy at 0 °C 127
Table B.4 Analysis of Variance of Fracture Energy at 12 °C 127
Table B.5 Analysis of Variance of Fracture Energy at 25 °C 127
Table B.6 Analysis of Variance for Fracture Energy at -12 ºC, 9.5 mm PG 64-22 128
Table B.7 Analysis of Variance for Fracture Energy at -12 ºC, 9.5 mm PG 76-22 128
Table B.8 Analysis of Variance for Fracture Energy at -12 ºC, 25 mm PG 64-22 128
Table B.9 Analysis of Variance for Fracture Energy at -12 ºC, 25 mm PG 76-22 128
Table B.10 Analysis of Variance for Fracture Energy at 0 ºC, 9.5 mm PG 64-22 128
Table B.11 Analysis of Variance for Fracture Energy at 0 ºC, 9.5 mm PG 76-22 129
Table B.12 Analysis of Variance for Fracture Energy at 0 ºC, 25 mm PG 64-22 129
Table B.13 Analysis of Variance for Fracture Energy at 0 ºC, 25 mm PG 76-22 129
Table B.14 Analysis of Variance for Fracture Energy at 12 ºC, 9.5 mm PG 64-22 129
Table B.15 Analysis of Variance for Fracture Energy at 12 ºC, 9.5 mm PG 76-22 129
Table B.16 Analysis of Variance for Fracture Energy at 12 ºC, 25 mm PG 64-22 130

Table B.17 Analysis of Variance for Fracture Energy at 12 ºC, 25 mm PG 76-22 130
Table B.18 Analysis of Variance for Fracture Energy at 25 ºC, 9.5 mm PG 64-22 130
Table B.19 Analysis of Variance for Fracture Energy at 25 ºC, 9.5 mm PG 76-22 130
Table B.20 Analysis of Variance for Fracture Energy at 25 ºC, 25 mm PG 64-22 130
Table B.21 Analysis of Variance for Fracture Energy at 25 ºC, 25 mm PG 76-22 131

List of Figures

Figure 1.1 Cracking Distress 2
Figure 1.2 Fracture Specimen geometries for asphalt concrete 6
Figure 1.3 SC(B) Test Setup 7
Figure 1.4 Load-displacement curve for Fracture Energy and Flexibility Index 8
Figure 1.5 Fénix Test Setup (Perez-Jimenez et al., 2010) 9
Figure 1.6 Notch Configurations 15
Figure 1.7 Data Shifting to Construct a Master Curve 20
Figure 1.8 Shift Factor versus Temperature 20
Figure 1.9 Sigmoidal Function (Pellinen et al., 2003) 21
Figure 1.10 Progression of Master Curve Development (Smith et al., 2019) 23
Figure 2.1 Load-displacement curve for flexibility index and fracture energy calculations 40
Figure 3.1 Fracture Toughness vs. Thickness (NDT Resource Center, 2014) 56
Figure 3.2 Plastic Zone Size for Plane Strain 57
Figure 3.3 TRVE sizes before using Coefficient of Variation (Kim et al., 2010) 59
Figure 3.4 TRVE sizes using Coefficient of Variation (Kim et al., 2010) 59
Figure 3.5 Schematic representation of the cohesive zone (Paulino et al., 2004) 62
Figure 3.6 Notch Configurations 62
Figure 3.7 SC(B) Sample Fabrication 65
Figure 3.8 Load vs. displacement plot for notch configurations 66
Figure 3.9 Fracture Energy Results 68
Figure 3.10 Crack Propagation for each notch configuration 73
Figure 3.11 Crack Propagation Scheme 74
Figure 3.12 Initial and Final Crack at -12°C 74
Figure 3.13 Initial and Final Crack at -24°C 75
Figure 4.1 Loading Rate Effect (Aragão et al., 2012) 83
Figure 4.2 Influence of Loading Rate (Li et al., 2010) 84
Figure 4.3 Effects of 9.5 mm fracture energy at different temperatures 91
Figure 4.4 Effects of 25 mm fracture energy at different temperatures 91
Figure 4.5 Fracture Energy Master Curve for 9.5 mm PG 64-22 using Time-Temperature Superposition at a 25 ˚C Reference Temperature 93
Figure 4.6 Fracture Energy Master Curve for 9.5 mm PG 76-22 using Time-Temperature Superposition at a -12 ˚C Reference Temperature 93
Figure 4.7 Fracture Energy Master Curve for 25mm using Time-Temperature Superposition at a -12 ˚C Reference Temperature 94
Figure 4.8 Effects on 9.5 mm fracture energy at different temperatures 95
Figure 4.9 Effects on 25 mm fracture energy at different temperatures 96
Figure 4.10 Local Fracture Energy Parabolas 97
Figure 4.11 Binder Type and NMAS influence on Fracture Energy from 99
Figure 4.12 Binder Type and NMAS influence on Loading Rate from 100
Figure 4.13 9.5 mm NMAS Global Parabola 101
Figure 4.14 25 mm NMAS Global Parabola 101

Figure 4.15 Global Fracture Energy Parabolas 103
Figure B.1 Local Parabola for 9.5 mm PG 64-22 119
Figure B.2 Local Parabola for 9.5 mm PG 76-22 121
Figure B.3 Local Parabola for 25 mm PG 64-22 123
Figure B.4 Local Parabola for 25 mm PG 76-22 125

Chapter 1 Introduction to Semi-Circular Bend Test Methods in Asphalt Concrete

1.1 Introduction to Cracking in Asphalt Concrete

Asphalt concrete is commonly used in roads because it is easily constructed at a very low cost in comparison with other materials. Also, asphalt concrete provides a smooth and safe quality riding surface (Wagoner *et al.,* 2005c). Every year, a significant amount of money is invested in designing, constructing, and maintaining asphalt concrete, due to external factors such as traffic loads, environmental conditions, construction practices, and material properties that can deteriorate asphalt concrete and form cracks (Behbahani, 2013).

There are several types of cracking distress in asphalt concrete: fatigue cracking, block cracking, edge cracking, longitudinal cracking, joint reflection cracking, slippage cracking, and transverse cracking (Miller *et al.*, 2003; ASTM, 2016). Fatigue cracks (Fig. 1.1a), which are typically created by traffic loading, have been historically thought to form at the bottom of the asphalt layer, where the tensile stress and strain are the highest, and propagate upward to the surface with the continuous repetition of traffic (Khattak, 2013). However, several studies report that load-related fatigue cracks are also formed “top-down,” which starts at the surface of the pavement and continues to the bottom (Harmelink *et al.*, 2008; Park *et al.,* 2013). Consequently, it is necessary to rehabilitate the pavement when the riding surface is unacceptable (Mobasher *et al.,* 1997). Block cracks are cracks interconnected, which divide the surface into rectangular pieces. This type of crack is not related to traffic loads as fatigue is, but it is caused by daily temperature cycling. Edge cracks are parallel to the outer edge of the pavement. A frost-weakened base causes edge cracking and the traffic load can worsen the crack (ASTM, 2016). Longitudinal cracks are linear cracks and parallel to the pavement centerline. This type of crack may be caused by daily temperature cycling and reflective cracking from PCC slabs underneath asphalt concrete

(Miller *et al.*, 2003). Joint reflection cracking is a crack formed in asphalt concrete overlays because of PCC slabs. This type of crack is also not caused by traffic loads but by thermal movement of the PCC underneath asphalt concrete. Slippage cracks, which are caused by braking or turning wheels, are half-moon shaped cracks that are transversal to traffic direction (ASTM, 2016). Finally, transverse cracks (Fig. 1.1b), which frequently result from low temperatures or reflective cracking, are linear cracks that are perpendicular to traffic flow and may cause unstable crack growth (Hoare, 2000).

a) Fatigue Crack **b) Transverse Crack**

Figure 1.1 Cracking Distress

To enhance the design and structure of asphalt concrete, fracture mechanics has been used since the 1960s to evaluate cracking behavior. Asphalt concrete becomes more brittle, and it is more susceptible to cracking at low temperatures and older mixture age (Moavenzadeh, 1967; Li *et al.*, 2010). Fracture mechanics examine how cracks initiate and propagate in different materials. There are important theories in fracture mechanics, such as linear elastic and nonlinear, which help to quantify and predict cracks in asphalt concrete (Mobasher *et al.*, 1997).

In the past decades, there have been multiple test methods to obtain fracture resistance in asphalt concrete to have a better understanding of cracking. Most tests place a discontinuity such a notch in a test specimen to accelerate the testing sequence. When a notch is present in a sample, a stress concentration forms at the notch tip. Cracks form and propagate when energy stored in the notch region exceeds the energy necessary to create new surfaces. Single-edge notched beam [SE(B)], semi-circular bend test (SC(B)), and disk-shaped compaction tension [DC(T)] are examples of fracture tests used to obtain fracture energy (Wagoner *et al.,* 2005b).

1.2 Fracture Mechanics

Fracture mechanics can be applied to multiple fields, such as civil, biomedical, electrical, mechanical, and aerospace engineering. Through the years, fracture mechanics has been evolving from one field to the other through the development of multiple theories and equations to solve cracking problems in aircraft, buildings, ships, pavements, and bones. In 1921, Griffith, one of the pioneers in fracture mechanics, proposed a theory of brittle fracture and energy release rate (Griffith, 1921). In 1948, Irwin and Orowan proposed modifications to Griffith's theory to account for small-scale plastic energy in fracture (Irwin, 1948). In 1957, Irwin proposed an approach that was based on stress analysis of cracks, and as a result, Irwin made comparisons between energy-based approaches and stress analysis (Irwin, 1957; Saxena, 1998).

In the 1960s, linear elastic fracture mechanics (LEFM) was established (Anderson, 2005). Linear elastic only occurs when inelastic deformations are not considerable. Linear elastic theories consider two parameters: strain energy release rate and stress intensity. Stress intensity measures the intensity of the stress field in the region of the crack in an open mode, and it depends on the stress applied, the structure geometry, and the crack length. When a material fails by unstable crack propagation, the strain energy release rate is equal to the fracture toughness of the material K_{IC}. Linear elastic theories have been used in asphalt concrete to compare the load repetitions to fatigue failure. However, this method of measurement has produced a lot of questions about the results obtained using the linear elastic theories (Mobasher *et al.,* 1997; Anderson, 2005).

Nonlinear fracture mechanics are applied for the materials that have nonlinear deformations: elastic-plastic and visco-elastic. From the 1970s to the 1980s, elastic-plastic theories began to be analyzed. From the 1980s to date, time-dependent fracture mechanics were developed (Saxena, 1998). Some parameters for nonlinear fracture mechanics were proposed: the compliance approach and the R-Curve approach. The compliance approach defines the crack instability condition, whereas the R-Curve approach evaluates the fracture toughness at different crack lengths (Yang *et al*., 2013).

1.3 Fracture Mechanics in Asphalt Concrete

1.3.1 Asphalt Geometries used in Fracture Tests

To investigate crack growth behavior, some studies have used multiple test geometries. For asphalt concrete, the test specimen should have a simple geometry and a loading setup (Behbahani, 2013). At the beginning of fracture testing research, the most common geometry used was the single-edge notched beam [SE(B)] (Fig. 1.2a) (Majidzadeh *et al.,* 1971; Mobasher *et al.,* 1997; Wagoner *et al.,* 2005a; Hakimzadeh, 2015; Yang *et al.,* 2013), which has a rectangular shape. Some advantages of this geometry are that after crack initiation allows for a stable crack, mixed modes can be performed such as shear and tensile opening. However, this beam configuration had some disadvantages because it is difficult to compare laboratory results with field conditions due to its irregular shape. In other words, it is not as common to extract samples from roads that have a beam shape, as it is a circular core barrel, which is the preferred method of sample extraction. As a result, an alternate shape geometry named semi-circular bend [SC(B)] was developed (Fig. 1.2b) (Mobasher *et al.,* 1997; Molenaar et al., 2002; Marasteanu *et al.,* 2007; Mohammad *et al.,* 2008; Arabani *et al.,* 2008; Li *et al*., 2010; Kim *et al.,* 2012; Yang *et al.,* 2013), and it can be used to investigate fracture energy and fracture toughness of asphalt concrete at low temperatures and predicts fatigue cracking. Some of the advantages of an SC(B) geometry are that it can be easily obtained from field specimens; two specimens can be used from one core, and; it is a simple three-point bending loading.

A disk-shaped geometry was also introduced due to limitations with previous geometries. The disk-shaped compaction tension [DC(T)] (Fig. 1.2c) (Lee, 1999; Wagoner *et al.*, 2005c, Braham *et al.*, 2007; Kim *et al*., 2009; Marasteanu *et al.*, 2012), which is used to determine fracture properties at low temperatures, has a near disk shape and was first designed with two holes close to the edges. However, more than 50% of the samples had the propensity to break at the point of loading, making the samples inefficient in collecting fracture data. Thus, the placement of the holes was modified to the center of the sample. As the SC(B) geometry, the DC(T) can be easily obtained from field specimens and it has a standard fracture test configuration. Finally, a dog-bone direct tension (DBDT) (Fig. 1.2d) was proposed (Roque *et al.*, 2009; Koh *et al.*, 2009) to improve concepts from IDT, which was used to assess tensile measurements. DBDT geometry has some advantages: the failure limits can be measured on the failure plane since they are already known; samples can be built by coring the opposite side of the sample, and; stress concentrations at the end of the specimen are not critical as in IDT. Beyond the basic shape of the test, there is still a need to find an appropriate thickness from the geometries to obtain a more fundamentally sound result from the fracture tests.

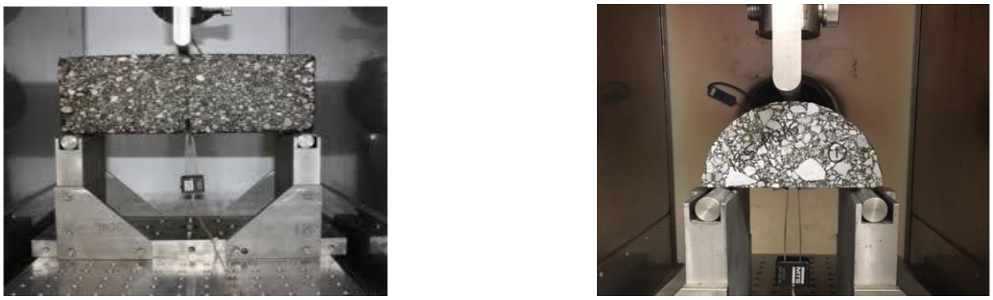

a) Single Notched Beam (Braham *et al.*, 2016) **b) Semi-Circular Bend**

c) Disk-Shaped Compaction Test (Braham *et al.*, 2016) **d) Dog-Bone Direct Tension (Koh *et al.*, 2009)**

Figure 1.2 Fracture Specimen geometries for asphalt concrete

1.3.2 SC(B) Test Methods

Since this research is going to be based on SC(B) geometry, further investigation was made into the SC(B) geometry and methods that apply fracture mechanics principles were introduced, which are: SC(B) test at low temperatures, Illinois Flexibility Index Test (I-FIT) Protocol, the Louisiana Transportation Research Center (LTRC) Method and the Fénix Test. Specifically, the Fénix Test is not a bend test as the previous tests mentioned, but it uses an SC(B) geometry, which is the main focus of this study.

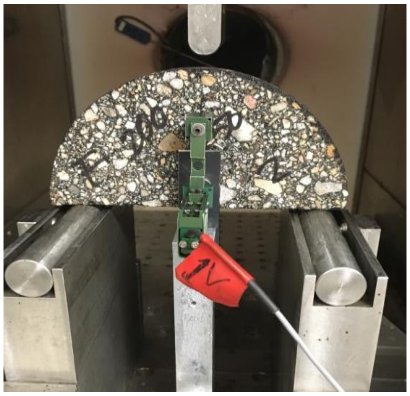

Figure 1.3 SC(B) Test Setup

AASHTO TP 105 specification is the semi-circular bend (SC(B)) fracture test (Fig. 1.3), which determines the fracture energy and fracture toughness at low temperatures of asphalt concrete with a semi-circular geometry. The samples tested according to specification are cut in half with a 150 mm diameter, a 25 mm thickness, and a 15 mm notch length and 1.5 mm wide. A load is applied to the sample, and the External Load Line Displacement (LLD) and the Crack Mouth Opening Displacement (CMOD) are recorded. Tests are run with different low temperatures: one half is tested 10 ˚C above the Performance Grade (PG) lower limit of the asphalt binder used for the mixture, and the other half is tested 2 ˚C below the PG lower limit. The loading rate applied is 0.03 mm/min or 0.0005 mm/s. For conditioning, the sample has to be in a temperature-controlled chamber for 2 ± 0.5 hours. For test performance, after conditioning the sample, the sample is situated on the test fixture and the clip gage is attached. The analysis is made when the load applied to the specimen starts increasing from 0.3 kN to a peak load. Then the load starts to decrease and it is stopped when the load starts dropping below 0.5 kN, or when the crack mouth opening displacement limit is reached, whichever occurs first. Once the test is completed, the fracture energy is calculated by taking the area under the load/external LLD curve, and dividing this value by the area of the ligament (AASHTO, 2013), as shown in Figure 1.4. Higher fracture energy indicates lower cracking susceptibility in the field (Al-Qadi *et al*., 2015).

The I-FIT Method utilizes AASHTO Specification TP 124-16, and it was developed for SC(B) geometry with a 50 mm thickness, at an intermediate temperature of 25 °C, and a loading rate of 50 mm/min with a controlled load-line displacement (LLD). Fracture energy and flexibility index (FI) are the two parameters obtained from this test procedure. The flexibility index, which is calculated with the slope at the inflection point (Figure 1.4), is defined as the index that characterizes the damage resistance of asphalt concrete (AASHTO, 2016). The advantage of this calculation is that FI can be related to fracture mechanics and crack growth rate. Therefore, the FI region, where it is calculated, represents the zone close to the notch tip, which is the place that cracks develop while testing (Ozer *et al*., 2017). A higher flexibility index indicates lower cracking susceptibility in the field (Al-Qadi *et al*., 2015).

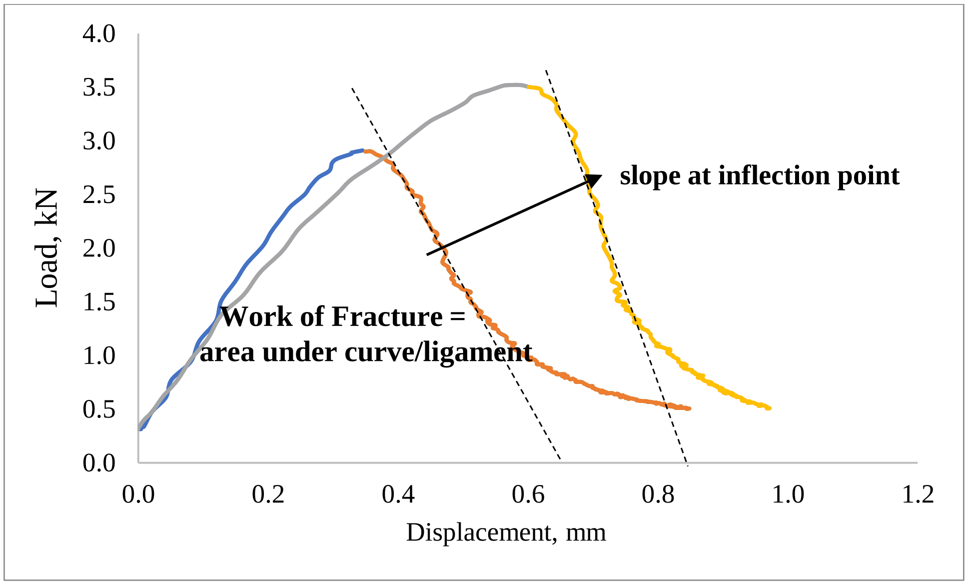

Figure 1.4 Load-displacement curve for Fracture Energy and Flexibility Index

The LTRC Method used an SC(B) geometry and intends to collect J_c, which is the critical strain energy release rate, to assess crack resistance of asphalt concrete. The test is performed with a thickness of 57 mm, at an intermediate temperature of 25 °C, with a loading rate of 0.5 mm/min. Additionally, the test is performed with different notch depths to capture critical J_c. The three-notch depth tested were: 25.4, 31.8, and 38 mm. These values were selected based on a/r_a, which is the radio of the notch depth to the radius of the specimen, between 0.50 and 0.75 (Cooper III *et al.,* 2016; Braham *et al.,* 2016). These methods look to evaluate beyond asphalt concrete due to the use of polymers, chemicals and recycled asphalt pavement (RAP) that are mixed with the asphalt binder to enhance performance on the roads.

Figure 1.5 Fénix Test Setup (Perez-Jimenez et al., 2010)

Finally, the Fénix Test is performed in an SC(B) geometry, and it is used to calculate the dissipated energy during the formation of cracks to evaluate the cracking resistance. The thickness of the geometry is 63.5 mm with a 6 mm-deep notch, at low and intermediate temperatures of -10 ºC, 5 ºC, and 20 ºC, with a loading rate of 1 mm/min. Unlike the other tests, the Fénix Test is not a bend test method and it is performed in tension. For instance, two steel plates are glued to the specimen and then attached to a loading platen to make a small rotation, as shown in Figure 1.5

(Perez-Jimenez *et al.*, 2010; Perez Madrigal *et al.*, 2017). Table 1.1 summarizes some of the semi-circular geometry methods used in asphalt concrete.

Table 1.1 Semi-Circular Geometry Methods

Method	Reference	Purpose	Thickness	Test Temperature	Loading Rate
Determining the Fracture Energy of Asphalt Concrete Using the Semi-Circular Bend Geometry (SCB)	AASHTO TP 105-13	Determine fracture energy, fracture toughness, and stiffness.	25 mm	low temperature -24ºC, -12 ºC	0.03 mm/min
Illinois Flexibility Index Test (I-FIT) Protocol	AASHTO TP 124-16	Determine fracture energy and flexibility index (FI)	50 mm	intermediate temperature 25 ºC	50 mm/min
Louisiana Transportation Research Center (LTRC) Method	Cooper III *et al.*, 2016	Collect critical strain energy release rate (J_c)	57 mm	intermediate temperature 25 ºC	0.5 mm/min
Fénix Test	Perez-Jimenez *et al.*, 2010	Calculate dissipated energy during to estimate cracking resistance	63.5 mm	Low and intermediate temperature -10 ºC, 5 ºC, and 20 ºC	1 mm/min

For asphalt concrete, there is a concern that current asphalt concrete fracture tests and test results do not give an accurate fracture characterization (Wagoner *et al.*, 2005b). Several procedures need to be evaluated such as AASHTO TP 105 and AASHTO TP 124. AASHTO TP 105 is the standard method of test for determining the fracture energy of asphalt concrete using the semicircular bend geometry (SC(B)). This method covers the determination of fracture energy, fracture toughness, and stiffness in asphalt concrete, and is usually used at low temperatures (AASHTO, 2013). Likewise, AASHTO TP 124 is the standard method of test for determining the fracture potential of asphalt mixtures using the flexibility index test (FIT) (AASHTO, 2016). This method covers the determination of flexibility index and fracture energy. In this research, the

LTRC Method and the Fénix Test are not going to be considered since the notch depth is not a variable and only three-point bending tests are going to be performed.

In this dissertation, Chapter 2 will cover a statistical analysis called Ruggedness Test based on the ASTM E1169 specification, in which the asphalt indices: fracture energy and flexibility index are going to be evaluated using common factors in asphalt concrete such as nominal maximum aggregate size (NMAS), binder type, loading rate, and testing temperature. The results obtained will set the experimental matrix for the following chapters depending on the sensitivity and influence of the factors into the indices.

1.4 The Current Problem: Fracture Mechanics vs. AASHTO Procedures

Cracking is one of the major distresses of asphalt concrete. Cracks forms from multiple factors: traffic loads, construction, and environmental conditions. To address this issue, fracture mechanics has been applied to multiple methods using different geometries.

In 1984, Chong and Kurrupu proposed the semi-circular bend. The geometry of the SC(B) is a half-disk with a rectangular notch that makes an angle with the center axle of the disc. The authors perceived that the fracture toughness that was obtained with the SC(B) test did not depend on the thickness and crack length. Therefore, SC(B) can be used for mode I and II stress intensity factors depending on the angle of the notch. For instance, for a mode I the angle with the center axle of the disc is zero (Marasteanu *et al.,* 2007). In 1994, Lim et al., researched specimen size and asphalt concrete. The results obtained were the following: the fracture toughness was not dependent on the thickness and diameter of the specimen, a notch length did not seem to influence fracture toughness, and a notch length between 3 mm and 80% of the radius of the specimen gave valid values of K_{Ic} (Lim *et al.,* 1994).

AASHTO TP 105 and AASHTO TP 124 are standard methods that determine the fracture energy of asphalt concrete using semi-circular bend geometry. Additionally, AASHTO TP 124 determines a flexibility index. AASHTO TP 105 test procedure method has some limitations with fracture results obtained. There is a need for continuing investigating applying fundamental fracture theory to the test methods. Therefore, Chapter 3 from this study will investigate two components of AASHTO TP 105 and AASHTO TP 124: sample thickness and notch configuration.

1.4.1 Thickness

In material testing, the specimen size is an important factor to consider. Equally, in asphalt concrete, the specimen dimension is significant due to the maximum aggregate size because it may not be much smaller than the specimen size. The specimen dimension can be related to the representative volume element (RVE). The RVE is defined as the smallest volume large enough where the material characteristics are constant. Some disadvantages of using specimens smaller than RVE are more samples required for testing, and in the test procedure the process of averaging ignores biases that could result in large errors; therefore, using specimens of larger RVE is recommended (Kim, 2009).

Furthermore, the thickness used for SC(B) geometry in AASHTO TP 105 is 25 mm and for AASHTO TP 124 is 50 mm. In 1999, Roque et al. used a 25 mm thickness in Superpave IDT specimens to study the crack growth rate. The authors mentioned that at 25 mm, the plane stress conditions are met for indirect tension tests. As a result, the stress intensity factor can be obtained with thin specimens. In 2004, following Roque et al. thickness for the IDT test, Li et al. (2004) proposed to use a 25 mm thickness for SC(B) geometry to satisfy the plane stress which is required to calculate the fracture toughness. In Li et al., (2004) study, a 50-mm thickness was also proposed, but it was discarded after doing a finite element analysis to the stress and strain state for both 25 mm and 50 mm thicknesses. The thickness of the sample not only balances plane stress versus plane strain conditions but also influences whether RVE is being achieved.

From the perspective of fracture mechanics, the sample thickness has to do with plane stress vs. plane strain concepts, which are related to fracture toughness. Fracture toughness is defined as the resistance of a material to crack extension. To determine fracture toughness, the critical stress-intensity factor (K_{Ic}) is measured. Thin sections are related to plane stress where plain strain conditions do not exist. When increasing the thickness, the properties are shifted to a mixed-mode and then to plane strain and at some point, it becomes constant into the plane strain. A Mode I fracture, which is the most common mode to be considered as K_I, is defined as the condition where the crack plane is normal to the largest tensile loading direction. The specimen size gives different K_I value, but when the plane strain is reached, a constant value of K_I is obtained and it becomes K_{Ic}, which is the true material property (Anderson, 2015; NDT Education, 2014, ASTM, 2006).

To summarize, the thickness of 25 mm in AASHTO TP 105 is proposed based on plane stress (Li *et al.*, 2004). However, AASHTO TP 124 proposes a thickness of 50 mm. In asphalt concrete, the importance of RVE is that if using smaller specimen may lead to errors in the testing and more tests need to be completed to obtain accurate results (Kim, 2009). The issue with the thickness of 25 mm for the SC(B) geometry is that may not demonstrate the RVE of the material. Therefore, this research in Chapter 3 evaluates three different thicknesses such as 25 mm, and 50 mm, which have been proposed in several SC(B) methods, and 100 mm to give an upper range of the thicknesses previously used.

1.4.2 Notch Configuration

Fracture mechanics describes the principles of crack initiation, crack propagation and failure. Cracks usually initiate in some stress concentration points such as notches. For crack extension, the strain energy release rate (*G*) is the origin of the total energy. When the critical G value (G_{Ic}) is achieved, crack propagation occurs in an instability condition. Therefore, R-Curve, which is a compliance approach, is used through the strain energy release rate (*G*). For a specimen with a notch that experiences infinitesimal crack growth under displacement conditions or constant load, the response before and after the crack propagation can be observed in the change of the load-deformation response (Mobasher *et al.*, 1997).

Additionally, the notch configuration used for AASHTO TP 105 and AASHTO TP 124 is a rectangular notch (Fig. 1.6a). Asphalt concrete fracture tests are usually performed on notched specimens. The purpose of the notch is to concentrate the stress so the crack can initiate and propagate. However, the size and the shape of the notch may have some influences on the results of the tests (Roque *et al.*, 1999). Researchers have found some issues with rectangular configuration because the crack is forced to occur at the top corners of the notch, which makes the crack form in a specific location, giving difficulty in obtaining accurate fracture properties. The "dog-bone" direct tension configuration has advantages: failure can be measured on the failure plane, so it is known a priori; the DBDT geometry allows that the stress concentrations at the end of the specimen are less critical; and the cracks can be formed anywhere, instead of being forced as a rectangular notch. Therefore, to simulate the "dog-bone" direct tension configuration, a semi-circular notch configuration was proposed (Fig. 1.6b) (Koh *et al.*, 2009; Porter, 2016). Fracture testing in metals follows ASTM E399, which uses a fatigue pre-cracked that must be introduced to mimic a natural crack in the specimen in a reproducible way to obtain plane-strain fracture toughness (Souza *et al.*, 2012). The purpose of using fatigue pre-cracking (Fig. 1.6c) is to create a sharp crack that is unaffected by the procedure of the pre-cracking. The importance of the sharp crack is to provide the validity of K_{Ic} which depends on the condition on the crack. The tip of the fatigue crack should have an adequate size to ensure plane strain conditions. This pre-crack can be made by applying a cyclic loading at the notched specimen and it is recommended to be performed at the same environmental conditions that are going to be tested (ASTM, 2006).

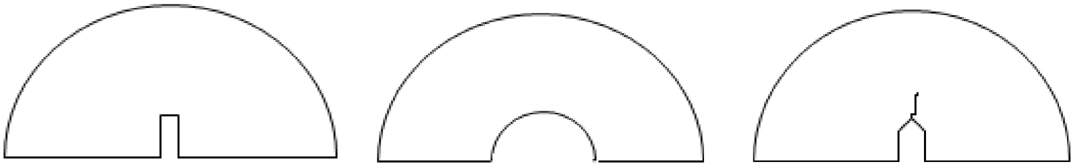

a) Rectangular Notch b) Semi-circular notch c) Fatigue Pre-cracked notch

Figure 1.6 Notch Configurations

As seen in previous research done with the geometries, except the DBDT, used to test fracture in asphalt concrete, a rectangular notch had ruled. The issue with the rectangular notch is that the crack is forced to occur at one of the tips of the mechanically inserted notch. However, no "tips" occur in pavement in the field. Thus, obtaining accurate fracture properties may be difficult because of the crack forming in a specific location (Roque *et al.*, 1999). In metals, fatigue pre-cracked notches are used to validate the K_{Ic} property by creating a sharp-crack in a specimen to ensure plain-strain conditions (ASTM, 2006). According to Broek, specimens must present a fatigue crack. For the cracking to occur at the right place, there is a starter notch. In the case of thick members, the cracks start at a corner, which can be compared to a rectangular notch configuration. However, this behavior is not ideal for a standard test because the cracking behavior results are irreproducible and curved crack front. Consequently, this behavior can be avoided with the implementation of a chevron notch because this notch forces the crack initiation in the center, which increases the probability of having a straight crack front. Another advantage is that the crack starts immediately with the cycling process (Broek, 1986). For crack initiation, notches or stress concentrations are the sites where fatigue loading occurs. Fatigue pre-cracked specimens experience fatigue growth rate indistinctly from the shape of the notch. However, when the crack starts from a notch, the propagation of the crack is higher due to the accumulation of fatigue damage at the tip where the crack starts (Rozumek *et al.,* 2006). From Porter's (2016) study, the semi-circular notch provided different results for crack initiation and propagation; and the fatigue pre-cracked notch gave only results on crack propagation, compared to the rectangular notch.

This preliminary work shows the need to better understand the influence of thickness and notch configurations on the SC(B) geometry in asphalt concrete. Therefore, Chapter 3 will examine the evaluation of the thickness of SC(B) geometry from AASHTO TP105 and AASHTO TP124 testing methods based on the plane stress vs. plane strain (thinner to thicker) and RVE. Also, the assessment of a rectangular notch configuration from AASHTO procedures, by comparing fracture energy results from semi-circular notch configuration, which mimic the DBDT, and a fatigue notch configuration used in ASTM E399 will be made. The focus of this chapter will be to apply fracture mechanics concepts in asphalt concrete in the thicknesses and the notch configurations evaluated.

1.5 Viscoelastic Behavior of Asphalt Concrete

One of the most challenging tasks of asphalt concrete is the prediction of a long-term service prediction due to the influence of traffic loading and environmental conditions. Since asphalt concrete is a viscoelastic material, the performance and behavior can be affected by loading rate, temperature, aging, and moisture. Consequently, several models have been made to capture the effects of these factors in asphalt concrete (Kim, 2009). Researchers have focused on the study of the interaction between loading rate and testing temperature by developing a fracture test that applies combinations of low temperature or intermediate temperature with slow or fast loading rates. However, a more comprehensive study is needed in which testing temperatures from low to intermediate and loading rates from slower to faster are used. Thus, Chapter 4 will apply this concept of viscoelastic behavior to evaluate testing temperatures and loading rates used in SC(B) test methods. Also, this application will help to understand the time-temperature superposition in asphalt concrete by plotting fracture energy versus a reduced loading rate.

1.5.1 Loading Rate and Testing Temperature

The interaction between loading rate and testing temperature in asphalt concrete has been investigated when performing fracture tests. In 1967, Moavenzadeh researched the effects of the parameters of loading rate, temperature, and depth of notch on asphalt concrete. The results obtained showed that the strain energy release rate is a property of asphalt concrete and it can vary from one material to another, which was obtained from the theory of brittle fracture. After testing asphalt concrete under static and repeated conditions, in either direct or indirect tensile strength measurements, the results showed that parameters, such as temperature, loading rate, thickness, and stiffness have some effect on the mode of failure and tensile strength of asphalt concrete. The mode of failure is related to brittle materials at low temperatures and high loading rates. In contrast, if the temperature increases or the loading rate decreases, the mode of failure is related to ductile materials.

Molenaar et al. (2000) used four temperatures: 25 °C, 15 °C, 0 °C and -10 °C, and three loading rates which were 0.005 mm/s, 0.05 mm/s, 0.5 mm/s. The following conclusions were given from the study: $K_{I,}$ for a deformation rate of 0.05 mm/s if the diameter is greater than 220 mm, it is almost independent of the specimen diameter and the diameter must be greater than 150 mm for a deformation rate of 0.005 mm/s. Li et al. (2005) tested using 0.0005 mm/s, which is the loading rate specified in AASHTO TP 105, to control the crack mouth opening displacement (CMOD) and used three temperatures: -20 °C, -30 °C, and -40 °C. The results obtained demonstrated that both fracture energy and fracture toughness are useful for low-temperature performance and both parameters are temperature dependent.

1.5.2 Time-Temperature Superposition

Asphalt is a viscoelastic material, so its behavior changes depending on the temperature. The time-temperature superposition principle (TTSP) is used to predict the behavior of materials with time-dependent behavior. This concept assumes that the time and temperature are interconnected and similar (Starkova *et al.*, 2009). The dynamic modulus |E*| test, which is a material characterization test, provides information about the dynamic modulus |E*| of the material tested with different temperatures (-10 ºC to 54 ºC) and frequencies (0.1 Hz to 25 Hz). With the results obtained, a master curve is plotted, |E*| versus reduced frequency. The purpose of the master curve is to compare the performance of different asphalt concrete mixtures (Clyne *et al.*, 2003; AASHTO, 2013). To build a master curve, the principle of time-temperature superposition is applied. This creates a master curve, where different reduced frequencies overlap. Therefore, different frequencies at different temperatures produce the same dynamic modulus. When calculating fracture energy from the fracture test, just low temperatures and one loading rate are considered in AASHTO TP 105 and intermediate temperature and one loading rate in AASHTO TP 124. Since asphalt is a viscoelastic material, there is limited information in fracture analysis on testing at different temperatures and loading rates. In theory, different loading rates at different temperatures should produce the same fracture energy. If this is true, then a master curve of fracture energy could be created based on a “reduced” loading rate. Therefore, the loading rate based on the temperatures applied in the AASHTO procedures must be examined.

To calculate the shift factors, different theoretical models can be used for the shift functions. One of the most popular to calculate the horizontal shift factor is the Williams-Landel-Ferry (WLF) equation (Eq. 1.1). (Pacheco *et al.*, 2015). Other models used to describe the behavior of asphalt concrete are pure power law, generalized power law, the Prony series, and the Standard-Linear-Solid model.

$$\log aT = \frac{-C_1(T-T_o)}{C_2(T-T_o)} \qquad \text{(Eq. 1.1)}$$

Where,

aT = shift factor

C_1 *and* C_2 = constants that depends on the material

T = Temperature (ºC)

T_o= Reference temperature (ºC)

Alternatively, AASHTO TP 62 proposes a sigmoidal function to construct master curves for Uniaxial Dynamic Modulus |E*|. To build this master curve, the WLF equation is not used; nonetheless, the shift factors are determined to shift a dynamic modulus curve by giving an initial trial value and then applying the error minimization between the predicted |E*| and the actual |E*| for fitting the curve (Chebab *et al.*, 2002). The Dynamic Modulus |E*| is calculated using Equation 1.2 For instance, Figure 1.7a shows a dynamic modulus |E*| plotted versus frequency without shifting the data. However, Figure 1.7b shows the same data from Figure 1.7a but after shifting the function. The reference temperature used for the shifting is 21 °C. Figure 1.8 is a plot of the shift factor versus testing temperature.

$$\log|E^*| = \delta + \frac{\alpha}{1+e^{\beta-\gamma\log\xi}} \tag{Eq. 1.2}$$

Where:

$|E^*|$ = cyclic modulus,

ξ = reduced frequency,

δ = minimum modulus value,

α = span of modulus values, and

β, γ = shape parameters.

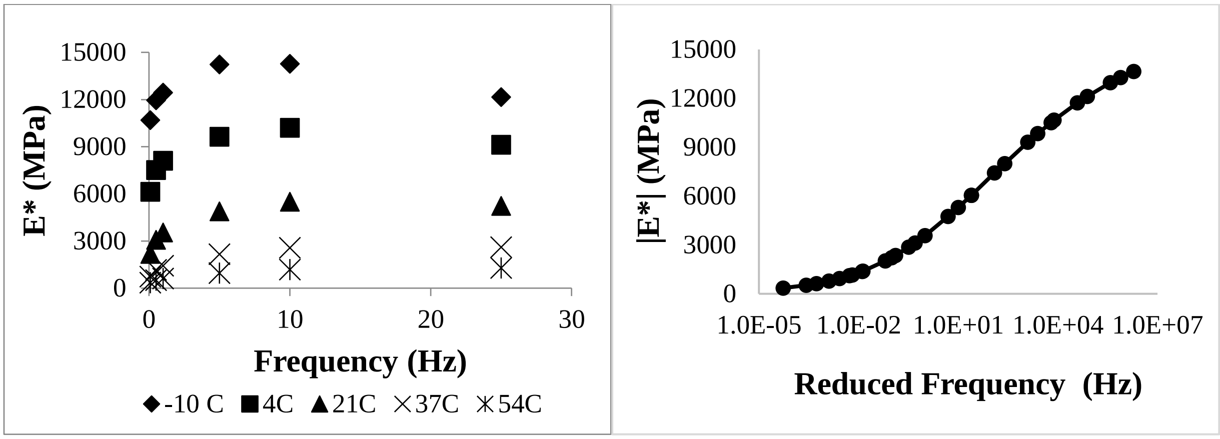

a) Data before Shifting **b) Data after Shifting**

Figure 1.7 Data Shifting to Construct a Master Curve

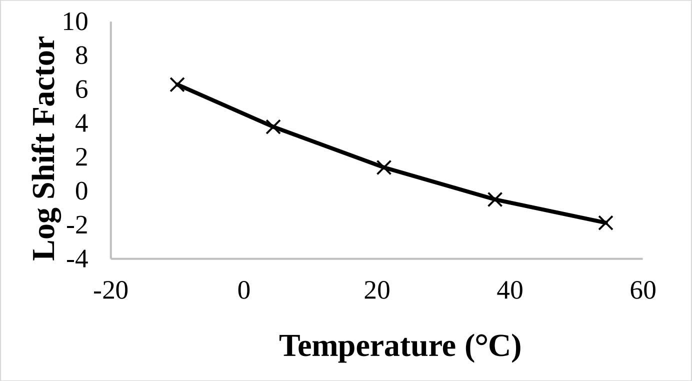

Figure 1.8 Shift Factor versus Temperature

Asphalt concrete has used polynomial fitting functions instead of a single polynomial model to shift the asphalt mix data because of a polynomial swing at low and high temperatures. The sigmoidal function is represented as an S-shaped curve that is delineated by four parameters which define the characteristics of the shape. These parameters are the upper asymptote, the lower asymptote, the maximum slope, and the inflection point where there is a change from increasing slope to decreasing slope. Figure 1.9 shows the fitting parameters in the sigmoidal function, where the shape parameter γ influences in the steepness of the function, and β is the turning point of the horizontal position. Because of the behavior of the mix, a sigmoidal function is used for fitting the cyclic data. The maximum stiffness of the mix, which is dependent on the binder stiffness at cold temperatures, is represented by the upper part of the sigmoidal function that approaches asymptotically. However, at high temperatures, the aggregate has a higher influence than the asphalt binder which leads to an equilibrium value that depends on the aggregate gradation. Therefore, the sigmoidal function describes the physical behavior of the asphalt mixture in the temperature range tested (Pellinen *et al.,* 2003; Yang *et al.,* 2017).

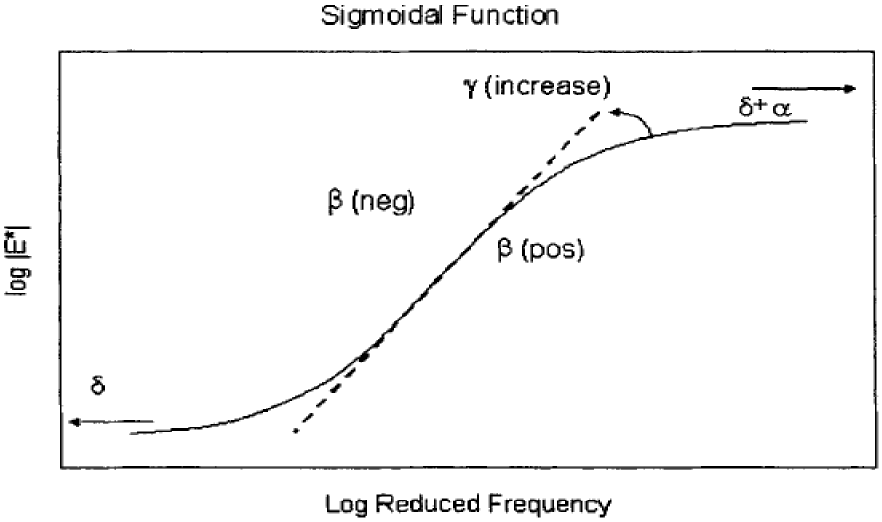

Figure 1.9 Sigmoidal Function (Pellinen et al., 2003)

In 2017, Yang et al. tested three test methods: Dynamic Modulus |E*|, IDT Dynamic Modulus, and Torsion Bar |G*| and created a master curve for each of them following the AASHTO R 62-13 specification. In this study, the authors proposed modifications to the traditional master curve development AASHTO R 62 because the master curve obtained was not describing the S-shape with the initial values specified for the shifting factors. Consequently, one of the recommendations was to provide a method to calculate the initial guesses for fitting the curves rather than having a fixed initial guess as the AASHTO R 62-13 specification gives. Another recommendation was to establish a minimum and maximum value on the log shift factors which are used to create the reduced frequencies (Yang *et al.,* 2017). In 2019, another research performed by Smith et al. tested the same three methods: Dynamic Modulus |E*|, IDT Dynamic Modulus, and Torsion Bar |G*| to compare laboratory tests results versus the concept of RVE found through grayscale analysis techniques. In this study, both the initial coefficients and the minimum and maximum value of the log shift factors recommendations provided by Yang et al. were applied when building the master curves as seen in Figure 1.10. For instance, Figure 1.10a shows the master curve developed using the initial guesses from the AASHTO R 62 specification which does not represent the expected sigmoidal function. When applying the initial guess utilizing the equations recommended by Yang et al., a more defined S-shape is obtained in Figure 1.10b, but the isothermal curves were highly spaced. Therefore, the second recommendation of placing a minimum and maximum value on the log shift factors was applied in Figure 1.10c, where a sigmoidal S-shape is described and the isothermal curves are not highly spaced (Smith *et al.,* 2019). Both studies are an example of how building a master curve can be challenging when the desired result is not obtained, but at the same time when enhancing the concepts provided in the specifications can give a stronger description of the results.

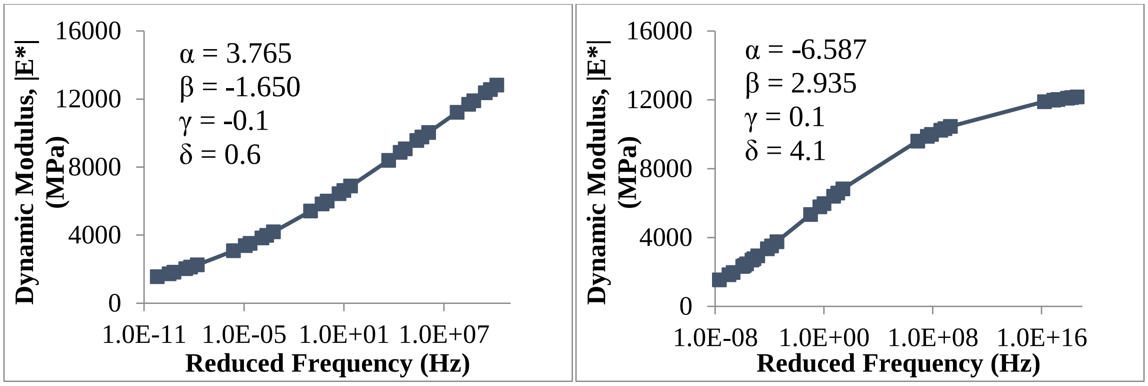

a) Developed according to AASHTO R 62 b) Developed using Yang et al. initial guess

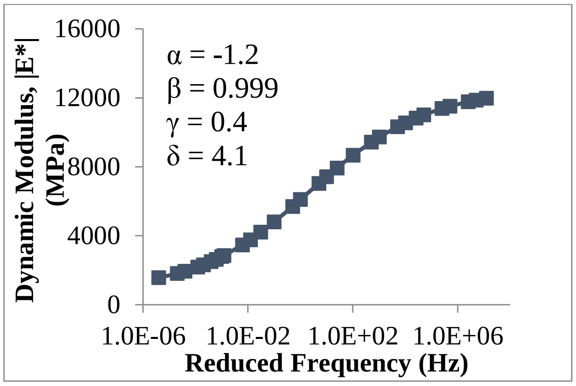

c) Restricting minimum and maximum on -10 and 54 °C shift factors

Figure 1.10 Progression of Master Curve Development (Smith et al., 2019)

As mentioned, asphalt concrete is a viscoelastic material, so building a master curve to represent the cracking resistance could be beneficial to understand its behavior in different temperatures versus loading rates applied. Having a master curve for fracture analysis can give a better understanding of the cracks developed on asphalt material. When calculating fracture energy from the fracture test, only low temperatures and one loading rate are considered in AASHTO TP 105; intermediate temperatures and one loading rate are considered in AASHTO TP 124. Since asphalt is a viscoelastic material, in fracture analysis there is limited information on testing in different loading rates and temperatures. With the temperatures and loading rates from actual fracture tests, a fracture master curve could be developed. This curve will be similar in concept to a dynamic modulus master curve but will plot fracture energy versus loading rate. Using these methods combined, the aim is to enhance specifications that use an SC(B) geometry to ensure that fundamental fracture theory is being appropriately applied.

1.5.3 Cracking Resistance Master Curve Development

In this dissertation, Chapter 4 will first evaluate fracture energy using low and intermediate temperature with different loading rates. Then, it will explore the feasibility of constructing a fracture energy master curve, which would plot fracture energy versus a reduced loading rate.

The cracking resistance master curve was created based on AASHTO R 62 for dynamic modulus |E*| by applying the concept of time-temperature superposition. To develop the cracking master curve, the following steps were followed:

Step 1: Prepare a summary table from the fracture energy (G_f) obtained from the SC(B) test from each temperature and loading rate combination. Then calculate the average of the fracture energy (G_f) from the three replicates from each temperature and loading rate.

Step 2: Calculate the coefficient of variation of the fracture energy (G_f). This information will provide a better idea of the difference between the values obtained in the three replicates.

Step 3: To describe the shape of the master curve, sigmoidal parameters are used in the Equation 1.3:

$$\log |G_f| = \delta + \frac{\alpha}{1+e^{\beta+\gamma \log l_r}} \tag{Eq. 1.3}$$

Where,

$|G_f|$ = fracture energy, J/m^2

$\delta, \alpha, \beta, \gamma$ = fitting parameters, and

l_r = reduced loading rate, mm/min, which is expressed in Equation 1.4.

$$log\ l_r = \log l + a_1(T_R - T) + a_2\,(T_R - T)^2 \tag{Eq. 1.4}$$

Where,

$\mathrm{f_r}$ = reduced loading rate at the reference temperature,

f = the loading rate at the test temperature

$\mathrm{a_1, a_2}$ = the fitting coefficients, and

$\mathrm{T_R}$ = the reference temperature, ℃

The reference temperature for this method is usually at the medium temperature. However, the master curves were shifted at -12 ˚C because with the other temperatures the curves were not smooth.

Step 4: Then the sum of the squared errors (Eq 1.5) is calculated between the average fracture energy (G_f) obtained in Step 1 and the values of the predicted fracture energy from Equation 1.3. The following equation shows the calculation that should be performed:

$$\sum error^2 = \sum_1^n (log \mid \hat{G}_f|_i - \log|G_f|_i)^2 \qquad \text{(Eq. 1.5)}$$

Where,

$\sum error^2$ = sum of squared errors

n = number of temperatures/loading rates combinations

$\log \mid \hat{G}_f|_i$ = fracture energy value predicted by Equation 1.3

$\log|G_f|_i$ = logarithm of the average measured in Step 1

Step 5: The Excel solver function is used to minimize the sum of the squared error to have a better-fitted curve. The following coefficients were applied for fitting the curves: $\alpha = 3.0, \beta = 1.0, \delta = 0.5, \gamma = -0.5, \mathrm{a_1} = 0.10$, and $\mathrm{a_2} = 0.00010$.

Step 6: After minimizing the error, the master curve is plotted with the fracture energy data against the loading rate on a log scale by shifting the reference temperature to -12 ˚C. The same steps can be followed to create master curves for other cracking indices.

Finally, to implement this research, the fracture energy will be calculated following the testing procedures of AASHTO TP 105 only. However, different temperatures, loading rates, thicknesses, and notch configurations will be considered from fracture test methods performed in the field to evaluate the fracture energy influenced by these factors.

1.6 Dissertation Objectives

The objectives for the proposed research are to:

- Evaluate the interactions of asphalt properties: nominal maximum aggregate size, binder type, loading rate, and temperature, through ASTM E1169 ruggedness test and compare fracture energy vs. flexibility index results.
- Enhance the test procedure of AASHTO TP 105 by assessing that fundamental fracture mechanics concepts are applied to the specification by evaluating three thicknesses: 25, 50 and 100 mm, three notch configurations of the SC(B) geometry: rectangular, semi-circular, and fatigue pre-cracked, and two low temperatures of the SC(B) methods: -12 and -24 °C.
- Evaluate the fracture behavior by performing AASHTO TP 105 test at four different testing temperatures (-12, 0, 12, 25 ˚C), five loading rates (0.03, 0.5, 1.0, 30.0, and 50.0 mm/min), two binder types (PG 64-22 and PG 76-22), and two NMAS (9.5 and 25 mm).
- Investigate fracture behavior by plotting fracture energy versus loading rate at different temperatures to have a better understanding of the time-temperature superposition principles that is applied in asphalt concrete because of its viscoelastic properties.

1.7 Dissertation Organization

This dissertation is organized with the following chapters. First, Chapter 2 is about the fracture energy and flexibility index calculated from AASHTO TP105 using different factors such as NMAS, binder type, loading rate, and temperatures, by applying a ruggedness test. These results obtained helped to set the experimental matrix for the next chapters. Second, Chapter 3 is an evaluation of thicknesses and notch configurations from the SC(B)'s geometry. In this chapter, only low temperatures and one binder type were tested to calculate fracture energy. Additionally, Chapter 4 is an assessment of fracture energy calculated at low and intermediate temperatures with different loading rates and two binder types, by keeping constant the thickness and notch configuration, which were obtained from the Chapter 3 results. The objective of this chapter is to apply the concept of time-temperature superposition by plotting fracture energy versus loading rate to describe the cracking behavior in asphalt concrete. Finally, Chapter 5 gives conclusions to enhance SC(B) specifications and recommendations for future research.

1.8 References

AASHTO (2013). Standard Method of Test for Determining the Fracture Energy of Asphalt Mixtures Using the Semicircular Bend Geometry (SCB). TP 105-13. Washington D.C. Fracture Toughness of Asphalt Concrete Materials. *13th International Conference on Fracture.*

AASHTO (2013). Standard Practice for Developing Dynamic Modulus Master Curves for Asphalt Mixtures. *R 62-13.* Washington D.C.

AASHTO (2016). Determining the Fracture Potential of Asphalt Mixtures Using the Flexibility Index Test (FIT). TP 124-16. Washington D.C.

Al-Qadi, I., Ozer, H., Lambros, J., Khatib, A., Singhvi, P., Khan, T., Rivera-Perez, J., Doll, B. (2015). Testing Protocols to Ensure Performance of High Asphalt Binder Replacement Mixes Using RAP and RAS. Report FHWA-ICT-15-017.

Anderson, T. (2005). *Fracture Mechanics Fundamentals and Applications*. Boca Raton, FL: Taylor & Francis.

Arabani, M., Ferdowsi, B. (2008). Evaluating the Semi-Circular Bending Test for HMA Mixtures. *International Journal of Engineering A: Basics.* 22 (1), pp. 47-58.

ASTM (2006). Standard Test Method for Linear-Elastic Plane-Strain Fracture Toughness K_{1C} of Metallic Materials. E399-06. West Conshohocken, PA.

ASTM (2016). Standard Practice for Roads and Parking Lots Pavement Condition Index Surveys. D-6433-16. West Conshohocken, PA.

Behbahani, H., Aliha, M., Fazaeli, H., Rezaeifar, M. (2013). Effect of Characteristics Specifications on Fracture Toughness of Asphalt Concrete Materials. *13th International Conference on Fracture.*

Braham, A., Buttlar, W., Marasteanu, M. (2007). Effect of Binder Type, Aggregate, and Mixture Composition of Fracture Energy of Hot-Mix Asphalt in Cold Climates. *Transportation Research Record: Journal of the Transportation Research Board, No. 2001.* pp. 102-109.

Braham, A., Underwood, S. (2016). State of the Art and Practice in Fatigue Cracking Evaluation of Asphalt Concrete Pavements.

Broek, D. (1986). *Elementary Engineering Fracture Mechanics.* Hingham, MA: Kluwer Academic Publishers.

Chebab, G., Kim, Y.R, Schapery, R., Witczak, M., Bonaquist, R. (2002). Time-Temperature Superposition Principle for Asphalt Concrete with Growing Damage in Tension State. *Association of Asphalt Pavement Technologists: Proceedings of the Technical Sessions,* 71, pp. 559-593.

Chong, K.P. Kuruppu, M.D. (1984). New Specimen for Fracture Toughness Determination for Rock and Other Materials. *International Journal of Fracture.* 26, R52-R62.

Clyne, T., Li, X., Marasteanu, M., Skok, E. (2003). Dynamic and Resilient Modulus of Mn/DOT Asphalt Mixtures. Report MN/RC – 2003-09.

Cooper III, S., King, W., Kabir, S. (2016). Testing and Analysis of LWT and SCB Properties of Asphalt Concrete Mixtures. *Louisiana Department of Transportation and Development.* FHWA-LA-536.

Griffith, A. (1921). The Phenomena of Rupture and Flow in Solids. *Philosophical Transactions of the Royal Society of London. Series A, Containing Papers of a Mathematical or Physical Character.* 221, pp. 163-198.

Harmelink, D., Shuler, S., Aschenbrener, T. (2008). Top-Down Cracking in Asphalt Pavements: Causes, Effects, and Cures. *Journal of Transportation Engineering,* 134(1), pp. 1-6.

Hakimzadeh, S. (2015). Single-Edge Notched Disk Fracture Test for Asphalt Concrete. *Journal of Testing Evaluation.* 44(1), pp. 565-573.

Hoare, T., Hesp, S. (2000). Low-Temperature Fracture Testing of Asphalt Binders. *Transportation Research Record: Journal of the Transportation Research Board, No 1728,* Washington, D.C, pp 36-42.

Irwin. G.R. (1948). Fracture Dynamics. *Fracturing of Metals, American Society for Metal.* Cleveland: OH. pp. 147-166.

Irwin, G.R. (1957). Analysis of Stresses and Strains Near the End of a Crack Traversing a Plate. *Journal of Applied Mechanics-Transactions of the ASME.* 24, pp. 361-364.

Khattak, M., Baladi, G. (2013). Analysis of Fatigue and Fracture of Hot Mix Asphalt Mixtures. *Hindawi Publishing Corporation.*

Kim, Y.R. (2009). *Modeling of Asphalt Concrete.* Reston, VA: McGraw Hill.

Kim, M., Buttlar, W., Baek, J., Al-Qadi, I. (2009). Field and Laboratory Evaluation of Fracture Resistance of Illinois Hot-Mix Asphalt Overlay Mixtures. *Transportation Research Record: Journal of the Transportation Research Board, No. 2127.* pp. 146-154.

Kim, M., Mohammad, L., Elseifi, M. (2012). Characterization of Fracture Properties of Asphalt Mixtures as Measured by Semicircular Bend Test and Indirect Tension Test. *Transportation Research Record: Journal of the Transportation Research Board, No. 2296.* pp. 115-124.

Koh, C. Lopp, G., Roque, R. (2009). Development of a Dog-Bone Direct Tension Test (DBDT) for Asphalt Concrete. *Advanced Testing and Characterization of Bituminous Materials.* pp. 585-596.

Lee, K. Soupharath, N., Shukla, A., Franco, C., Manning, F. (1999). Rheological and Mechanical Properties of Blended Asphalt Containing Recycled Asphalt Pavement Binders. *Asphalt Paving Technology.* 68, pp. 89-128.

Li, X., Marasteanu, M.O., Dai, S., and Lukanen, E. (2005). Prediction of Low Temperature Crack Spacing in Asphalt Pavements. *Proceedings, the 7th International Conference on the Bearing Capacity of Roads, Railways and Airfields,* Trondheim, Norway.

Li, X., Marasteanu, M. (2004). Evaluation of the Low Temperature Fracture Resistance of Asphalt Mixtures Using the Semi-Circular Bend Test. *Asphalt Paving Technology: Association of Asphalt Paving Technologists- Proceedings of the Technical Sessions.* 73, pp. 401-426.

Li, X., Marasteanu, M., Kvasnak, A., Bausano, J., Williams, C., Worel, B. (2010). Factors Study in Low-Temperature Fracture Resistance of Asphalt Concrete. *Journal of Materials in Civil Engineering ASCE.* 22(2), pp 145-152.

Lim, I. L., Johnston, I.W., Choi, S.K. and Boland, J.N. (1994). Fracture Testing of a Soft Rock with Semi-Circular Specimens Under Three Point Bending. Part1-Mode I. *International Journal of Rock Mechanics, Mining Science.* 31, pp. 199-212.

Majidzadeh, K., Kaufman, E., Ramsamooj, D. (1971). Application of Fracture Mechanics in the Analysis of Pavement Fatigue. *Journal of the Association of Asphalt Paving Technologists.* 40, pp. 227-246.

Marasteanu, M. Moon, K., Teshale, E., Falchetto, A., Turos, M. (2012). Investigation of Low Temperature Cracking in Asphalt Pavements National Pooled Fund Study- Phase II. *Minnesota Department of Transportation*, MN/RC 2012-23.

Marasteanu, M., Zofka, A., Turos, M., Li, X., Velasquez, R., Li, X. (2007). Investigation of Low Temperature Cracking in Asphalt Pavements, National Pooled Fund Study 776. *Minnesota Department of Transportation*, MN/RC 2007-43.

Miller, J., Bellinger, W. (2003). Distress Identification Manual for the Long-Term Pavement Performance Program. FHWA-RD-03-031.

Moavenzadeh, F. (1967). Asphalt Fracture. *Proceedings of the Association of Asphalt Paving Technologists.* 36, pp. 51-79.

Mobasher, B., Mamlouk, M., Lin, H. (1997). Evaluation of Crack Propagation Properties of Asphalt Mixtures. *Journal of Transportation Engineering.* 123(5), pp 405-413.

Mohammad, L., Kabir, M., Saadeh, S. (2008). Evaluation of Fracture Properties of Hot Mix Asphalt. *CRC Press*. pp. 427-436.

Molenaar, J. M. M. and Molenaar, A.A.A. (2000) "Fracture Toughness of Asphalt in the Semi-Circular Bend Test", *Proceedings, 2nd Eurasphalt and Eurobitume Congress*, Barcelona, Spain.

Molenaar, A., Scarpas, A., Liu, X., Erkens, S. (2002). Semi-Circular Bending Test; Simple but useful? *Asphalt paving Technology: Association of Asphalt Paving Technologists-Proceedings of the Technical Sessions.* 71, pp. 794-815.

NDT Resource Center. (2014). https://www.nde-ed.org

Orowan, E. (1948). Fracture and Strength of Solids. *Reports on Progress in Physics*. 12, pp. 185-232.

Ozer, H., Al-Qadi, I., Barber, E., Okte, E., Zhu, Z., Wu., S. (2017). Evaluation of I-FIT Results and Machine Variability Using MnRoad Test Track Mixtures. Report FHWA-ICT-17-012.

Pacheco, J., Bavastri, C., Pereira, J. (2015). Viscoelastic Relaxation Modulus Characterization Using Prony Series. *Latin American Journal of Solids and Structures.* 12, pp. 420-445.

Park, H., Kim, Y.R. (2013). Investigation into Top-Down Cracking of Asphalt Pavements in North Carolina. *Transportation Research Record: Journal of the Transportation Research Board*, 2368, pp. 45-55.

Pellinen, T., Witczak, M., Bonaquist, R. (2003). Asphalt Mix Master Curve Construction Using Sigmoidal Fitting Function with Non-Linear Least Squares Optimization. *Materials Characterization/Modeling of Pavement Systems,* pp. 83-101.

Perez-Jimenez, F., Valdes, G., Miro, R., Martinez, A., Botella, R. (2010). Development of a New Test Procedure for Evaluating Cracking Resistance in Bituminous Mixtures. *Transportation Research Record: Journal of the Transportation Research Board*, 2181, pp. 36-43.

Perez-Madrigal, D., Iannone, A., Martinez, A., Giustozzi, F. (2017). Effect of Mixing Time and Temperature on Cracking Resistance of Bituminous Mixtures Containing Reclaimed Asphalt Pavement Material. *Journal of Materials in Engineering,* 29(8), pp. 1-8.

Porter, R. (2016). The Effects of Notch Geometry on Fracture Testing of Asphalt Concrete. *Honor Theses.*

Roque, R. Koh, C. Chen, Y., Sun, X., Lopp, G. (2009). Introduction of Fracture Resistance to the Design and Evaluation of Open Graded Friction Courses in Florida. *Florida Department of Transportation.* BD-545 #53.

Rozumek, D., Macha, E., Lazzarin, P., Meneghetti, G. (2006). Influence of Notch (Tip) Radius on Fatigue Crack Growth Rate. *Journal of Theoretical and Applied Mechanics,* 44 (1), pp. 127-137.

Saxena, A. (1998). Nonlinear Fracture Mechanics for Engineers. Boca Raton, FL: CRC Press LLC.

Smith, S., Morales, A., Braham, A. (2019). Evaluating Aggregate Size Effects on Dynamic Modulus Using Gray Scale Analysis, submitted to Asphalt Paving Technology: *Journal of the Association of Asphalt Paving Technologist*.

Souza, J., Yoshimura, H., Peres, F., Schon, C. (2012). Effect of Sample Pre-Cracking Method and Notch Geometry in Plane Strain Fracture Toughness Tests as Applied to a PMMA Resin. *Polymer Testing,* 31, pp. 834-840.

Starkova, O., Aniskevich, A. (2009). Application of Time-Temperature Superposition to Energy Limit of Linear Viscoelastic Behavior. *Journal of Applied Polymer Science.* 114, pp. 341-347.

Wagoner, M., Butlar, W., Paulino, G. (2005a). Development of a Single-Edge Notched Beam Test for Asphalt Concrete Mixtures. *Journal of Testing and Evaluation.* 33(6), pp. 452-460.

Wagoner, M., Butlar, W., Paulino, G. (2005b). Disk-shaped Compaction Tension Test for Asphalt Concrete Fracture. *Society for experimental mechanics.* 45(3), pp 270-277.

Wagoner, M., Butlar, W., Paulino, G. (2005c). Investigation of the Fracture Resistance of Hot Mix Asphalt Concrete Using a Disk-Shaped Compact Tension Test. *Transportation Research Record: Journal of the Transportation Research Board,* No 1929, Washington, D.C, pp 183-192.

Yang, S., Braham, A. (2013). The Investigation of R-Curves of Asphalt Concrete. *Airfield and Highway Pavement 2013: Sustainable and Efficient Pavements, ASCE.* pp, 1064-1074.

Yang, S., Braham, A., Underwood, S., Hanz, A., Reinke, G. (2017). Correlating Field Performance to Laboratory Dynamic Modulus from Indirect Tension and Torsion Bar. *Road Materials and Pavement Design*, 8 (1), pp. 104-127.

Chapter 2 Ruggedness Test of Fracture Energy and Flexibility Index using Semi- Circular Bend Test

Abstract

Cracking in asphalt concrete is one of the principal distresses that affect the quality and smoothness of roads. Therefore, multiple tests exist to evaluate the fracture behavior, including AASHTO TP 105 and AASHTO TP 124. Many properties affect the performance, cracking behavior, and durability of asphalt concrete. Some of these factors include Nominal Maximum Aggregate Size (NMAS), binder grade, loading rate during testing, and temperature during testing. This study investigated the influence of these four factors on the cracking performance of asphalt concrete by using a ruggedness test (ASTM E1169), which evaluates the individual significance and interactions of different factors. Two analyses methods were made following the test method procedure from AASHTO TP 105 specification, one for fracture energy and another for flexibility index, using four factors and two levels: NMAS (9.5 and 25 mm), binder grade (PG 64-22 and PG 76-22), loading rate (0.03 and 1.00 mm/min), and temperature (-24 and 0 °C). Results showed that temperature had a significant effect on both fracture energy and flexibility index. However, the loading rate was only significant for the flexibility index. NMAS and binder grade were significant only for fracture energy. In conclusion, due to the viscoelastic properties of asphalt concrete, fracture energy and flexibility index showed different trends based on their sensitivity to the factors that were applied.

Keywords: asphalt concrete, ruggedness test, semi-circular bend test, fracture energy, flexibility index.

2.1 Introduction

Cracking behavior can be evaluated by performing tests such as AASHTO TP 105 and AASHTO TP 124. Both test methods use a semi-circular geometry. AASHTO TP 105 determines fracture energy, fracture toughness, and stiffness, while AASHTO TP 124 determines fracture energy and flexibility index. Although both test methods determine fracture energy, the specimen thickness, loading rate, and testing temperature from each specification are not the same.

2.1.1 Test Methods

AASHTO TP 105 was created because of the need of studying fracture resistance at low temperatures due to thermal cracking (Li *et al.*, 2006). Usually, asphalt concrete fracture tests are performed on notched specimens and the rectangular notch is one of the most commons. Some of the properties were selected from previous research made in fracture resistance. For instance, Roque et al. (1999) used a 25-mm thickness for Indirect Tension (IDT) specimens to study the crack growth rate. Therefore, two thicknesses were evaluated by a finite element analysis: 25 mm and 50 mm. A 25-mm thickness was selected to meet the plane stress conditions needed in fracture toughness (Li *et al.*, 2004). For testing temperature, Li et al., (2004) used two low temperatures: -30 ºC and -40 ºC for two binder types: 58-28 and 58-40. The results showed that some micro-cracks can be formed at temperatures lower temperature of the PG lower limit. The loading rate of 0.03 mm/min is not mentioned how it was determined.

AASHTO TP 124 was developed to evaluate the asphalt concrete fracture behavior of potential cracking between different mixtures especially when using reclaimed asphalt pavement (RAP) and recycled asphalt shingles (RAS). To determine the properties, multiple temperatures and loading rates were tested. The intermediate temperature of 25 ºC, which is a modification from the low-temperature SC(B) test, was selected because the peak values were always obtained at that temperature. When the temperature increase, also the loading rate increases, so 50 mm/min was selected because it produced a load-displacement curve higher than the lower loading rates which means that gives a more brittle behavior and the concept of a post-peak unloading could be applied. The thickness of 50 mm was determined by the influence in the flexibility index (Al-Qadi *et al.*, 2015).

2.1.1.1 Fracture Indices

A fracture index can be defined as any parameter obtained from laboratory measurements from a fracture test with the purpose to describe cracking performance on an asphalt mixture (Zhu *et al*, 2017). Different fracture indices are used to characterize the fracture behavior, but this chapter will focus on the calculation of fracture energy and flexibility index. Fracture energy, which is the parameter calculated in AASHTO TP 105 and AASHTO TP 124, is the energy necessary to produce a unit surface crack area (Anderson, 2005; AASHTO, 2013). The fracture energy calculations come from a concept applied in a specification to test concrete and mortar specimens for three-point bend tests on notched beams. The graph which describes the energy was the plot of load versus deformation. The test was performed with a constant rate of deformation depending on the peak load (RILEM, 1985). In 2015, a research performed by Al-Qadi et al. found that the fracture energy was not enough as the only parameter to differentiate between asphalt concrete mixtures (Al-Qadi *et al.*, 2015). Consequently, the flexibility index (FI) was proposed to distinguish a cracking response.

Because of the need to develop an index that describes the fracture process and determine cracking potential, the Flexibility index (FI), which is defined as an indicator to characterize the fracture resistance of asphalt mixtures, was proposed (Al-Qadi *et al*., 2015; AASHTO, 2016). The innovation of this calculation is that FI can be related to fracture mechanics and crack growth rate.

Therefore, the FI region, where it is calculated, represents the zone close to the notch tip, which is the place where cracks develop while testing. The flexibility index considers both the fracture energy and the slope of the load-displacement at the inflection point where the crack starts to propagate (Ozer *et al*., 2017). Also, peak load, critical displacement, displacement at the peak load, and displacement at the end of the test are considered. The FI can catch the variation in the changes of the asphalt concrete material and the design in mixtures. A higher flexibility index indicates lower cracking susceptibility in the field. For instance, if a mix has an FI less than 2, it can be evaluated as poor performing, whereas a good performing mix can have an FI value greater than 6 (Al-Qadi *et al.*, 2015). In comparison with fracture energy, the flexibility index shows a higher sensibility in the mixture variables than fracture energy (Ling *et al*, 2016).

2.1.1.2 Ruggedness Test (ASTM E1169)

Since there are multiple factors that can influence the calculations of fracture energy and flexibility index, a ruggedness test (ASTM, 2014), which is an experimental design that allows the evaluation of the effects of variations between factors studied, can be performed to compare the values obtained from (SC(B)) test methods.

The factors studied in a ruggedness test are the ones known to affect the results. These factors require two limit levels each. Some of the factors that can affect the asphalt concrete properties include nominal maximum aggregate size (NMAS), binder grade, loading rate, and temperature, which are defined in the following list:

- Nominal Maximum Aggregate Size (NMAS): The aggregates used are named from the nominal maximum aggregate size, which can be defined as the largest sieve that retains no more than 10 percent of the aggregate. The larger the maximum aggregate size of an asphalt mixture, the more resistant to a permanent deformation a mixture is in comparison with smaller sizes (Liu *et al.*, 2017).

- Binder Grade: Binders can be modified or unmodified, and this difference can influence the results of fracture tests due to the stiffness that a modified binder can have. This stiffness could lead to a more brittle asphalt that becomes susceptible to cracking.
- Loading Rate: Because of the different vehicles' movements that affect the performance of asphalt concrete, roads are exposed to different loading rates.
- Temperature: Due to the nature of the asphalt binder, temperature is the most important factor that can influence the properties of asphalt concrete.

Multiple researchers have explored fracture energy and flexibility index using the previously mentioned factors. Wu et al. (2005) performed an SC(B) test to evaluate fracture resistance characterization and then make comparisons between different factors, such as NMAS, binder, and notch depth. The NMAS used were 19 and 25 mm which did not give a significant effect in an ANOVA analysis when the notch depth was 25.4 mm and 38 mm. For binder grade, Wu et al. used multiple types of modified binders, in which the interaction results did not give a significant effect (2005). Another study by Li et al. (2010) looked at variables such as loading rate, binder grade, aggregate, notch length, and air voids. The authors found that the loading rate had a significant effect in fracture energy with the different combinations of temperature and notch lengths. Also, the modified binder showed higher fracture energy than the unmodified binder and higher values of PG which had effects on the fracture energy. According to Yang et al. (2017), testing temperature influenced fracture energy, energy rate, and cohesive energy.

Ozer et al. (2016) found that post-peak slope (m), which is a parameter in the flexibility index calculation, looks to be more sensitive to testing conditions, such as temperature and loading rate in crack velocity correlation. Ling et al. looked at the sensitivity of the flexibility index by evaluating traffic level, aging, and binder type. The authors used two low temperatures (-28 and -34 °C) and found that the binder modification can increase the values of the post-peak slope (2016).

2.1.2 Objectives

The focus of this research is the application of the SC(B) geometry using the AASHTO TP 105 test method to obtain fracture energy and flexibility index. The objectives of this study are to:

- Evaluate the impact of NMAS, binder type, loading rate, and testing temperature through ASTM E1169 ruggedness test;
- Determine the behavior of the flexibility index, which values are calculated from SC(B) specimen tested according to AASHTO TP 105, at lower temperature.

2.2 Materials and Methods

2.2.1 Materials

Two different mixes were used for the study. The nominal maximum aggregate sizes (NMAS) used were 9.5 mm and 25 mm combined with two binder grades: a neat binder PG 64-22 and a PG 76-22, which was modified from a neat binder with SBS polymer. The binder content for both binder grades used for the NMAS 9.5 mm was 5.70% and the effective binder was 3.88%, and for the 25 mm the binder content was 4.02% and the effective binder was 2.45%, as shown in Table 2.1. Because the same binder content was used for each of the NMAS for the binder types, the effective binder content, which is the asphalt not absorbed into the aggregate, was calculated. When having differences in the effective binder content, also the asphalt film thickness is affected which could lead to some problems in the pavement to become brittle and less durable (Chadbourn *et al.*, 1999).

Table 2.1 Asphalt Binder Content

NMAS	Binder Type	Binder Content (%)	Effective Binder Content (%)
9.5 mm	PG 64-22	5.70	3.88
	PG 76-22		
25 mm	PG 64-22	4.02	2.45
	PG 76-22		

The mix design air voids target was 4%, but the samples were compacted at 7% air voids in the laboratory, as specified by the test methods. Test specimens were subjected to two hours aging at the compaction temperature. Additional details for the mixes may be found in the research of Yang *et al*. (2017). The experimental matrix for this study is shown in Table 2.2.

Table 2.2 Experimental Matrix

Factors	Number of Levels	Level Value
NMAS	2	9.5 mm, 25 mm
Binder	2	PG 64-22, PG 76-22
Loading Rate	2	0.03 mm/min, 1.0 mm/min
Temperature	2	0 ℃, -24 ℃

2.2.2 Test Methods

In this study, an SC(B) test was performed following the AASHTO TP 105 specification to calculate the results of fracture energy and then the flexibility index. Potential factors that may affect the fracture energy and the flexibility index obtained from these tests were analyzed using a ruggedness test.

2.2.2.1 Fracture Energy: AASHTO TP105 specification is the semi-circular bend (SC(B)) fracture test method, which determines the fracture energy and fracture toughness at low temperatures of asphalt concrete with a semi-circular geometry. According to the specification, the samples are sawed from the middle of a 150-mm diameter compacted specimen and then cut in half with a 25-mm thickness and a 15-mm notch length and 1.5 mm width.

For test performance, after conditioning the sample, the sample is situated on the test fixture and a clip gage is attached. The loading rate applied is 0.03 mm/min or 0.0005mm/s. A load is applied to the sample, and the external Load Line Displacement (LLD) and the Crack Mouth Opening Displacement (CMOD) are recorded. The analysis is made when the load applied to the specimen starts increasing from 0.3 kN to a peak load. Then the load starts to decrease, and it is stopped when the load drops below 0.5 kN, or when the crack mouth opening displacement limit is reached, whichever occurs first. Once the test is completed, the fracture energy (Eq. 2.1) is calculated by taking the area under the load/external LLD curve and dividing this value by the area of the ligament of the tested sample (Fig. 2.1). Higher fracture energy indicates lower cracking susceptibility in the field (Al-Qadi *et al*., 2015).

$$G_f = \frac{W_f}{A_{lig}} \qquad \text{(Eq. 2.1)}$$

Where:

G_f = fracture energy (J/m^2),

W_f = work of fracture (J), and

A_{lig} = ligament area (m^2).

2.2.2.2 Flexibility Index: The I-FIT Method utilizes the AASHTO Specification TP124-16, and fracture energy and flexibility index (FI) are the two parameters obtained from this test procedure. However, for this study, the Flexibility Index (Eq. 2.2) was calculated from the fracture energy value obtained in the AASHTO TP 105 specification.

$$FI = \frac{G_f}{|m|} \; x \; A \qquad \text{(Eq. 2.2)}$$

Where:

G_f = fracture energy (J/m^2),

$|m|$ = absolute value of post-peak load slope m (kN/mm), and

A = factor for unit conversion and scaling equal to 0.01.

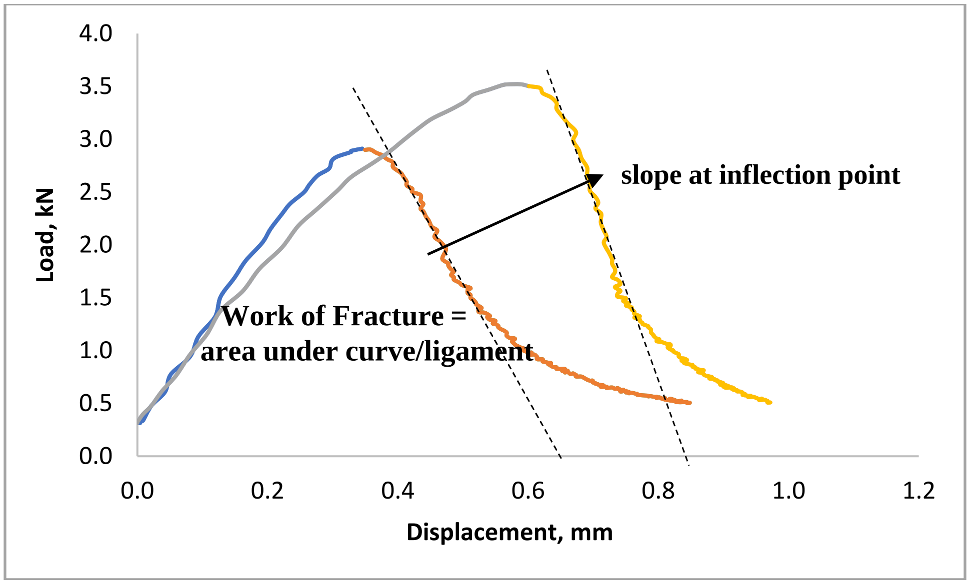

Figure 2.11 Load-displacement curve for flexibility index and fracture energy calculations

2.2.2.3 Factors and Levels: The performance, deformation behavior, and durability of asphalt concrete can be affected by several factors such as type of aggregate, binder, loading rate, and temperature (Fakhri, 2018). Therefore, it is important to evaluate the factors which interact with asphalt concrete. For this research, four factors were evaluated: nominal maximum aggregate size (NMAS), binder grade, loading rate, and temperature. Table 2.3 summarizes the factors that were considered for the ruggedness test. The following list explains why the upper and lower values were chosen based on the results of the study performed by Yang et al. (2017):

- Nominal Maximum Aggregate Size (NMAS): The NMAS may influence the performance of asphalt concrete in fracture behavior since the size of the gradation affects the aggregate

(Yang *et al.*, 2017). Therefore, a 9.5 mm, which is used as a surface mix, and a 25 mm NMAS, which is used as a binder mix, were selected.

- Binder Grade: Two asphalt binder grades were selected: PG 64-22 (unmodified) and PG 76-22 (polymer modified). When adding polymers to the binder, the stiffness can increase at high temperatures, but may also affect the fracture behavior at low temperatures. Including both modified and unmodified binders – with a wide range of stiffness– allows the evaluation of binder stiffness as a factor.
- Loading Rate: Since there are different loading rates proposed to perform fracture tests, the first loading rate was from AASHTO TP 105 (0.03 mm/min) and the second (1.0 mm/min) from previous research made in 2017 by Yang et al. The intent was to create a large range of loading rates to explore how the loading rate influenced the results. Also, when having a high temperature, a fast loading rate may be similar to a slower loading rate for a lower temperature.
- Temperature: Asphalt behavior depends on temperature. Hence, two low temperatures were selected: -24 °C and 0 °C. For -24 °C, the temperature of -22 °C is the lower limit for both binder grade used and a 2 °C temperature below the lower PG limit is recommended to be used in a fracture test to capture the glass transition temperature in asphalt concrete (Braham *et al.,* 2007). The temperature of 0 °C was chosen to explore fracture energy with higher temperatures and a faster loading rate.

Table 2.3 Factors considered for the ruggedness test

Factor No.	**Factor**	**Units**	**Lower Level Value**	**Upper Level Value**
A	NMAS	mm	9.5	25
B	Binder	grade	PG 64-22	PG 76-22
C	Loading Rate	mm/min	0.03	1.00
E	Temperature	°C	-24	0

Ruggedness Test: A ruggedness test is used to determine factors that can influence the results from test methods analyzed. Consequently, these factors must be looked at closely while testing. To perform the ruggedness test, two levels need to be considered per each factor upper-level value and lower-level value. These two values are recommended to be extreme limits from the factors that could be possible in the laboratory. This separation will increase the interactions between the factors and the upper and lower level values. The upper-level value is represented with the (+) symbol and the lower level value with the (-) symbol. Every factor will have the same amount of upper and lower values (ASTM, 2014).

The ruggedness test can be performed from four to seven factors in a Plackett-Burman (PB) order design. Table 2.4 shows the design recommended up to 7 factors from ASTM E1169. If the number of variables is less than seven factors, the following options must be applied:

- For four factors, the columns A, B, C, and E are used.
- For five factors, the columns A, B, C, D, and F are used.
- For six factors, the columns A, B, C, D, F, and G are used.

Table 2.4 Recommended design up to 7 factors from ASTM E1169

PB Order	A	B	C	D	E	F	G	Test Result
1	+1	+1	+1	-1	+1	-1	-1	
2	-1	+1	+1	+1	-1	+1	-1	
3	-1	-1	+1	+1	+1	-1	+1	
4	+1	-1	-1	+1	+1	+1	-1	
5	-1	+1	-1	-1	+1	+1	+1	
6	+1	-1	+1	-1	-1	+1	+1	
7	+1	+1	-1	+1	-1	-1	+1	
8	-1	-1	-1	-1	-1	-1	-1	
Ave +								
Ave -								
Effect								

The following steps are used to perform the ruggedness test calculations:

- First, the averages from the upper level (+) and lower level (-) values from the average of the test results' replicates are calculated and separated for each factor or column. For example, from PB order 8, the result is from the factor combination for all the lower-level values.
- Then, the Average+ is the average of the upper-level results from each factor. On the other hand, the Average- is the average of the lower-level results from each factor.
- The main effect is the difference between the upper level (+) average and the lower level (-) average. The differences between the factors are ordered from the highest to the lowest value, regardless of the sign of the number.
- The standard deviation is calculated from the difference between the replicates of the test results. The main effect is then divided by the standard error effect to obtain a value of student's t-test.
- With the student's t-test, a p-value can be calculated. If the p-value is <0.05 the factor is significant, otherwise, it is not significant.

For this research study, four factors were analyzed. Therefore, the columns A, B, C, and E described in Table 4 were used.

2.3 Results and Discussion

Since four factors: NMAS, binder, loading rate, and temperature, were evaluated in this paper, the columns A, B, C, and E were used from the ASTM E1169 experimental design for both fracture energy and flexibility index. Four replicates per combination were tested to get the average of fracture energy (J/m^2). Table 2.5 presents the calculations of the average (+), average (-), and the main effect for fracture energy. Average (+) and average (-) were calculated for each factor column from the average values and then the main effect was [Ave (+) – (Ave (-))]. For example, column

A’s values (+1 = 25 mm) are: 1159.54, 1053.87, 392.96, 507.93, which gives the Average (+) of 778.57. Then, Column A’s values (-1 = 9.5 mm) are: 523.47, 539.32, 806.80, 357.53, which gives the Average (–) of 556.78. The difference of both averages gives the number of 221.79, which is the main effect and can be interpreted as the changing factor from low level to high level

Table 2.5 Calculations of the main effect for fracture energy

	NMAS	**Binder**	**Loading Rate**	**Temperature**	**Fracture Energy (J/m2)**	
PB order	**A**	**B**	**C**	**E**	**Average**	**Difference**
1	+1	+1	+1	+1	1159.54	618.60
2	-1	+1	+1	-1	523.47	170.63
3	-1	-1	+1	+1	539.32	249.54
4	+1	-1	-1	+1	1053.87	896.04
5	-1	+1	-1	+1	806.80	494.48
6	+1	-1	+1	-1	392.96	235.61
7	+1	+1	-1	-1	507.93	359.42
8	-1	-1	-1	-1	357.53	100.63
Ave +	778.57	749.44	653.82	889.88		
Ave -	556.78	585.92	681.53	445.47	Standard	**66.52**
Main Effect	**221.79**	**163.52**	**-27.71**	**444.41**	Error Effect	

The difference between the replicates was calculated as the subtraction of the highest fracture energy from the lowest of each combination. With the differences of the replicates, the standard error effect was calculated with Equation 2.3 and the degree of freedom with Equation 2.4.

$$S_{effect} = \sqrt{\frac{4\, s_{rep}^2}{N\ x\ reps}} \tag{Eq. 2.3}$$

$$Degree\ of\ freedom = (N-1)\ x\ (Reps-1) \tag{Eq. 2.4}$$

Where:

S_{effect} = Standard error effect,

N = number of runs in the design,

Reps= number of the replicates of the design, and

s_{reps} = estimated standard deviation of the test results

Table 2.6 shows the summary of the main effect results for fracture energy in the order of the effects obtained from Table 2.5. To determine if the factors are significant, a student's t-test is calculated by dividing the main effect by the standard error effect. Then, the p-value is calculated with the degree of freedom (Eq. 2.4). Temperature, NMAS, and binder grade each had a significant effect on the fracture energy with a p-value < 0.05. However, the loading rate did not have a significant effect on fracture energy.

Table 2.6 Statistics results for main effects for fracture energy

Effect Order	Effect	Main Effect	t	p-value
E	Temperature	444.41	6.68	<0.001
A	NMAS	221.79	3.33	0.003
B	Binder	163.52	2.46	0.02
C	Loading rate	-27.71	0.42	0.68

For flexibility index, the values were calculated from the SC(B) test AASHTO TP 105 for low temperature. The slope at the inflection point was obtained from the load-displacement curve for each of the replicates. Table 2.7 shows average (+), average (-), and the main effect for each of the factors. Also, the same columns (A, B, C, and E) from ASTM E1169 used for fracture energy were used for the flexibility index.

Table 2.7 Calculation of the main effect for flexibility index

	NMAS	Binder	Loading Rate	Temperature	Flexibility Index	
PB order	**A**	**B**	**C**	**E**	**Average**	**Difference**
1	+1	+1	+1	+1	1.35	-2.14
2	-1	+1	+1	-1	0.02	-0.06
3	-1	-1	+1	+1	0.27	0.51
4	+1	-1	-1	+1	3.33	4.15
5	-1	+1	-1	+1	2.65	3.16
6	+1	-1	+1	-1	0.00	0.00
7	+1	+1	-1	-1	0.22	0.89
8	-1	-1	-1	-1	0.02	0.05
Ave +	1.22	1.06	0.41	1.90		
Ave -	0.74	0.90	1.55	0.26	Standard	**0.50**
Main Effect	**0.49**	**0.16**	**-1.14**	**1.64**	Error Effect	

Table 2.8 shows the summary of the main effect results for the flexibility index in the order of the effects obtained from Table 2.7. The temperature and loading rate had a significant effect on the flexibility index with a p-value < 0.05. However, NMAS and binder grades did not have a significant effect on the flexibility index.

Table 2.8 Statistics results for main effects for flexibility index

Effect Order	Effect	Main Effect	t	p-value
E	Temperature	1.64	3.32	0.003
C	Loading Rate	-1.14	2.31	0.03
A	NMAS	0.49	0.98	0.34
B	Binder	0.16	0.31	0.76

2.3.1 Fracture Energy and Flexibility Index

After performing a ruggedness test for both fracture energy and flexibility index, as expected, temperature is a significant factor to be considered in asphalt concrete. However, the loading rate is not a significant factor for fracture energy. Temperature and loading rate have been tightened together in asphalt concrete studies and cracking behavior, so these results of not being significant for fracture energy are an interesting finding. A study performed by Al-Qadi et al., (2015) found that at low temperatures, fracture energy looks to be less rate-dependent than at intermediate temperatures. For instance, at temperatures less than 0 °C, fracture energy does not present an increase due to slow or similar loading rates. However, at intermediate temperatures, fracture energy increases when the loading rate increases (Al-Qadi *et al.*, 2015). On the other hand, flexibility index calculation can be affected by different parameters such as fracture energy, slope at the inflection point (m), peak load, critical displacement, and displacement at the peak load. Nonetheless, the post-peak slope (m) parameter appears to be more sensitive to testing conditions changes as loading rates and temperature (Al-Qadi *et al.*, 2015). In 2017, a study performed by Zhu et al. found that when the temperature increases, the fracture energy and flexibility index increase as well. This behavior occurs because at higher temperatures there is more energy necessary to fracture the asphalt mixtures (Zhu et al., 2017). In this chapter, the same behavior was experienced in the calculations for both fracture energy and flexibility index.

NMAS and binder were only significant in fracture energy. Yang et al. (2017) used 9.5 mm and 25 mm NMAS to calculate fracture energy. The authors found that the 25 mm NMAS had more fracture energy in comparison with 9.5mm. On the other hand, Wu et al. (2005), evaluated fracture resistance characterization with an ANOVA analysis from two NMAS: 19 mm and 25 mm. The results showed that NMAS did not give a significant effect when using a notch depth of 25.4 and 38 mm and significant for a 31-mm notch depth. However, their range of NMAS was narrower than ours, therefore, it appears that the influence of aggregate size becomes significant somewhere between a difference of 6 mm and 15.5 mm. In 2017, Ozer et al. conducted research where eight mixtures were evaluated according to the flexibility index calculated. The NMAS used were 4.75, 12.5 and 19 mm, and the binder types used were PG 58-34, PG 64-22, PG 64-34 and PG 70-22. Higher NMAS as 12.5 and 19 mm and the binder type PG 64-22 experienced lower flexibility index values, which means poor field performance (Ozer *et al*., 2017). In comparison with this study and the results obtained in this Chapter, PG 64-22 and 25 mm experienced both low and high flexibility index values. For instance, PG 64-22 obtained most of the low flexibility index values, between 0 and 0.3; however, in one combination with 25 mm NMAS resulted in a higher flexibility index value of 3.3. On the other hand, half of the 25 mm NMAS samples had lower flexibility index values of 0 and 0.3, and the other half had a higher flexibility index value of 1.3 and 3.3. These results could be due to the added combinations of loading rates and testing temperature to the research since the higher flexibility index values were obtained when combined with the higher temperature testing.

Fracture energy and flexibility index are fracture parameters that are used to characterize cracking behavior. After the statistical analysis performed of these values, it showed that depending on the factors applied those are significant or not. Fracture energy is sensitive to temperature, NMAS and binder type, but the flexibility index is sensitive to temperature and loading rate. Since asphalt is viscoelastic, fracture energy at low temperature does not depend on the loading rate. However, the flexibility index due to the sensitivity of the post-peak slope may experience differences when changing the temperature and loading rate. Consequently, the range of the loading rate tested (0.03 and 1.00 mm/min) for fracture energy may need to be wider in future research to see the interactions that those results may have.

2.4 Conclusions

The purpose of this chapter was to perform a ruggedness test to evaluate the effects of four factors: NMAS (9.5 and 25 mm), binder grade (PG 64-22 and PG 76-22), loading rate (0.03 and 1.00 mm/min), and temperature (-24 and 0 °C). These factors may affect the performance of asphalt concrete and were evaluated by making a comparison between fracture energy and flexibility index, which are values used to characterize cracking behavior.

The conclusions from this chapter are the following:

- Fracture energy and flexibility index have different parameters that affect their results because of asphalt's viscoelastic properties. For instance, for flexibility index, post-peak slope (m) can be sensitive to temperature, loading rate, and the low PG temperature. Whereas fracture energy is not affected by the loading rate at low temperature, but it may start to affect the values when increasing the temperature to 0 °C.
- Testing temperature had the most significant effect on both the fracture energy and flexibility index. However, the loading rate did not have a significant effect on fracture energy. Since asphalt concrete is a viscoelastic material, testing temperature and loading rate relate to each other. A wider range for loading rate and testing temperature must be considered to evaluate the results.
- The values of both fracture energy and flexibility index increase when the temperature increases due to the amount of energy necessary to fracture the asphalt mixtures at warmer temperatures.
- The differences in the effective binder content could influence that the NMAS and binder type had a significant effect on fracture energy for the ruggedness test.

2.5 References

AASHTO (2013). Standard Method of Test for Determining the Fracture Energy of Asphalt Mixtures Using the Semicircular Bend Geometry (SCB). TP 105-13. Washington D.C. Fracture Toughness of Asphalt Concrete Materials. *13th International Conference on Fracture.*

AASHTO (2016). Determining the Fracture Potential of Asphalt Mixtures Using the Flexibility Index Test (FIT). TP 124-16. Washington D.C.

Anderson, T. (2005). *Fracture Mechanics Fundamentals and Applications*. Boca Raton, FL: Taylor & Francis.

Al-Qadi, I., Ozer, H., Lambros, J., Khatib, A., Singhvi, P., Khan, T., Rivera-Perez, J., Doll, B. (2015). Testing Protocols to Ensure Performance of High Asphalt Binder Replacement Mixes Using RAP and RAS. Report FHWA-ICT-15-017.

ASTM. (2014). Standard Practice for Conducting Ruggedness Test. E1169-14. West Conshohocken, PA.

Behbahani, H., Aliha, M., Fazaeli, H., Rezaeifar, M. (2013). Effect of Characteristics Specifications on Fracture Toughness of Asphalt Concrete Materials. *13th International Conference on Fracture.*

Braham, A., Buttlar, W., Marasteanu, M. (2007). Effect of Binder Type, Aggregate, and Mixture Composition on Fracture Energy of Hot-Mix Asphalt in Cold Climates, *Transp. Res. Rec*, pp. 102-109.

Fakhri, M., Kharrazi, E., Aliha, M. (2018). The Effect of Loading on Fracture Energy of Asphalt Mixture at Intermediate Temperatures and Under Different Loading Modes. *Frattura ed Integrita Strutturale*, 43, pp 113-132.

Li, X., Marasteanu, M. (2004). Evaluation of the Low Temperature Fracture Resistance of Asphalt Mixtures Using the Semi-Circular Bend Test. *Asphalt Paving Technology: Association of Asphalt Paving Technologists- Proceedings of the Technical Sessions.* 73, pp. 401-426.

Li, Xinjun, and M. O. Marasteanu. (2006). Investigation of Low Temperature Cracking in Asphalt Mixtures by Acoustic Emission. *Road Materials and Pavement Design*, Vol. 7/4. Taylor and Francis Group Online, London, UK, 2006, pp. 491–512.

Li, X., Marasteanu, M. (2010). Using Semi Circular Bending Test to Evaluate Low Temperature Fracture Resistance for Asphalt Concrete. *Experimental Mechanics* (50), pp 867-876.

Ling, C., Swiertz, D., Mandal, T., Teymourpour, P., Bahia, H. (2016). Sensitivity of the Illinois Flexibility Index Test to Mixture Design Factors.

Liu, H., Hao, P., Xu, J. (2017). Effects of Nominal Maximum Aggregate Size on the Performance of Stone Matrix Asphalt. *Applied Sciences*,7.

Ozer, H., Al-Qadi, I., Lambros, J., El-Khatib, A., Singhvi, P., Doll, B. (2016). Development of the Fracture-based Flexibility Index for Asphalt Concrete Cracking Potential Using Modified Semi-Circle Bending Test Parameters. *Construction and Building Materials* (115), pp 390-401.

Ozer, H., Al-Qadi, I., Barber, E., Okte, E., Zhu, Z., Wu., S. (2017). Evaluation of I-FIT Results and Machine Variability Using MnRoad Test Track Mixtures. Report FHWA-ICT-17-012.

RILEM Technical Committee 50-FMC. (1985). Determination of the Fracture Energy of Mortar and Concrete by Means of Three-Point Bend Tests on Notched Beams. *Materials and Structures*, No. 106. Springer Netherlands for International Union of Laboratories and Experts in Construction Materials, Systems and Structures (RILEM), Dordrecht, The Netherlands, pp. 285–290.

Roque, R., Zhang, Z., Sankar, B. (1999). Determination of Crack Growth Rate Parameters of Asphalt Mixtures Using the Superpave IDT. *Presentation at the Annual Meeting of the Association of Asphalt Paving Technologists.*

Wagoner, M., Butlar, W., Paulino, G. (2005). Investigation of the Fracture Resistance of Hot Mix Asphalt Concrete Using a Disk-Shaped Compact Tension Test. *Transportation Research Record: Journal of the Transportation Research Board,* No 1929, Washington, D.C, pp 183-192.

Wu, Z., Mohammad, L., Wang, L., Mull, M. (2005). Fracture Resistance Characterization of Superpave Mixtures Using the Semi-Circular Bending Test. *Journal of ASTM International,* 2(3).

Yang, S., Braham, A. (2017). Influence of Binder Grade, Gradation, Temperature and Loading Rate on R-Curve of Asphalt Concrete. *Construction and Building Materials* (154), pp 780-790.

Zhou, F., Newcomb, D., Gurganus, C., Banohashemrad, S., Park, E. Sakhaeifar, M., Lytton, R. (2016). Experimental Design for Field Validation of Laboratory Tests to Assess Cracking Resistance of Asphalt Mixtures. *National Cooperative Highway Research Program Transportation Research Board,* Report 9-57.

Zhu, Y., Dave, E., Rahbar-Rastegar, R., Daniel, J., Zofka, A. (2017). Comprehensive Evaluation of Low-Temperature Fracture Indices for Asphalt Mixtures. *Road Materials and Pavement Design.*

Chapter 3 Evaluation of Semi-Circular Bend (SC(B)) Geometric Properties for Asphalt Concrete Testing*[1]

Abstract

Cracking in asphalt concrete is one of the principal distresses that affect the quality and smoothness of roads and can be influenced by different factors such as temperature, traffic loads, and construction materials. Therefore, there are some fracture tests, which use a semi-circular geometry, such as AASHTO TP 105 and AASHTO TP 124. The research objective of this study is to investigate the fundamental fracture characterization of asphalt concrete by evaluating the semi-circular bend (SC(B)) test, found in AASHTO TP 105 specification, by analyzing results from different thicknesses to study the representative volume element (RVE), notch configurations for crack initiation and propagation, and testing temperatures. SC(B) methods apply different factors to calculate fracture energy. Hence, this study looks to investigate three thicknesses: 25, 50, and 100 mm; three notch configurations: rectangular, semi-circular, and fatigue pre-cracked; and two low temperatures: -24, and -12 °C. To isolate the influence of thickness and notch configuration, other factors such as a 12.5 mm NMAS, a loading rate of 0.03 mm/min, and a binder type of PG 64-22 have been kept constant. The results show that thickness influences fracture energy calculations. Consequently, to meet the (RVE) and plane strain, which are material behavior required for asphalt concrete, a 50-mm thickness was selected from this study. Notch configuration and low testing temperatures do not have a statistically significant influence on fracture energy. Thus, having a deep understanding of fracture energy analysis can provide a better idea of the cracks developed in asphalt concrete material when selecting a notch configuration.

Keywords: thickness, notch configuration, temperature, fracture energy, asphalt concrete.

1* Technical article to be submitted to ASCE Journal of Materials in Civil Engineering in May 2020

3.1 Introduction

Cracking in asphalt concrete is one of the most common problems that roads have. These problems can be the result of traffic loads and temperature or environment. Therefore, there is a need to research fracture resistance to have a better understanding of cracking behavior. AASHTO TP 105 and AASHTO TP 124 are examples of asphalt concrete fracture tests that calculate a parameter called fracture energy. The AASHTO TP 105 test method is used to determine the fracture energy, fracture toughness, and stiffness, which represents the fracture resistance of asphalt mixtures. Fracture energy (Eq. 3.1) is defined as the energy that is necessary to produce a unit surface crack area and can be calculated as dividing the work of fracture by the ligament area (AASHTO, 2013). Whereas, AASHTO TP 124 calculates fracture energy and flexibility index (FI) (Eq. 3.2) which is a parameter that characterizes the fracture resistance of asphalt mixtures. For this research study, only the fracture energy was calculated.

$$G_f = \frac{W_f}{A_{lig}} \qquad \text{(Eq. 3.1)}$$

$$FI = \frac{G_f}{|m|}\ x\ A \qquad \text{(Eq. 3.2)}$$

Where:

G_f = fracture energy (J/m^2),

$W_f = \int Pdu,$ work of fracture (J),

P = applied load (N),

U = average load line displacement (m),

A_{lig} = (r-a) x t, ligament area (m^2),

a = notch length (m),

r = specimen radius (m),

t = specimen thickness (m),

$|m|$ = absolute value of post-peak load slope m (kN/mm), and

A = factor for unit conversion and scaling equal to 0.01.

Both tests AASHTO TP 105 and AASHTO TP 124 calculate fracture energy, utilize a semi-circular geometry, and have a rectangular notch configuration. However, the specimen thickness, loading rate, and testing temperature are different, which are factors that influence cracking behavior based upon fundamental fracture mechanics. Since there are differences between the semi-circular geometric properties in several test methods, this chapter will focus on the evaluation of thicknesses and notch configurations of a Semi-Circular Bend (SC(B)) asphalt concrete specimen.

3.1.1 Thickness

Fracture mechanics concepts have been applied to multiple fields and parameters, such as thickness and notch configuration, which have been studied in different materials. In initial fracture mechanics research, thickness was ignored but later found important because it caused effects in the variation of the critical stress intensity factor when using aluminum alloy. In metals, the specimen thickness can affect the plastic deformation of the material. For instance, when a specimen is thick, the elastic constraint, which is established by the thickness, is large and the crack extension can happen more easily; however, the opposite happens for a thin specimen (Wright *et al.*, 1977). In adhesive epoxy joints, fracture energy is also calculated. When increasing the adhesive layer thickness, the fracture energy increases (Marzi *et al.*, 2011). In concrete research, when increasing the specimen thickness, the concrete strength decreases; nonetheless, the fracture energy and fracture toughness increase when the specimen thickness is larger (Duan *et al.*, 2003; Wittmann *et al.*, 1990). Hence, investigating the influence of thickness in different materials before applying fracture mechanics is important because the material may exhibit a thickness effect (Wright *et al*., 1977).

In fracture mechanics, the fracture energy can be related to the energy release rate (G_{Ic}) to obtain fracture toughness as seen in Eq. 3.3. G can also be called the cracking driving force which units are force per unit crack extension (Broek, 1986; Anderson, 2005).

$$G_{Ic} = \frac{{K_{Ic}}^2}{E}(1 - \upsilon^2) \qquad \text{(Eq. 3.3)}$$

Where:

G_{Ic} = energy release rate,

E = Young’s Modulus,

K_{Ic} = fracture toughness, and

υ = Poisson’s ratio

To evaluate the significance of specimen thickness to cracking behavior, fracture toughness, which represents the amount of stress generated from an existing flaw in a material, must be considered. These existing flaws can appear as voids, cracks, material defects, and design discontinuities. Given the heterogeneous composition of asphalt concrete, which is a mixture of asphalt binder, aggregate, and air voids, the presence of these flaws is assumed. Fracture toughness is determined by the stress-intensity factor (K), which is a function of loading, crack size and geometry, and represents the stress formed at the crack tip. K_{Ic} is then the highest stress intensity value that can reach a material without fracture. For specimens of different sizes, the value of K can vary because when changing the specimen thickness, and the stress adjacent to the flaws changes until the thickness obtains a critical dimension. At this point, K becomes a constant value (K_{Ic}), which is a true material property called the plane-strain fracture toughness, as shown in Figure 3.1. Plane stress can be defined in a very thin specimen that when pulled, the cross-section would neck because there is no stress in the other direction to provide a constraint. On the other hand, plane strain can be defined in a thick specimen that has enough material where the cross-section would not be affected because there is no constraint (Broek, 1986; Anderson, 2005).

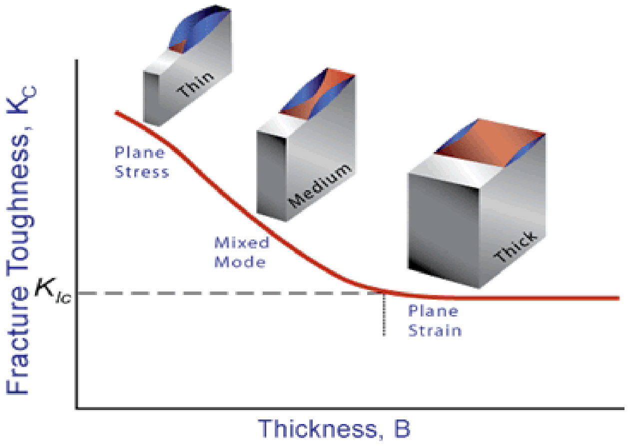

Figure 3.1 Fracture Toughness vs. Thickness (NDT Resource Center, 2014)

Figure 3.1 shows the thickness effect on fracture toughness. For instance, K_{Ic} starts decreasing and the specimen thickness increasing until a point that K_{Ic} is not sensitive to the specimen increase. The main reason to have a thick thickness is that the plane stress does not develop and just a small region is at the specimen surface, so the thickness must be larger than the size of the plastic zone (Broek, 1986; Anderson, 2005).

$$B \geq 2.5 \left(\frac{K_{Ic}}{\sigma_y}\right)^2 \qquad \text{(Eq. 3.4)}$$

Where:

B = specimen thickness necessary to reach plane strain (m),

K_{Ic} = fracture toughness of the material, and

σ_y = yield stress of the material.

From Equation 3.4, the portion of $\left(\frac{K_{Ic}}{\sigma_y}\right)^2$ is proportional to the plastic zone size. Materials in the field, especially metals, exhibit a yield stress, where the material deforms plastically. Thus, there is a region in the vicinity of the crack tip where the plastic deformation occurs, which is called the plastic zone. Figure 3.2 shows the plastic zone (ry) in plane strain and how it increases to accommodate the forces applied. The size of ry for plane strain can be calculated with Equation 3.5 (Broek, 1986; Anderson, 2005).

$$ry = \frac{{K_I}^2}{4\pi{\sigma_y}^2}\left(\frac{3}{2}\sin\theta + (1-2\upsilon)^2 * (1+cos\theta)\right) \qquad \text{(Eq. 3.5)}$$

Where:

ry = size of the plastic zone,

σ_{ys} = yield stress, and

K_I = stress intensity factor.

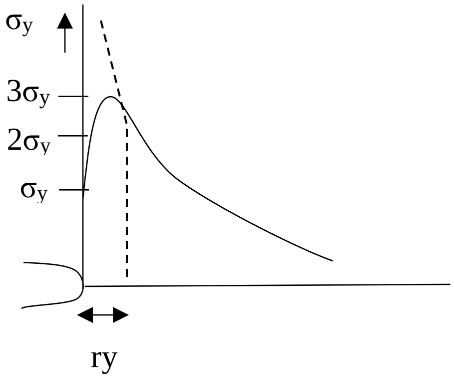

Figure 3.2 Plastic Zone Size for Plane Strain

Since specimen thickness is demonstrated to influence fracture energy in different materials, the asphalt concrete field also presents this concern and some research has been performed on this parameter. Specimen thickness is one of the factors used to calculate the area for fracture energy of asphalt concrete. The dimension of a specimen can be related to the RVE, which is defined as the smallest volume large enough where the material behaves with constant characteristics (Kim, 2009). This concept of RVE has been used for determining specimen sizes to satisfy theoretical requirements for laboratory tests. If smaller than RVE specimen sizes are used in laboratory testing, more samples are required for testing and test results when calculating the averages. Without the inclusion of additional samples, the biases are ignored and could result in large errors (Smith *et al*., 2019). To make sure a specimen describes the global property and not a localized phenomenon, it is necessary to find an optimum specimen size that meets the theoretical requirements of the test that is performed. Also, the internal structure from a sample that is integrated by asphalt binder, aggregates, and air voids affects the mechanical properties of the sample. Thus, RVE is characterized by the statistical homogeneity related to the internal structure (Romero *et al.*, 2001). For instance, RVE conditions for dynamic modulus samples are defined by two main requirements given in ASTM D3497: the ratio of the diameter of the specimen (D) to the maximum aggregate size should be 4:1, and the minimum ratio of specimen height (H) to D should be 2:1.

Another method used to evaluate RVE is an image analysis technique, which is one of the most popular techniques used, is digital image correlation (DIC) (Kim *et al.,* 2009). A study performed by Kim et al. sought to determine RVE with DIC for asphalt concrete mixtures using an NMAS of 12.5 mm. Samples with an approximate thickness size of 45 to 50 mm started to show more consistency, as displayed in Figure 3.3, but the trial RVE, which was found reasonable, was around 60 mm because the standard deviation of strains showed homogeneity at that thickness, as shown in Figure 3.4. Although, the authors considered that a coefficient of variation needed to be applied to account for size distribution in the mixture, a gauge length of 50-60 mm thickness size was recommended for a 12.5 mm NMAS since these values showed consistency in the results (Kim *et al.*, 2010).

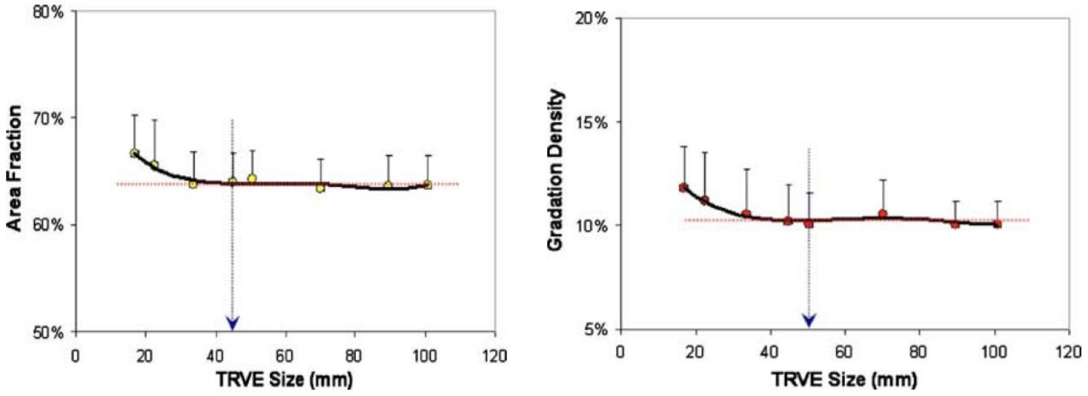

a) Aggregate area fraction vs TRVE size b) Aggregate gradation density vs TRVE Size

Figure 3.3 TRVE sizes before using Coefficient of Variation (Kim et al., 2010)

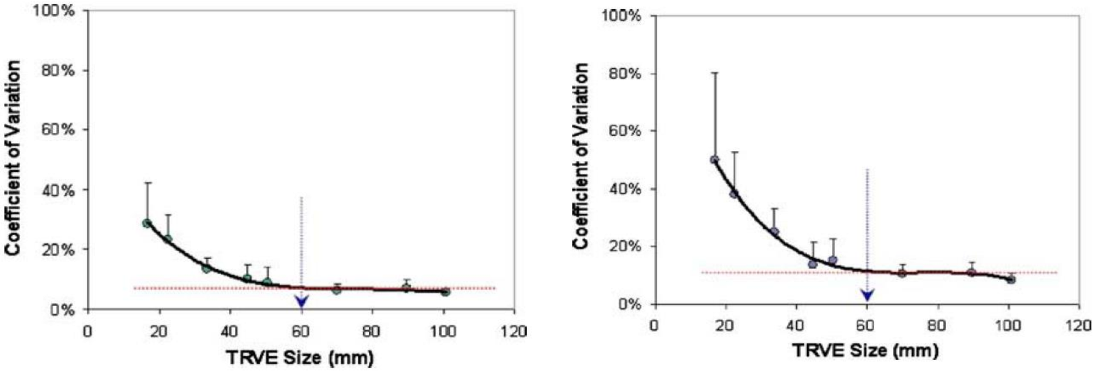

a) Number of aggregate particles b) Mean area of aggregate particles

Figure 3.4 TRVE sizes using Coefficient of Variation (Kim et al., 2010)

As previously mentioned, AASHTO TP 105 and AASHTO TP 124, which are asphalt concrete fracture tests, require different specimen thicknesses. AASHTO TP 105 uses a thickness of 25 mm because it was applied to the Indirect Tension Test (IDT) specimens and met plane stress conditions to calculate fracture toughness. On the other hand, AASHTO TP 124 uses a 50-mm thickness which was selected because of the influence in the flexibility index (Al-Qadi *et al.*, 2015).

3.1.2 Notch Configuration

While both methods AASHTO TP 105 and AASHTO TP 124 utilize rectangular notches, different notch configurations have been shown to influence cracking behavior. Fracture tests for asphalt concrete are usually performed on notched specimens. Other fields that apply fracture mechanics concepts also make this assumption because all engineering materials have cracks where the failure starts. Below, several studies in multiple fields and materials are going to be mentioned to illustrate the importance of having a notch in the specimen. In 2003, a study performed by Ju et al. in a structural steel created for a nuclear power plant, a sharp V-notch was introduced to evaluate the fracture toughness of the material. The results showed that the crack initiated at the tip of the sharp notch; consequently, the extension of the crack and plastic deformation occurred (Ju *et al.,* 2003). In 2013, a study in concrete materials by Grégoire et al. based on concrete beams where the fracture process zone (FPZ) shape and size are different depending on the fracture initiation on notched or unnotched beams was investigated. In this study, different notch depths were selected, with one unnotched, and the results showed that unnotched beams had higher strength than notched beams (Grégoire *et al.,* 2013). Another study on fabric-reinforced hybrid composite proposed five different notch depths from 1 mm to 5 mm with different fiber orientations and percentages of glass content. The results showed that the effect of notch size on fracture toughness was not that severe in comparison with changing the type of materials; however, the notch depth of 1 mm had higher fracture toughness than 5 mm samples

(Kaleemulla *et al.,* 2009). In metallic materials, fracture toughness is proposed to be calculated in a fatigued pre-cracked notch to produce a sharp crack. The fatigue is created by applying a load cyclically on a notched specimen. Some materials are too brittle to produce fatigue because the fracture occurs when the fatigue crack initiates (ASTM, 2006). In asphalt concrete, a study performed on SC(B) samples investigated the effect of using five notch lengths and found that when decreasing the notch length, the peak force and initial stiffness started to increase. Also, the fracture energy is higher for smaller notch lengths. This could be due to having more ligament area to fracture the specimen for small notch lengths (Nsengiyumva, 2015).

To analyze the crack initiation in asphalt concrete, several models and studies have been performed on the cohesive zone of the sample which helps to characterize the fracture behavior in asphalt pavements. This concept implies that the cohesive zone is in front of a crack and takes place in a narrow strip-shaped zone at the time of the fracture process (Liu *et al.,* 2019). The cohesive zone is composed of cohesive strength and fracture energy which represents the damage that occurred in a cohesive zone placed ahead of the crack tip. Figure 3.5 shows the concept of cohesive zone in pure mode I. The cohesive zone model in asphalt concrete has been studied in an indirect tension (IDT) test and a single-edge notch beam (Paulino *et al.*, 2004; Song *et al*., 2005). In this research three notch configuration: rectangular notch, semi-circular notch, and fatigue pre-cracked are selected to study the crack initiation.

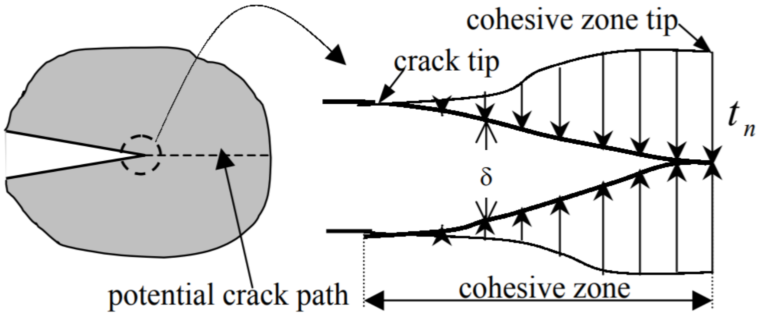

Figure 3.5 Schematic representation of the cohesive zone (Paulino et al., 2004)

A rectangular notch (Fig. 3.6a) is the most common notch configuration used on asphalt concrete. However, this notch configuration can present some issues because the crack is forced to occur at one to two specific locations. A semi-circular notch configuration (Fig. 3.6b) was proposed by Roque et al. (1999) in the development of a Dog-Bone Direct Tension test (DBDT) where the crack can start from any location, especially in the weakest point of the material. Finally, a fatigued pre-cracked notch (Fig. 3.6c) is used typically in metals to produce a sharp crack by applying a load cyclically. This notch eliminates the crack initiation in the specimen. For fracture toughness calculations, a machined notch cannot represent the cracks made in the field, so a short fatigue crack, called pre-cracked, is performed. This pre-crack procedure should follow certain conditions that most of the engineering materials meet, but some brittle materials cannot be pre-cracked (ASTM, 2006).

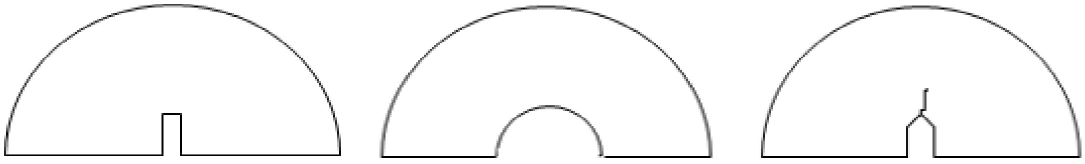

a) Rectangular notch **b) Semi-Circular notch** **c) Fatigue Pre-cracked notch**

Figure 3.6 Notch Configurations

The problem with the 25-mm thickness used in AASHTO TP 105 is that it may not be thick enough to represent the plane strain and describe the true material property. The same happens with the rectangular notch configuration because it forces the crack to occur in a specific location. Therefore, this study looks to evaluate different thicknesses and notch configurations in an SC(B) specimen.

3.1.3 Research Objective

The focus of this chapter is to obtain fracture energy using the AASHTO TP 105 test method to evaluate thickness and notch configurations used in previous studies and materials. The objective of this chapter is to:

- Enhance the test procedure of AASHTO TP 105 by assessing that fundamental fracture mechanics concepts are applied to the specification by evaluating thickness: 25, 50, and 100 mm, three notch configuration of the SC(B) geometry: rectangular, semi-circular and fatigue pre-cracked, and two temperatures of the SC(B) methods: -12 and -24 °C.

3.2 Materials and Methods

3.2.1 Materials

Since the focus of the study is to evaluate the properties of the SC(B) geometry, only one mix design was used. A 12.5 mm nominal maximum aggregate size (NMAS) limestone aggregate, and a PG 64-22 unmodified binder were selected, which is a common mix design in Arkansas used as a surface mix. The binder content used was 4.8%, and the samples were mixed following the short-term conditioning for mixture mechanical property testing from AASHTO R 30 and compacted at 7% air voids.

3.2.2 Test Methods

The SC(B) test was performed following the AASHTO TP 105 specification at low temperatures, -24 and -12˚C, with a 0.03 mm/min loading rate. AASHTO TP 105 uses a 25-mm thickness and a rectangular notch configuration. However, some additional testing variations of the thickness and notch configuration were made to make comparisons with different test methods. A 50-mm, which is used in AASHTO TP 124, and a 100-mm thickness to have a wider range of thickness values, were included to study the plane stress and plane strain, and the RVE of the specimens. Also, a semi-circular and a pre-cracked notch configuration were selected. Table 3.1 shows the experimental matrix for this study.

Table 3.1 Experimental Matrix

Factors	Number of Levels	Level Value
Binder Type	1	PG 64-22
NMAS	1	12.5 mm
Loading Rate	1	0.03 mm/min
Temperature	2	-24 and -12˚C
Thickness	3	25, 50 and 100 mm
Notch Configuration	3	Rectangular, semi-circular, and pre-fatigue

From a compacted asphalt concrete sample for each of the thicknesses, two discs were cut for 25 mm and 50 mm thickness and one disc for 100 mm thickness as shown in Figure 3.7. Therefore, four SC(B) samples were obtained per each compacted sample for 25 mm and 50 mm and two SC(B) samples for 100 mm. The dimensions and the fabrication of the notches were as follows: the rectangular notch was 15 mm in length and 2 mm in width which was sawed after cutting the disc in half. The semi-circular notch had a 12.7 mm (0.5 in) radius where a circular notch with a 1 in diameter was cored from the middle of the disc and then the samples were cut in half, having a semi-circular notch of 0.5 in. in radius. The fatigue pre-cracked notch had an initial rectangular notch and then different combinations of loads were applied.

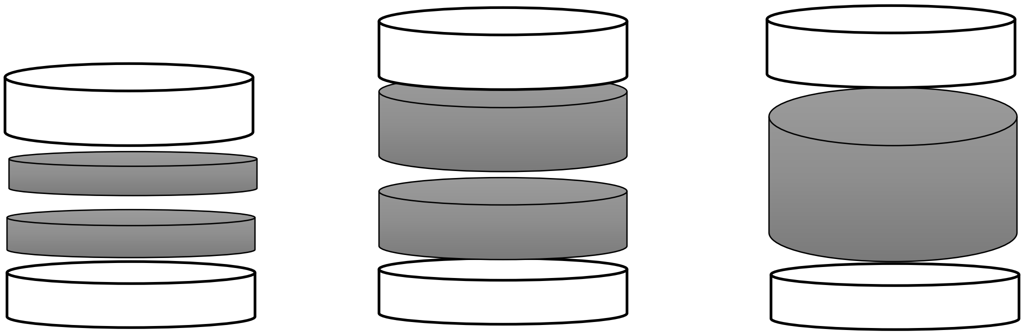

a) 25 mm **b) 50 mm** **c) 100 mm**

Figure 3.7 SC(B) Sample Fabrication

The notch configuration influenced the testing procedure performed. For instance, the rectangular and semi-circular notch configurations were performed using the AASHTO TP 105 procedure where a load is applied and increases from 0.3 kN to a peak load and then the load decreases until it reaches 0.5 kN and the test is manually stopped. However, for fatigue pre-cracked notch configuration the following steps were applied:

1. The average peak load from the rectangular notch samples calculated for each thickness was obtained;
2. On an untested sample, a 20% load from the peak load was applied and then the load was removed;
3. A 40% load from the peak load was applied and then the load was removed;
4. A 60% load from the peak load was applied and then the load was removed;
5. Finally, the load was applied until the sample reached a peak load and decreased to 0.5 kN and the test was manually stopped.

An example of this cyclic loading and unloading sequence is shown in Figure 3.8c for a 100 mm specimen thickness at a -12 ˚C, along with the standard loading curves for the rectangular notch (Fig 3.8a) with a 50 mm thickness at -24 ˚C, and semi-circular notch (Fig 3.8b) with a 25 mm at -12 ˚C.

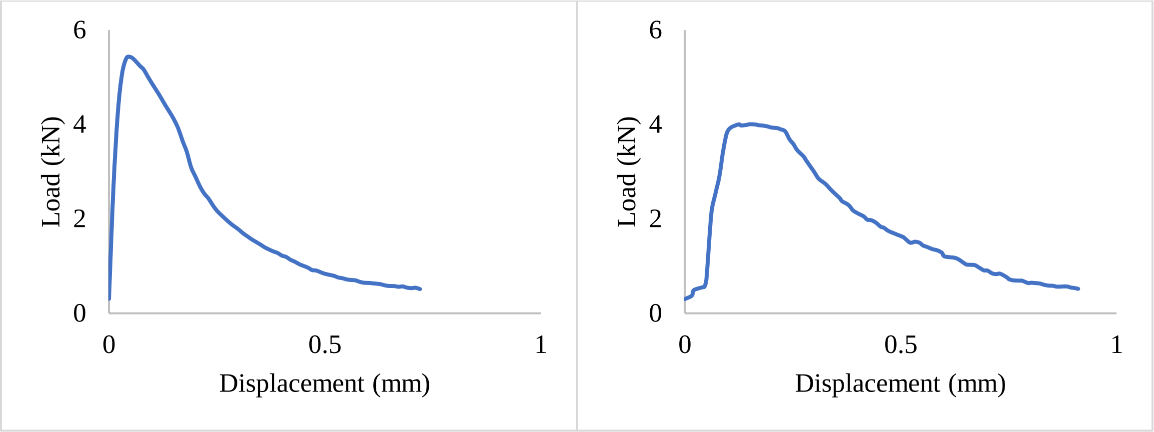

a) Rectangular Notch – 50 mm at -24 ˚C **b) Semi-Circular Notch – 25 mm at -12˚C**

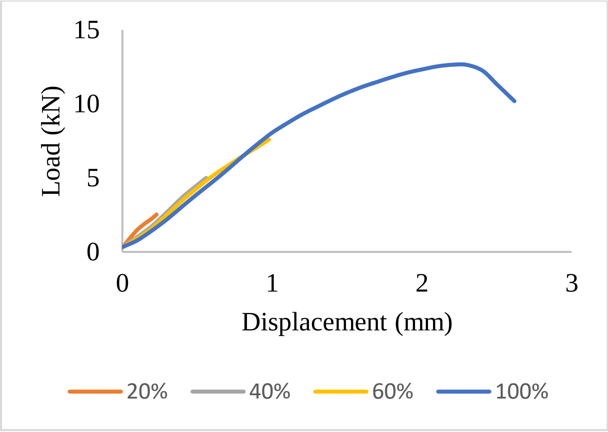

c) Fatigue Pre-Cracked Notch - 100 mm at -12 ˚C

Figure 3.8 Load vs. displacement plot for notch configurations

When fabricating the notch on the samples, several challenges were faced. For instance, the semi-circular notch samples, which was cored first and then cut in half, may have experienced a variety of notch length, to avoid this the most possible, the samples had to be completely centered when cored. Also, according to the specification for the rectangular notch a 10 mm distance has to be kept between the knives glued to the samples. For a semi-circular notch sample, some parts of the knives were not glued completely onto the sample due to the 1-inch diameter (25-mm). However, the 10 mm distance between the knives was kept for consistency between the other notch configurations. Finally, for the fatigue pre-cracked notch, when applying the different load amounts of the peak load, the test had to be stopped manually which could lead to some errors.

Additionally, during the thickness preparation, some challenges were experienced. Since a 100-mm thickness is not common in the asphalt field, handling these samples was challenging due to the heavier weight and difficulty of transport and test. Therefore, to make the 100-mm samples fit on the SC(B) fixture for testing, some changes were made to the fixture to center the sample properly and to include the extensometer to measure the displacement.

3.3 Results and Discussion

After performing the SC(B) test, the fracture energy was calculated for all combinations of thickness, notch configuration, and low temperatures, which are shown in Table 3.2. At the same time, Figure 3.9 shows the graphs made from Table 3.2 which displays the fracture energy results for -12˚C and -24˚C.

Table 3.2 Fracture Energy Results

	Fracture Energy at different Notch Configurations and Test Temperatures (J/m^2)					
	Rectangular		Semi-Circular		Pre-Cracked	
Thickness	**-12 ˚C**	**-24 ˚C**	**-12 ˚C**	**-24 ˚C**	**-12 ˚C**	**-24 ˚C**
25 mm	441	350	425	814	0	0
50 mm	504	499	61	168	493	540
100 mm	4365	1414	1621	1105	2327	1588

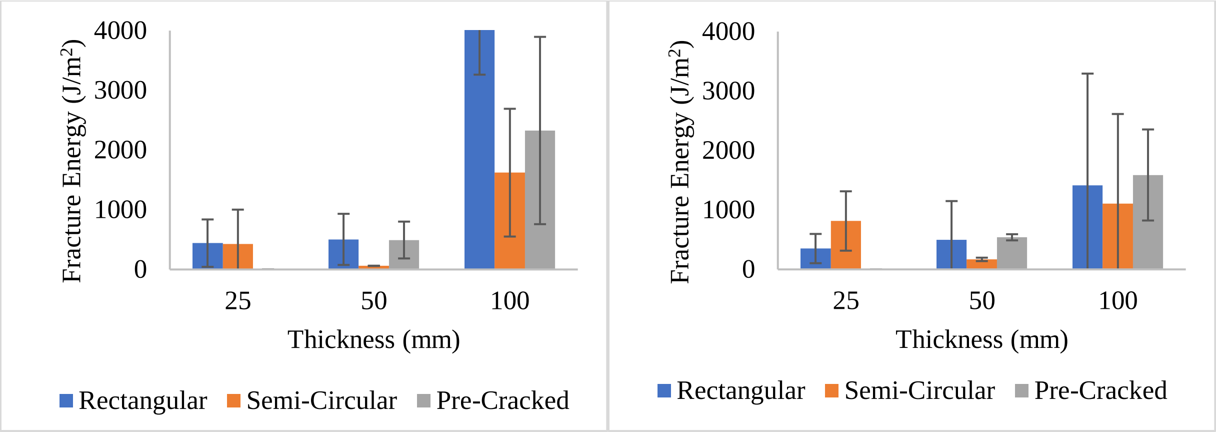

a) Fracture Energy at -12˚ **b) Fracture Energy at -24˚C**

Figure 3.9 Fracture Energy Results

3.3.1 Thickness

Figure 3.9 shows the fracture energy calculated for a combination of three thicknesses, 25, 50 and 100 mm, and three notch configurations: rectangular, semi-circular, and fatigue pre-cracked, at two low temperatures: -12 and -24 ˚C. In general, thickness affects fracture energy, especially in a 100 mm sample. The work of fracture when the load is applied increased with the thickness of the samples. For instance, the peak load average for a 25 mm thickness was 2.50 kN, for a 50 mm thickness was 5.9 kN, and for a 100 mm thickness was 13 kN. The results showed similar trends for both low temperatures and all notch configurations. For the 100-mm thickness, the fracture energy values calculated were high and most of the specimens broke after the peak load was reached. The 25 mm and 50 mm thickness samples had similar fracture energy results in comparison with the 100 mm. However, the fracture energy results from the 50-mm thickness specimens had lower variability between the configurations and temperatures tested in comparison with the other thicknesses.

3.3.1.1 Plane Strain

To determine the fracture toughness of the material, a thick specimen, calculated from Eq. 3.9, is necessary to meet plane strain. AASHTO TP 105 specification gives Eq. 3.6 to calculate the normalized stress intensity factor ($Y_{I(0.8)}$)from the Semi-Circular Bend specimen and the Eq. 3.7 to calculate the stress intensity factor (K_I). Equation 3.8 is given to calculate the shape of the plastic zone in plane strain (Broek, 1986).

$$Y_{I(0.8)} = \left\{4.782 + 1.219 \left(\frac{a}{r}\right) + 0.063 \exp\left(7.045 \left(\frac{a}{r}\right)\right)\right\} \tag{Eq. 3.6}$$

$$K_I = \frac{P}{2rt} \sqrt{\pi a} * Y_{I(0.8)} \tag{Eq. 3.7}$$

$$ry = \frac{{K_I}^2}{4\pi {\sigma_y}^2}\left(\frac{3}{2} \sin\theta + (1-2\upsilon)^2 * (1+cos\theta)\right) \tag{Eq. 3.8}$$

$$B \geq 2.5 * ry \tag{Eq. 3.9}$$

Where:

$Y_{I(0.8)}$ = the normalized stress intensity factor (dimensionless),

a = notch length (m),

r = specimen radius (m),

K_I = stress intensity factor (MPa*m$^{0.5}$),

P = Applied load (MN),

t = specimen thickness (m),

ry = shape of the plastic zone (m),

σ_y = yield stress of the material (MPa),

υ = Poisson's ratio; and

B = specimen thickness necessary to reach plane strain (m).

To calculate B (Eq. 3.8) the following steps were done:

- First, the normalized stress intensity factor ($Y_{I(0.8)}$) from each specimen was calculated depending on the notch length and the radius,
- Then the stress intensity factor (K_I) was calculated by using the maximum applied load (P) per each sample,
- The shape of the plastic zone (ry) was calculated assuming a Poisson's ratio value of 0.35 (Maher *et al.*, 2008; Wu *et al.*, 2013), which is a typical value for asphalt concrete. For the yield stress, since there is not a value measured on asphalt concrete, the average stress calculated from all the samples was used and assumed to be 0.76 MPa.
- Finally, the thickness (B) necessary to reach the plane strain for an SC(B) specimen has to be 2.5 times the plastic zone.

Tables 3.3 and 3.4 show the average B value calculated per specimen thickness for both temperatures. The minimum average thickness obtained, which is necessary to represent the true material property, is 46 mm. When applying the concept of plane stress vs. plane strain for fracture toughness, the value of K_I becomes constant depending on the thickness of the sample, which can represent the true material property.

Table 3.3 Plane Strain Thickness Calculations at -24 ˚C

Thickness	**Y_I**	**σ_o**	**K_I**	**B**
mm	**dimensionless**	**MPa**	**MPa*m$^{0.5}$**	**mm**
25	5.32	0.72	0.84	45.28
50	5.22	0.79	0.86	45.94
100	5.18	0.85	0.87	46.16

Table 3.4 Plane Strain Thickness Calculations at -12 ˚C

Thickness	$\mathbf{Y_I}$	$\boldsymbol{\sigma_o}$	$\mathbf{K_I}$	**B**
mm	**dimensionless**	**MPa**	$\mathbf{MPa{*}m^{0.5}}$	**mm**
25	5.35	0.71	0.86	47.00
50	5.22	0.81	0.87	47.55
100	5.21	0.79	0.84	44.37

3.3.1.2 Representative Volume Element

When determining the correct sample size of a specimen, the representative volume element (RVE) is used to satisfy theoretical requirements because this concept helps to ensure that the specimen represents a global property (Smith *et al.,* 2019). According to Kim et al., the maximum aggregate size in an asphalt concrete mixture is one of the influences on the size of the RVE. Consequently, for a 12.5 mm NMAS or below, an approximate gauge length of 50-60 mm RVE size is recommended for asphalt concrete. This study used the method of DIC to determine the appropriate RVE (Kim *et al.,* 2009; Kim *et al.,* 2010). This means that a sample of thickness of 25 mm thickness, which is the thickness used for AASHTO TP 105 at low temperature, does not meet the RVE requirements for a representative global response. In the same way, the 100-mm thickness which was considered in this study may not be convenient for testing since the results obtained were variable in comparison with the other thicknesses. Also, when comparing handling the sample with the other thickness, a 100-mm thickness may not be practical because many adjustments must be made to the fixture used and it could lead to more errors when cutting the sample thickness and the notch configuration. Therefore, from this study after performing the plane strain calculations and RVE comparison, a 50-mm thickness sample is proposed to be used because it is the smallest size but properly large sample that represents the plane strain and the RVE necessary for testing.

3.3.2 Notch Configuration

As shown in Figure 3.9, for the rectangular notch configuration at both temperatures, the fracture energy increased with the specimen thickness. Whereas, for the semi-circular notch, the fracture energy started increasing for the 25 mm and then decreased for the 50 mm and increased again for a 100 mm thickness. For the fatigued pre-cracked notch configuration samples were able to reach the peak load after applying the pre-loading to produce the fatigue, and then continue with the test, but some samples broke right after reaching the peak load. For this notch configuration, the 50 mm and 100 mm thickness samples were able to reach the peak load when pre-loading was applied every 0.2 peak load until 0.6 peak load and then continue with the test. However, the 25 mm samples broke before getting to the 0.6 peak load, so the actual test was unable to be performed. Because of how brittle an asphalt concrete sample is in comparison with a metal, the concept of the pre-cracked samples is difficult to execute.

3.3.2.1 Crack Initiation

In 1999, Roque et al. performed a study to investigate fracture behavior in an IDT test (Roque *et al.,* 1999). As mentioned before, fracture tests are usually performed under notched specimens. The notch purpose is to concentrate the stress to initiate a crack and then propagate it under a determined path. To select notch size and shape, the following considerations are necessary: the notch has to be sufficiently large to initiate and propagate the crack in a desired path; and the stress intensity factors can be determined from the notch effect interpretation (Roque *et al.,* 1999).

Table 3.5 and 3.6 show the average of the initial and final crack direction after the test was performed for both temperatures. The positive values represent the direction of the crack on the right side from the middle and the negative values represent the left side. Figure 3.10 displays examples of crack initial and final crack after the test for the three-notch configuration tested.

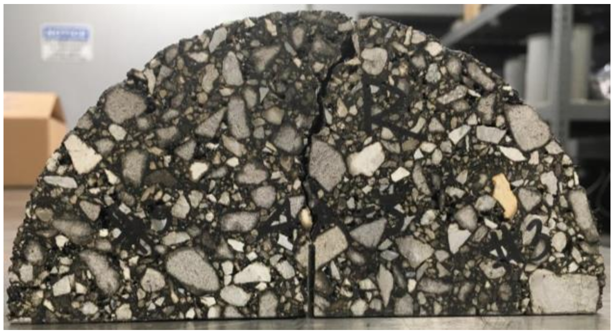

a) Rectangular notch

b) Semi-Circular notch **c) Fatigue Pre-Cracked notch**

Figure 3.10 Crack Propagation for each notch configuration

Figure 3.11 shows the distance from the vertical edge of crack initiation (L) and then the angle of the crack from the vertical axis.

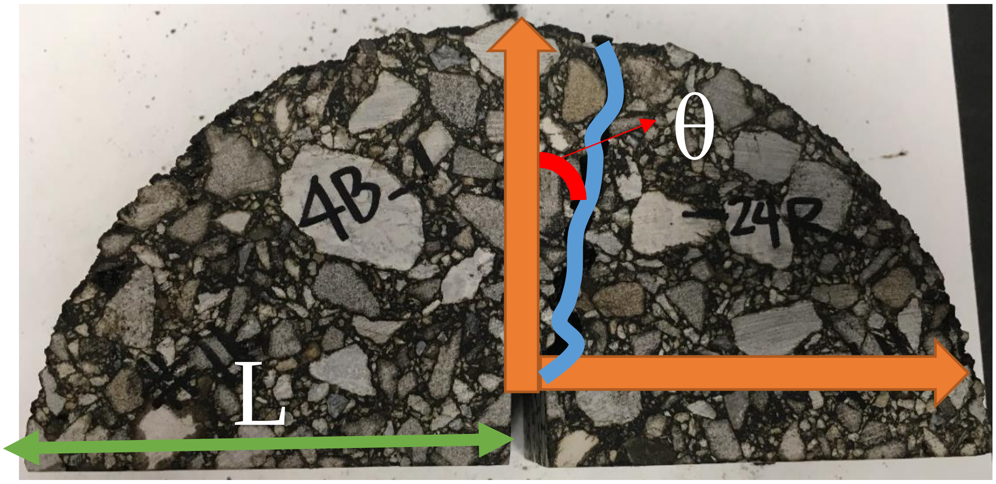

Figure 3.11 Crack Propagation Scheme

Table 3.5 3 Initial and Final Crack Degree for -12°C

	Initial and Final Crack Deviation Degree								
	Rectangular			Semi-Circular			Pre-Cracked		
Thickness	**Initial Angle°**	**Final Angle °**	**Dist. (cm)**	**Initial Angle°**	**Final Angle °**	**Dist. (cm)**	**Initial Angle°**	**Final Angle °**	**Dist. (cm)**
25 mm	7	1	74.8	4	4	77.7	-20	3	74.5
50 mm	10	5	75.9	-18	-2	75.0	-31	-3	74.1
100 mm	-10	0	75.0	-1	3	71.3	20	1	75.7

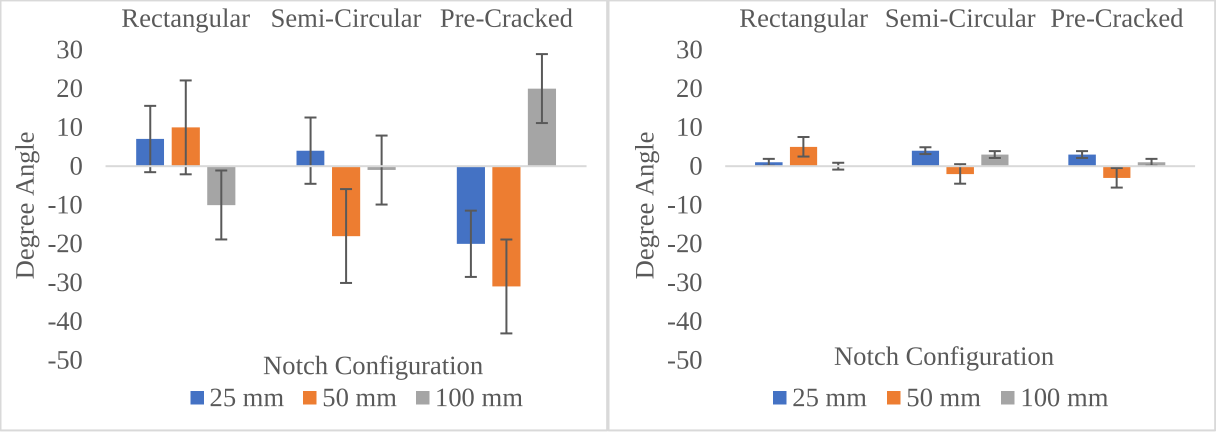

a) **Initial Crack** b) **Final Crack**

Figure 3.12 12 Initial and Final Crack at -12°C

Figure 3.12 plots the initial and final crack from Table 3.3 at -12°C. The results obtained showed that the rectangular notch angle initiation is at least 10° either in the right or left direction. For the semi-circular notch configuration, the highest initial angle is 18° and for fatigue pre-crack notch the initial angle is 31° when the temperature is -12°C.

Table 3.6 Initial and Final Crack Degree for -24°C

	Initial and Final Crack Deviation Degree								
	Rectangular			Semi-Circular			Pre-Cracked		
Thickness	**Initial Angle°**	**Final Angle °**	**Dist. (cm)**	**Initial Angle°**	**Final Angle °**	**Dist. (cm)**	**Initial Angle°**	**Final Angle °**	**Dist. (cm)**
25 mm	4	0	74.8	15	-3	79.0	-9	2	74.0
50 mm	-5	-2	74.8	-5	1	73.0	-12	-1	74.3
100 mm	9	4	75.3	9	5	78.0	4	4	75.7

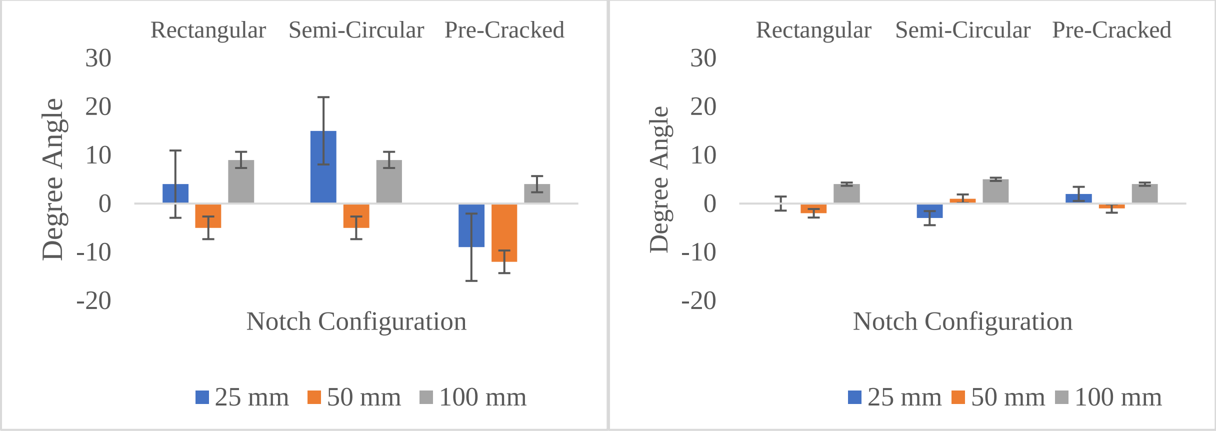

a) Initial Crack **b) Final Crack**

Figure 3.13 Initial and Final Crack at -24°C

Figure 3.13 plots the initial and final crack from Table 3.4 at -24°C. The rectangular notch configuration had the highest initial crack of 9°, the semi-circular notch had 15° and the fatigue pre-cracked notch -12°. For both temperatures, the final crack does not have much angle variability in comparison with the initial crack.

Since the rectangular notch configuration has a shorter range of initial and final, this indicates that the rectangular notch has less possibility of building a cohesive zone in comparison with the other notch configurations. The fatigue pre-cracked notch configuration may have higher values of the angles for initial crack and final since manually stopping the test for each increase of peak load could lead the crack in different directions. Consequently, the semi-circular notch configuration may better display the capture of the fracture energy without restricting the true crack propagation.

3.3.3 ANOVA Analysis

After performing the fracture energy calculations, a general factorial Analysis of Variance (ANOVA) design was used to evaluate the interactions between the variables. This general factorial design happens when there are *a* levels of factor A, *b* levels of factor B, and *c* levels of factor C and so on if there are more factors, which are organized into a factorial experiment with *n* replicates. The minimum number of replicates must be two to apply the sum of squares for accounting the errors into the experimental model. The degree of freedom for each factor is the number of levels minus one, and the degree of freedom for the interaction is the product of the number of degrees from each factor involved (Montgomery, 2009).

For this study, three factors with different number of levels were evaluated, thickness, notch configuration, and temperature, by following the number of levels from Table 3.1. Table 3.7 shows the general factorial design matrix to calculate the ANOVA for the three factors with each degree of freedom.

Where,

Factor A = Thickness (3 levels),

Factor B = Notch Configuration (3 levels),

Factor C = Temperature (2 levels); and

n = Replicates (3)

According to the factorial ANOVA performed in Table 3.7 for SC(B) fracture energy results, thickness has a significant main effect. As shown in the previous results, thickness clearly affects the results of fracture energy. Therefore, it is important to notice that different test methods utilizing different thicknesses are not resulting in the same fracture energy values. This information confirms that the RVE from the different thicknesses are not meeting the requirements necessary, indicating that the material properties are not the same for all the thicknesses.

Table 3.7 ANOVA Factorial Design

Source of Variation	**Sum of Squares**	**Degrees of Freedom**	**Mean Square**	**F_0**	**P-Value**
A, Thickness	29411771.26	2	14705885.6	21.88	**<0.0001**
B, Notch Configuration	3651278.04	2	1825639.0	2.72	0.0797
C, Temperature	2001422.52	1	2001422.5	2.98	0.093
AB	7794522.52	4	1948630.6	2.90	**0.0353**
AC	5424982.37	2	2712491.2	4.03	**0.0262**
BC	3732379.37	2	1866189.7	2.78	0.0756
ABC	3918341.41	4	979585.4	1.46	0.2354
Error	24197791.33	36	672160.9		
Total	80132488.81	53			

Notch configuration and temperature do not have a significant impact on the test in this study. However, the interactions between thickness and notch configuration and thickness and temperature are significant. One reason that the temperature is not significant is that both testing temperatures are low. Also, the binder used was PG 64-22 and the material may behave as elastic at both temperatures.

Interestingly, the notch configuration did not affect because most of the pre-cracked notch configuration samples broke during testing or after reaching the peak load. However, in 2010, Li et al. performed a research to evaluate the notch effect on SC(B) geometry samples, by using three notch lengths: 5, 15, and 30 mm, at three temperatures: -6, -18, -30 °C. From this study, the authors found that there were no significant differences in fracture energy due to the notch length at low temperatures (Li *et al.*, 2010). Since this study was also performed at low temperatures only, the notch configuration may be significant at higher intervals of temperatures.

3.4 Conclusion

The principal objective of this chapter was to evaluate if proper fracture mechanics concepts were applied to the thicknesses and notch configurations used in SC(B) test methods. To perform this assessment, three thicknesses (25, 50 and 100 mm), three notch configurations (rectangular, semi-circular, and fatigue pre-cracked), and two low temperatures (-12 and -24 °C) were used. An NMAS of 12.5 mm, a loading rate of 0.03 mm/min, and an unmodified PG 64-22 binder type were kept constant for this chapter.

The conclusions from this chapter are the following:

- Several factors affect the RVE in an asphalt concrete sample which could be the area of fraction, gradation, orientation and the maximum aggregate size from the mixture. Therefore, a gauge length of 50-60 mm thickness is recommended to be used for a 12.5 mm NMAS since it is the smallest size needed to represent RVE requirements and the plane strain in asphalt concrete.
- Fracture tests are usually performed on notched specimens. Most of the fracture tests in asphalt concrete use a rectangular notch; however, this notch forces the crack to occur in a specific zone. From the results, the rectangular notch had a lower angle

direction for initial crack in comparison with the other notch configurations, which means that it has less possibility to build a cohesive zone.

- A semi-circular notch configuration showed have less cohesive zone and allowed the crack to initiate from a wider range in comparison with the rectangular notch. Hence, this notch configuration was selected for further analysis because of the behavior of the initial crack.

3.5 References

ASTM (2006). Standard Test Method for Linear-Elastic Plane-Strain Fracture Toughness K_{1C} of Metallic Materials. E399-06. West Conshohocken, PA.

Broek, D. (1986). *Elementary Engineering Fracture Mechanics.* Hingham, MA: Kluwer Academic Publishers.

Duan, K., Hu, X., Wittmann, F. (2003). Thickness Effect on Fracture Energy of Cementitious Materials. *Cement and Concrete Research,* 33, pp. 499-507.

Grégorie, D., Rojas-Solano, L., Pijaudier-Cabot, G. (2013). Failure and Size Effect for Notched and Unnotched Concrete Beams. *International Journal for Numerical and Analytical Methods in Geomechanics,* 37, pp. 1434-1452.

Ju, J-B., Jang, J., Kwon, D. (2003). Evaluation of Fracture Toughness by Small-Punch Testing Techniques using Sharp Notched Specimens. *International Journal of Pressure Vessels and Piping,* 80, pp. 221-228.

Kaleemulla, K., Siddeswarappa, B. (2009). Plain Strain Fracture Behavior of Fabric Reinforced Hybrid Composites under varied Notch Configurations. *Journal of Minerals & Materials Characterization & Engineering,* Vol. 8, (No. 6), pp. 495-508.

Kim, Y.R. (2009). *Modeling of Asphalt Concrete.* Reston, VA: McGraw Hill.

Kim, Y-R., Lutif, J., Allen, D. (2009). Determining Representative Volume Elements of Asphalt Concrete Mixtures Without Damage. *Transportation Research Record: Journal of the Transportation Research Board,* No. 2127, pp. 52-59.

Kim, Y-R., Lee, J., Lutif, J. (2010). Geometrical Evaluation and Experimental Verification to Determine Representative Volume Elements of Heterogeneous Asphalt Mixtures. *Journal of Testing and Evaluation,* Vol. 38 (No. 6), pp. 660-666.

Li, X., Marasteanu, M. (2010). Using Semi Circular Bending Test to Evaluate Low Temperature Fracture Resistance for Asphalt Concrete. *Experimental Mechanics,* 50, pp. 867-876.

Liu, P., Chen, J. Lu, G., Wang, D., Oeser, M., Leischner, S. (2019). Numerical Simulation of Crack Propagation in Flexible Asphalt Pavements Based on Cohesive Zone Model Developed from Asphalt Mixtures. *Materials* 12, 1278.

Maher, A., Bennert, T. (2008). Evaluation of Poisson's Ratio for Use in the Mechanistic Empirical Pavement Design Guide (MEPDG). FHWA-NJ-2008-004.

Marzi, S., Biel, A., Stigh, U. (2011). On Experimental Methods to Investigate the Effect of Layer Thickness on the Fracture Behavior of Adhesively Bonded Joints. *International Journal of Adhesion and Adhesives.*

Montgomery, D. (2009). Design and Analysis of Experiments. *John Wiley & Sons, Inc.* 7th Edition, NJ.

NDT Resource Center. (2014). https://www.nde-ed.org

Nsengiyumva, G. (2015). Development of Semi-Circular Bending (SCB) Fracture Test for Bituminous Mixtures. Civil Engineering Theses, Dissertations, and Student Research.

Paulino, G., Song, S., Buttlar, W. (2004). Cohesive Zone Modeling of Fracture in Asphalt Concrete. *Proceedings of the Fifth International RILEM Conference - Cracking in Pavements: Mitigation, Risk Assessment, and Preservation*, pp. 63-70.

Romero, P., and Masad, E. (2001). Relationship Between the Representative Volume Element and Mechanical Properties of Asphalt Concrete. *Journal of Materials in Civil Engineering*, Vol. 28 (No. 8), pp. 77-84.

Roque, R., Zhang, Z., Sankar, B. (1999). Determination of Crack Growth Rate Parameters of Asphalt Mixtures Using the Superpave IDT. *Presentation at the Annual Meeting of the Association of Asphalt Paving Technologists.*

Smith, S., Morales, A., Braham, A. (2019). Evaluating Aggregate Size Effects on Dynamic Modulus Using Gray Scale Analysis, submitted to Asphalt Paving Technology: *Journal of the Association of Asphalt Paving Technologist*.

Song, S., Paulino, G., Buttlar, W. (2005). Simulation of Crack Propagation in Asphalt Concrete Using an Intrinsic Cohesive Zone Model. *Journal of Engineering Mechanics,* Vol. 132, No. 11, pp. 1215-1223.

Wright, T., Hayes, W. (1977). Fracture Mechanics Parameters for Compact Bone-Effects of Density and Specimen Thickness. *J. Biomechanics,* Vol. 10, pp. 419-430.

Wittman, F., Mihashi, H., Nomura, N. (1990). Size Effect on Fracture Energy of Concrete. *Engineering Fracture Mechanics,* 35, pp. 107-115.

Wu, J., Chew, S. (2014). Field Performance and Numerical Modeling of Multi-Layer Pavement System subject to Blast Load. *Construction and Building Materials,* 52, pp. 177-188.

Chapter 4 Developing a Master Curve for SC(B) test to Evaluate Cracking Resistance using Fracture Energy versus Loading Rate*[2]

Abstract

One of the principal distresses to consider in asphalt concrete is cracking; therefore, multiple fracture tests have been developed to quantify cracking resistance. Likewise, cracking parameters such as loading rate and testing temperature, which have been used to assess asphalt pavements in the test methods, are different. This study looks to evaluate the fracture behavior by testing at four temperatures (-12, 0, 12, 25 ˚C), five loading rates (0.03, 0.5, 1.0, 30.0, and 50.0 mm/min), two binder types (PG 64-22 and PG 76-22), and two NMAS (9.5 and 25 mm) by keeping constant other factors such as 50 mm thickness and a semi-circular notch configuration. After capturing fracture energy at different loading rates and testing temperatures, a preliminary master curve was built following the dynamic modulus master curve steps to characterize cracking in asphalt concrete across the range of temperatures and loading rates. This master curve was plotted with the fracture energy versus reduced loading rate. However, a sigmoidal function was not obtained, instead, a parabolic shape was found in the initial fracture analysis for each set of temperature when increasing the loading rate, which was defined as local fracture energy. From the local fracture energy, the peak values were plotted for each testing temperatures and this was defined as global fracture energy. As a result, for 9.5 NMAS, the peak fracture energy obtained was 3,611 J/m^2 for PG 64-22 at 10 ˚C and 4,723 J/m^2 for PG 76-22 at 7 ˚C. However, for 25 mm NMAS, the peak fracture energy obtained was 2,118 J/m^2 for PG 64-22 at 7˚C and 2,762 J/m^2 for PG 76-22 at 25 ˚C, which could mean that the maximum fracture for 25mm NMAS PG 76-22 may be in a higher testing temperature and loading rate.

2* Technical article to be submitted to the International Journal on Road Materials and Pavement Design in August 2020

Keywords: loading rate, temperature, fracture energy, asphalt concrete, master curve.

4.1 Introduction

Cracking exists in asphalt concrete because of various factors such as material properties, environmental conditions, traffic loads, and construction practices. Therefore, multiple cracking tests have been developed by agencies (Zhou *et al*., 2016). Many of these cracking tests are performed using a Semi-Circular Bend SC(B) geometry and fracture energy is calculated to quantify the cracking resistance. However, some of the parameters used, such as temperature and loading, are different. Asphalt concrete is a viscoelastic material that depends on time and temperature. For instance, asphalt concrete at higher temperatures behaves as a viscous material and at intermediate temperatures, it is more likely for a cracking failure to occur. However, at lower temperatures, the material is more brittle due to the crack initiation and propagation in these conditions (Fakhri *et al*., 2018).

There is a concern that the methods used to obtain the true fracture process may not be accurate and the results are affected due to the material viscoelasticity and the size effect. Multiple approaches have adopted low-temperature conditions where the type of fracture is more brittle, but the fatigue cracking is observed at intermediate temperatures. Therefore, in 2012 a study performed by Aragão et al. was made to study nine loading rates: 1, 5, 10, 25, 50, 100, 200, 400 and 600 mm/min at a testing temperature of 21°C. Figure 4.1 shows the plots of force versus loading time of the test performed for each of the loading rates applied where the authors were trying to calibrate their models with existing test results. This plot is a good example of how multiple loading rates applied behave. For example, the results experience higher peak loads for faster loading rates and lower loading times of the test performed (Aragão *et al*., 2012).

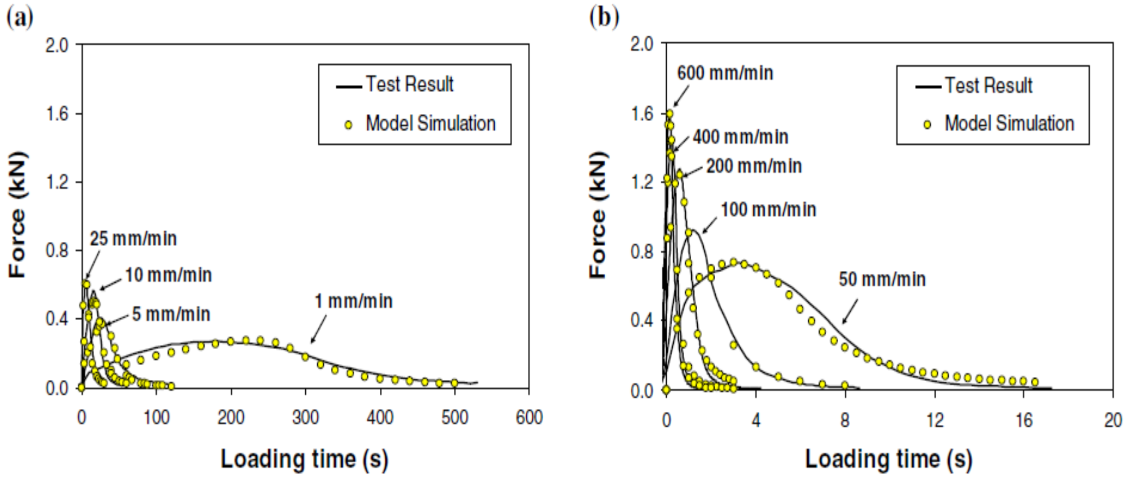

Figure 4.1 Loading Rate Effect (Aragão et al., 2012)

In 2010, a study performed by Li et al., at low temperatures and slow loading rates, three loading rates were tested: 0.009, 0.03 and 0.3 mm/min, in this same order the loading rates are plotted, and three testing temperatures were used: -30, -18, and -6 °C. Figure 4.2 shows fracture energy plotted versus loading rate level, where the fracture energy increases with the decreasing of the loading rate. Testing temperature has a significant influence on fracture energy when the temperature starts to decrease. Another observation is that at -6 °C, in comparison with the other testing temperatures, the loading rate has a higher influence in the fracture energy. For all the testing temperatures, the fracture energy had a major change from level 1 to 2. This could be due to the ductility of the material at higher temperatures and it is more depended on the loading rate in those conditions. For -30 and -18 °C, these temperatures represent the brittle properties on the material, and the mixture does not depend on the loading rate (Li *et al*., 2010).

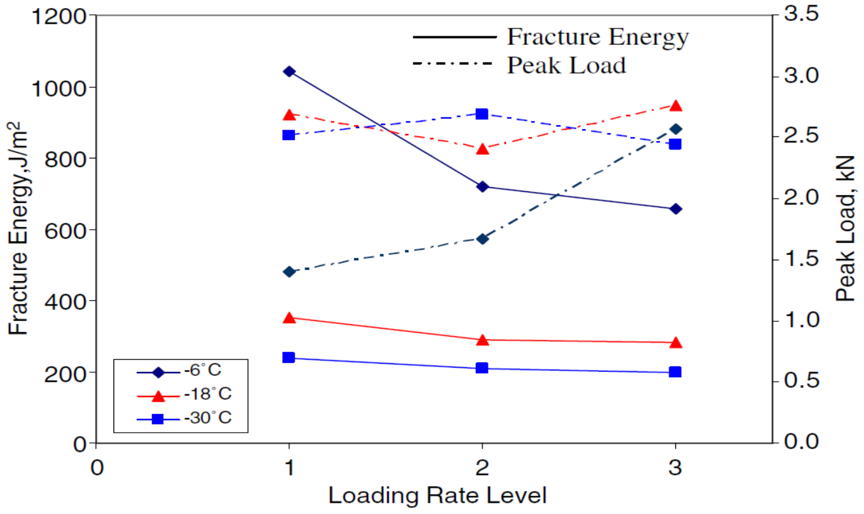

Figure 4.2 Influence of Loading Rate (Li et al., 2010)

Like fracture energy, the Dynamic Modulus |E*| of asphalt concrete is another material property measured at many different loading rates and testing temperatures. To characterize the stiffness of asphalt at the range of loading rates and temperature tested, the concept of time-temperature superposition is used to create a master curve that displays material behavior in each of these conditions. Because there is also variation in proposed testing temperatures and loading rates for cracking tests, this same concept of time-temperature superposition may be relevant for evaluating the influence of each of these conditions.

4.1.1 Time-Temperature Superposition Principle

Because asphalt concrete is a viscoelastic material, its behavior changes depending on the temperature. Time and temperature are functions of viscoelastic properties such as relaxation modulus, dynamic modulus, phase angle and creep compliance. The concept of Time-Temperature Superposition is used in experimental measurements of viscoelastic properties with different frequencies and temperatures to obtain two relationships: a master curve and a shift function-temperature curve. A master curve illustrates the viscoelastic property by plotting it at a reference temperature against time or frequency. The master curve describes how the material depends on the frequency modeled with a sigmoidal function. Moreover, a shift function-temperature curve illustrates the ratio between the real-time the test was performed and the reference time the data has been shifted versus the temperature in real time. The shift function-temperature describes how the material depends on the temperature to form the master curve (Papagiannakis *et al.,* 2008, Zhu *et al*., 2011).

In asphalt concrete, a master curve is used to analyze the Dynamic Modulus |E*| results from a complex modulus test. The importance of the master curve is to compare asphalt concrete performance with other mixtures at a range of temperatures and frequencies (Clyne *et al.,* 2003). Some of the uses for Dynamic Modulus are to characterize the stress/strain behavior in asphalt concrete which mimics the traffic loads and the deformation in the pavement. Also, Dynamic Modulus is used as an input in the PavementME Design and it is an indicator of rutting and cracking in the pavement structure. The test method used to obtain Dynamic Modulus |E*| is found in AASHTO T 342. In this test six frequencies are used: 0.1, 0.5, 1.0, 5.0, 10, and 25 Hz and tested at five temperatures: -10, 4.4, 21.1, 37.8, and 54 °C (Yang *et al.,* 2017a). Usually, the test is performed in a 150 mm tall and 100 mm diameter sample. However, in 2004 an alternate method, indirect tension test (IDT), was proposed by Kim et al. to use a 150 mm diameter and 38 mm thickness sample (Kim *et al.,* 2004).

4.1.2 Research Objective

The focus of this chapter is to obtain fracture energy using the AASHTO TP 105 test methods to evaluate some factors as loading rate and testing temperature with the time-temperature superposition concept. The objectives of this chapter are to:

- Evaluate the fracture behavior by performing AASHTO TP 105 test at different temperatures: -12, 0, 12, 25 ˚C, loading rates: 0.03, 0.5, 1.0, 30.0, and 50.0 mm/min, binder types: PG 64-22 and PG 76-22, and NMAS: 9.5 and 25 mm.
- Investigate fracture behavior by plotting fracture energy versus loading rate at different temperatures to have a better understanding of time-temperature superposition that is applied in asphalt concrete because of its viscoelastic properties.

4.2 Materials and Methods

4.2.1 Materials

Since the focus of the study is to develop a master curve for fracture resistance, two mix designs were used. A 9.5 mm and a 25.0 mm nominal maximum aggregate size (NMAS) limestone aggregates, which mix gradations are common in the state of Arkansas, were selected. A 9.5 mm NMAS is typically used as a surface mix; whereas a 25 mm NMAS is used as a binder mix. The differences between these NMAS gives a wider range to make comparisons when plotting a master curve. Both NMAS were mixed with a PG 64-22 unmodified binder and a PG 76-22 modified binder. As for NMAS, one modified and an unmodified binder were selected to evaluate the influences in fracture energy when applying the master curve concept. Since the binder content is the same for each aggregate size and binder type, the effective binder content was calculated. For the 9.5 mm NMAS the binder content was 5.3% and the effective binder was 4.30% for both binder types, and for 25 mm NMAS, for both binders types the binder content was 3.7%, and the effective binder was 2.85% for PG 64-22, and 3.08% for PG 76-22 as shown in Table 4.1. The differences between the effective binder effect in the 25 mm NMAS could lead to brittle problems in the pavement (Chadbourn *et al.*, 1999). The samples were mixed following the short-term conditioning for mixture mechanical property testing from AASHTO R 30 and compacted at 7% air voids.

Table 4.1 Asphalt Binder Content

NMAS	Binder Type	Binder Content (%)	Effective Binder Content (%)
9.5 mm	PG 64-22	5.3	4.30
	PG 76-22	5.3	4.30
25 mm	PG 64-22	3.7	2.85
	PG 76-22	3.7	3.08

4.2.2 Test Methods

The main output of this research is the fracture energy, which is defined as the energy necessary to produce a unit surface crack area and can be calculated by dividing the work of fracture (W_f), which is the area under the load versus LLD plot, by the ligament area of the specimen (A_{lig}) as shown in Equation 4.1. The unit of fracture energy is J/m^2.

$$G_f = \frac{W_f}{A_{lig}} \qquad \text{(Eq. 4.1)}$$

To obtain fracture energy, the SC(B) test was performed following the AASHTO TP 105 specification at four temperatures: -12, 0, 12, and 25 ˚C, with five loading rates of 0.03, 0.5, 1.0, 30.0, and 50.0 mm/min. These testing temperatures and loading rates were selected from previous research performed in fracture resistance which shows four different tests with test temperatures and loading rates that are used in the asphalt concrete field. Note how the testing temperatures and loading rates were chosen to encompass the testing temperatures and loading rates from four test that uses an SC(B) geometry and it was successful for all loading rates and testing temperatures except for the -24 ºC used in AASHTO TP 105-13. A summary of each of these test methods is as follows:

- AASHTO TP 105: Cracking at low temperatures characterize the distresses in asphalt pavements around the northern US and Canada. AASHTO TP 105 is performed at low temperatures because of the need to study fracture resistance due to thermal cracking (Li *et al.,* 2006). Moreover, a study showed that micro-cracks are formed at lower temperatures of the PG lower limit. For a PG 64-22, the temperatures used to test the samples are -24 ºC and -12 ºC (Li *et al.*, 2004). The determination of the loading rate value of 0.03 mm/min is not specified in the study.
- AASHTO TP 124: Proposed to evaluate reclaimed asphalt pavement (RAP) and recycled asphalt shingles (RAS). The intermediate temperature of 25 ºC was chosen because the peak load values were obtained at that temperature in comparison with other temperatures tested. Because the temperature increases, the loading rate increases; therefore, a fast loading rate of 50 mm/min was selected. At lower temperature, fracture energy seems to be less rate-dependent than at intermediate temperatures (Al-Qadi *et al.,* 2015).
- Louisiana Transportation Research Center (LTRC) Method: Evaluates the critical strain energy release rate (J_c) in asphalt concrete. This test is performed at intermediate temperatures such as 25 °C with a loading rate of 0.5 mm/min. In comparison with the other tests, three notch depths are tested: 25.4, 31.8, and 38 mm (Cooper III *et al.,* 2016).
- Fénix test: Quantifies the dissipated energy during the process of cracking, which benefits energy evaluation in asphalt concrete cracking resistance. The difference with other cracking tests is that around the cracking area, the Fénix test generates tensile stresses at a loading rate of 1 mm/min. For testing, low and intermediate temperatures such as -10 ºC, 5 ºC, and 20 ºC were proposed (Perez-Jimenez *et al.,* 2010).

As seen in the previous test methods, the thickness of each sample is variable. Therefore, the findings of Chapter 3 were utilized to choose a 50-mm thickness for the testing in Chapter 4. Also, all the tests mentioned utilize a rectangular notch. Again, the findings from Chapter 3 recommended the use of semi-circular notch, therefore, this notch geometry will be used in Chapter 4. Three replicates were made for each combination of PG grade, NMAS, loading rate, and testing temperature. Table 4.2 shows the experimental matrix for this study in which the SC(B) specification evaluation will provide data for the development of a fracture energy master curve for asphalt concrete. The steps of the master curve development are detailed in Chapter 1 in the 1.5.3 section.

Table 4.2 Experimental Matrix

Factors	Number of Levels	Level Value
Binder Type	2	PG 64-22, PG 76-22
NMAS	2	9.5, and 25 mm
Loading Rate	5	0.03, 0.5, 1.0, 30.0, and 50.0 mm/min
Temperature	4	-12, 0, 12, and 25˚C
Thickness	1	50 mm
Notch Configuration	1	Semi-Circular

4.3 Results and Discussion

A fracture energy analysis was conducted to assess the effects of cracking resistance on different types of materials and testing conditions. The factors contemplated were NMAS, loading rate, testing temperature, and binder type. Below, an analysis of cracking behavior is made by measuring the fracture energy and then a master curve by plotting fracture energy versus loading rate is intended to be developed to characterize cracking.

4.3.1 Fracture Energy

Figure 4.3 shows the average fracture energy from three replicates tested for each combination of temperature and loading rate from a 9.5 mm NMAS for both PG 64-22 and PG 76-

22 binder. Figure 4.4 presents the effect of 25 mm NMAS for both binder types. As mentioned, each of the temperatures and loading rates tested are obtained from asphalt concrete cracking tests that use an SC(B) geometry with a sample thickness of 50 mm and a semi-circular notch. As expected, the fracture energy calculated for these combinations is not the same for each loading rate or temperature. Fakhri et al. (2018) obtained different fracture energy results while using different loading rates. For instance, at higher testing temperatures, when the loading rate increased, the fracture energy increased as well. One explanation is that at lower temperatures the material is brittle, so after reaching the maximum fracture energy value, it drops because the crack did not have enough time to heal under the loading rates. On the other hand, at higher temperatures, the crack has more time to heal so the fracture energy increases as the loading rate increases, which may be caused by the asphalt binder behavior. In this research, a similar pattern happens for low temperatures (-12 and 0 ˚C). The loading rate increases and the fracture energy starts dropping when it reaches the maximum value. Additionally, for a higher temperature such as 25 ˚C the fracture energy increases as the loading rate does. However, at 12 ˚C the data experiences the same trend as low temperatures except for 9.5 mm PG 76-22 which can be considered a transition temperature between low temperatures and high temperatures. With this information obtained, in the following section, a master curve is expected to be developed by plotting the fracture energy versus loading rates for each of the testing temperatures.

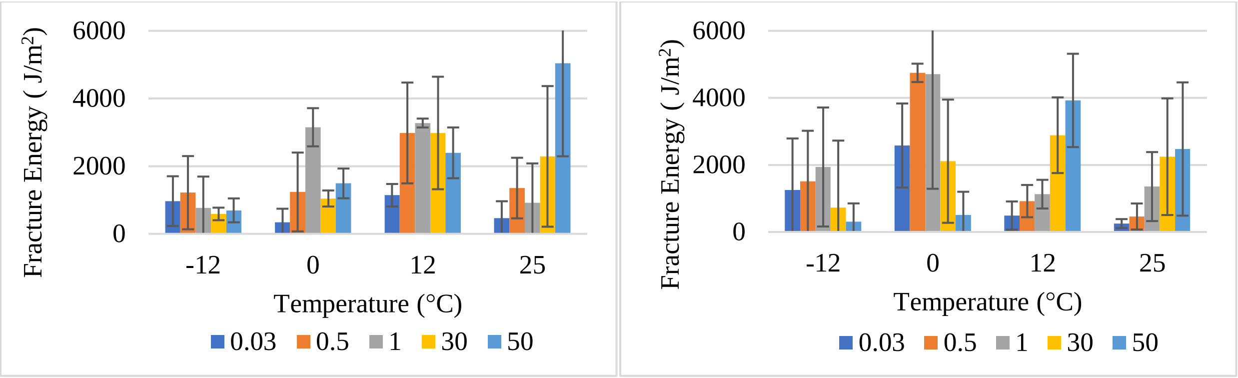

a) 9.5 mm PG 64-22 **b) 9.5 mm PG 76-22**

Figure 4.3 Effects of 9.5 mm fracture energy at different temperatures

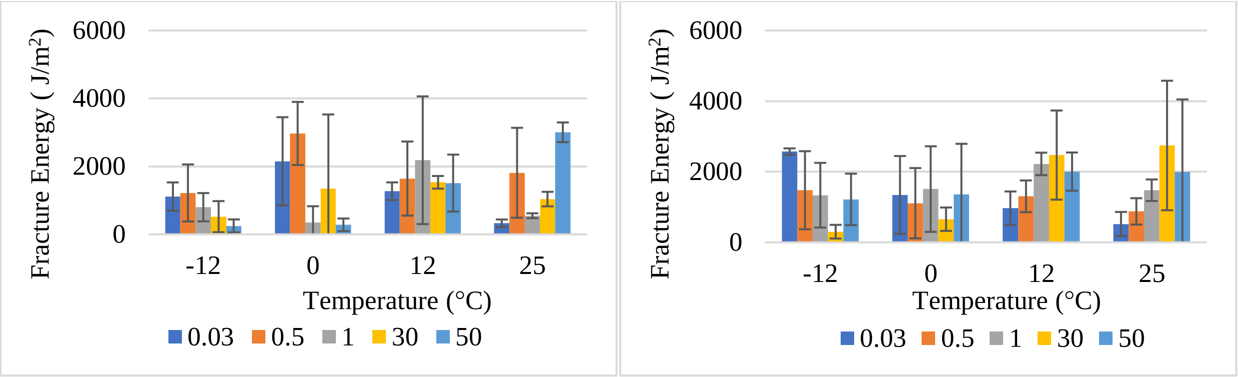

a) 25 mm PG 64-22 **b) 25 mm PG 76-22**

Figure 4.4 Effects of 25 mm fracture energy at different temperatures

4.3.2 Master Curves

Master curves are usually developed using the values of Dynamic Modulus |E*| which are obtained when testing at different temperatures and frequencies to analyze the effects of these factors on asphalt concrete. Because asphalt concrete is a viscoelastic material, it depends on temperature and loading rate to characterize the stiffness and consequently the time-temperature superposition concept is used (Bayane *et al.*, 2017). In this chapter, the factors of testing temperature and loading rate were applied when calculating fracture energy. After analyzing cracking resistance parameters in the previous section, a master curve is intended to be used to evaluate the behavior of asphalt concrete at low and intermediate temperatures by applying multiple loading rates by following the steps used in the Dynamic Modulus |E*| master curve fabrication. Figure 4.5 shows a preliminary fracture energy master curve for 9.5 mm NMAS and PG 64-22 binder type. The reference temperature used for this master curve was 25 ˚C but for the other mixtures, the master curves were better fitted at -12 ˚C. The master curve was built following the AASHTO R 62-13 specification for Dynamic Modulus |E*|.

From this first graph, the fracture energy calculated from 0 ˚C and 25 ˚C overlap but do not follow the same order as Dynamic Modulus |E*| from having at low temperatures higher |E*| values than for high temperatures. However, in 2017 a research performed by Zhu et al. found that the fracture energy increase as the test temperature increases (Zhu *et al.*, 2017). Thus, this behavior is followed in Figure 4.5 which is the opposite when comparing with the Dynamic Modulus |E*|, where the modulus decreases with the increase of test temperature. Additionally, the S-shaped from the sigmoidal function that is expected to be obtained in the master curve is not delineated in this graph. Moreover, Figure 4.6 does start from high temperatures to low temperatures as Dynamic Modulus |E*|, but the curve does not delineate an S-shaped as the sigmoidal function. At the same time, Figure 4.7a does not display an S-shaped curve to describe the characteristics of that mixture. Finally, Figure 4.7b plots a straighter line than a curve which increases from left to right.

In 2015, AlQadi et al., performed research on testing temperature (-30 to 30 ˚C) and loading rates (5 to 100 mm/min) selecting only two loading rates, a slower and a faster rate, to determine the effect on fracture energy. The authors found that the application of time-temperature superposition on fracture energy can be valid for certain testing temperature either at high displacement rates or lower testing temperatures. Also, most of the peak fracture energy values were obtained at a temperature of 25 ˚C (AlQadi *et al.*, 2015).

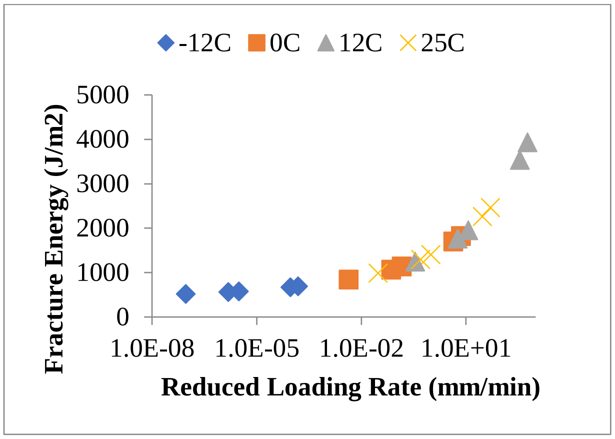

Figure 4.5 Fracture Energy Master Curve for 9.5 mm PG 64-22 using Time-Temperature Superposition at a 25 ˚C Reference Temperature

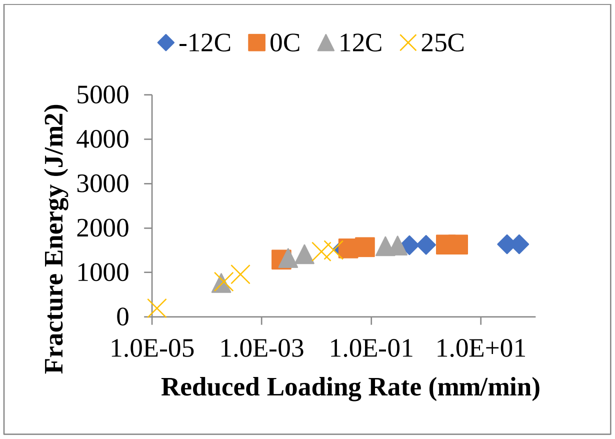

Figure 4.6 Fracture Energy Master Curve for 9.5 mm PG 76-22 using Time-Temperature Superposition at a -12 ˚C Reference Temperature

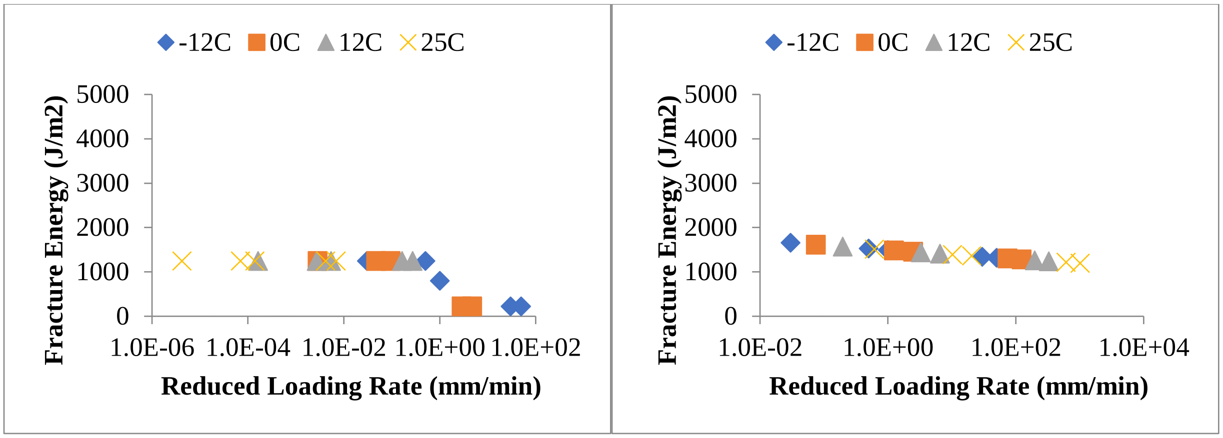

a) 25 mm PG 64-22 **b) 25 mm PG 76-22**

Figure 4.7 Fracture Energy Master Curve for 25mm using Time-Temperature Superposition at a -12 ˚C Reference Temperature

Since the master curves plotted did not give any similar trending or helpful information about cracking behavior, another method was applied after observing the trending in Figures 4.3 and 4.4. From those figures, a parabolic trending was observed on each of the testing temperatures and in the whole combination of testing temperatures and loading rates. The next section explains the concept of local and global fracture energy which is a different way to describe the cracking behavior.

4.3.3 Local and Global Fracture Energy

After evaluating the results when plotting the master curves in the previous figures, the procedure for Dynamic Modulus |E*| did not show any trending that can describe the cracking behavior. However, when looking at the graphs of the fracture energy (Fig. 4.8 and 4.9) obtained for different loading rates and testing temperatures, a parabolic shape can be seen for both a testing temperature and five loading rates, which we defined as “local” fracture energy, and for the whole combination of four testing temperature and five loading rates, which we defined as “global” fracture energy. Therefore, we explored building a master curve for cracking by developing both local and global parabolic relationships instead of continuing to explore the more traditional sigmoidal function.

The first step of the analysis consisted of simply drawing general parabolic shapes for both the local and global fracture energy, to determine if there was merit in a more comprehensive analysis. When analyzing Figure 4.8a for 9.5 mm PG 64-22, the peak of each of the local parabolas starts increasing with the testing temperature. This means that the global parabola shows the local maximum fracture energy at any given temperature. On the other hand, Figure 4.8b for 9.5 mm PG76-22 behaves differently because a second global parabolic shape can be observed, having a peak on the 0˚C temperature. This behavior could be due to the polymer that is acting and shifting from the unmodified binder.

Finally, when looking at Figure 4.9 for 25 mm, the larger aggregate seems to dominate the fracture behavior instead of the binder type because the trends are not similar as in Figure 4.8. In this case, the peak value for fracture energy for each local parabola is not that different as for Figure 4.8. With the general trends of a parabolic relationship established, a more robust, calculation of each of the local and global parabolas was pursued.

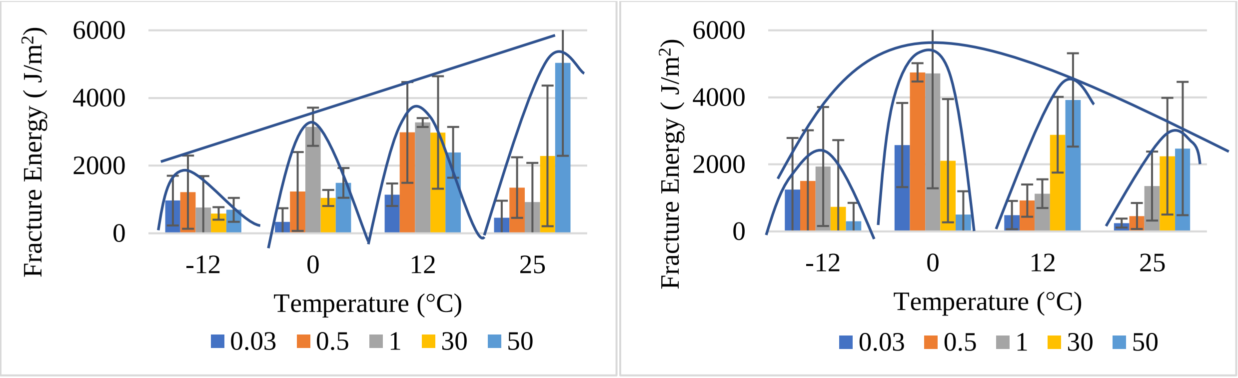

a) 9.5 mm PG 64-22 **b) 9.5 mm PG 76-22**

Figure 4.8 Effects on 9.5 mm fracture energy at different temperatures

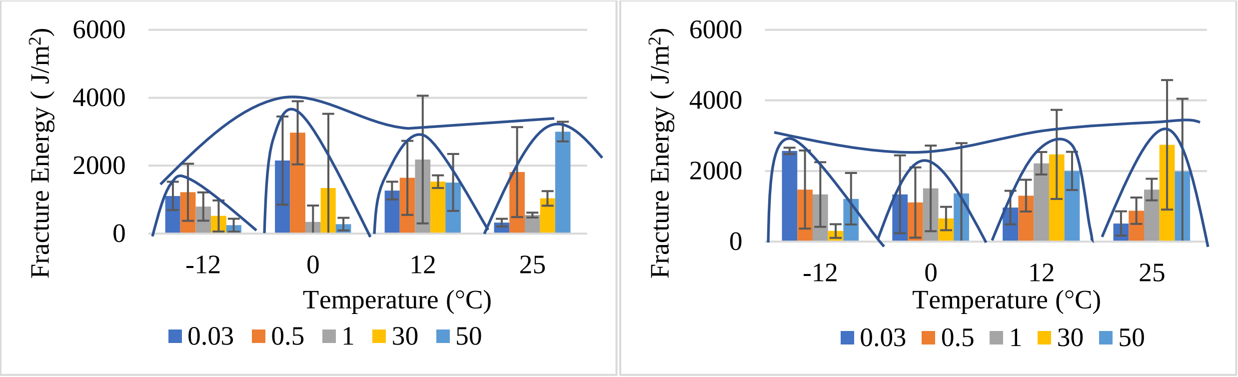

a) 25 mm PG 64-22 **b) 25 mm PG 76-22**

Figure 4.9 Effects on 25 mm fracture energy at different temperatures

4.3.3.1 Local Fracture Energy

The local fracture energy is defined as the fracture energy found in the parabolic shape in a specific testing temperature where the fracture energy is plotted versus the loading rate. For the calculation of the local fracture energy parabola, the following steps were done:

- First, three parabolas were plotted on each of the local zones, one of them is the average fracture energy obtained from three replicates tested, and the other two are the maximum and minimum values obtained from the standard deviation.
- The local fracture energy was plotted versus the loading rates for each testing temperature, as can be seen in Figure 4.10.
- Then, a second-degree parabola was fitted to the initial plotted parabolas.
- Finally, from the fitted parabolas, a second-degree equation was obtained to calculate the local fracture energy maximum value, by using the first derivate from the equation from each testing temperature to plot the global fracture energy.

When plotting these parabolas along the local fracture energy, some local zones were easier to correlate to the second-degree equation than others. For instance, Figure 4.10 shows the local fracture energy parabolas for two NMAS using a PG 64-22 binder type. In Figure 4.10a, the local fracture energy plotted from 9.5 mm PG 64-22 at 0 °C display three parabolas that can be easily fitted into a second-degree equation. The correlation from these parabolas were between 0.70 and 0.99. However, in Figure 4.10b, the local fracture energy plotted for a 25 mm PG 64-22 at 25 °C display three fitted parabolas that are harder to correlate to a second-degree parabola. The correlation from these parabolas were between 0.10 and 0.70. In this case, for 4.10b, applying the first derivate of the parabola would have gotten the minimum value from the parabola instead of the maximum because of the shape of the parabola. Therefore, in this case, the maximum local fracture energy value was obtained by plugging into the second-degree equation the value of the loading rate that gave the highest fracture energy value from the initial parabola.

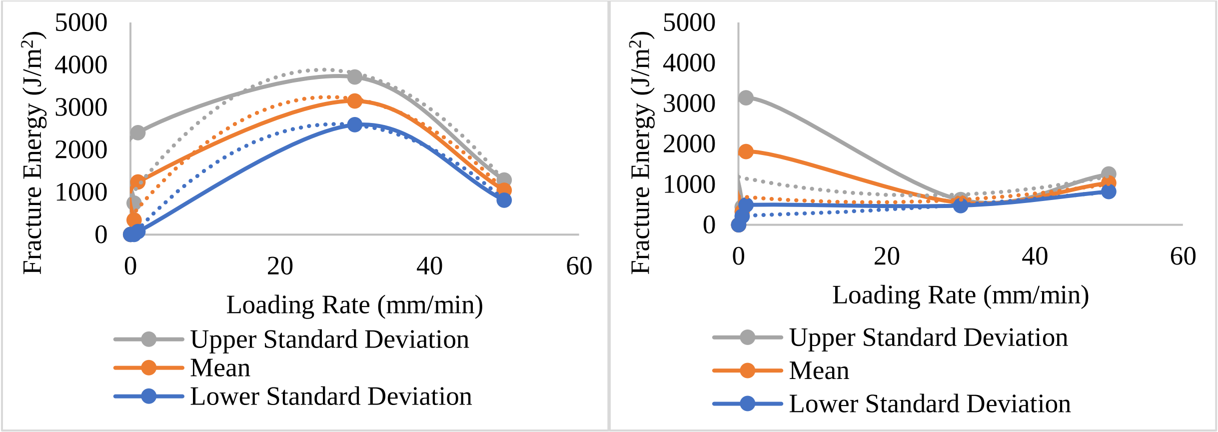

a) 9.5 mm PG 64-22 at 0 °C **b) 25 mm PG 64-22 at 25 °C**

Figure 4.10 Local Fracture Energy Parabolas

Table 4.3 shows the local maximum values and the loading rates at which the maximum value occurred from the average fitted parabolas from each testing temperature for all the combinations of NMAS and binder type. From this table, the global fracture energy parabolas were built.

Table 4.3 Local maximum values from fitted parabola (LR is loading rate)

Temp °C	**Fracture Energy (J/m^2)**							
	9.5 mm				**25 mm**			
	PG 64-22	**LR (mm/min)**	**PG 76-22**	**LR (mm/min)**	**PG 64-22**	**LR (mm/min)**	**PG 76-22**	**LR (mm/min)**
-12	840	20.45	2061	24.29	898	18.64	2571	11.76
0	3240	26.54	5036	24.47	1723	0.03	1361	24.07
12	3419	33.91	3916	50.00	2246	28.68	965	45.32
25	2269	50.00	2486	44.66	1010	50.00	1991	50.00

Figure 4.11 shows the influence of binder type and NMAS on fracture energy for the local maximum values obtained from Table 4.3. in Figure 4.11a, fracture energy was plotted to keep the same NMAS and varying the binder type. The results showed that all the values of 9.5 mm fall below the equality line on PG 76-22 which means that the modified binder has an influence on fracture energy on this NMAS at all the testing temperatures performed on this study. Specifically, the values from the testing temperatures at 12 and 25 °C are closer to the equality line than the other two points, which means there is more agreement between the binder type on intermediate temperatures. However, for 25 mm only half of the values are below the equality line for the testing temperatures at -12 and 25 °C.

In Figure 4.11b, fracture energy was plotted to keep the same binder type and to vary the NMAS. Most of the points fall above the equality line on the 9.5 mm NMAS, which means that the smaller aggregate has a higher local fracture energy than the 25 mm. However, one point for fracture energy PG 64-22 at -12 °C falls on the equality line on both NMAS and only one point for 25 mm NMAS at -12 °C falls closer the equality line, which could mean that at low temperature (-12°C) there is more agreement on the NMAS.

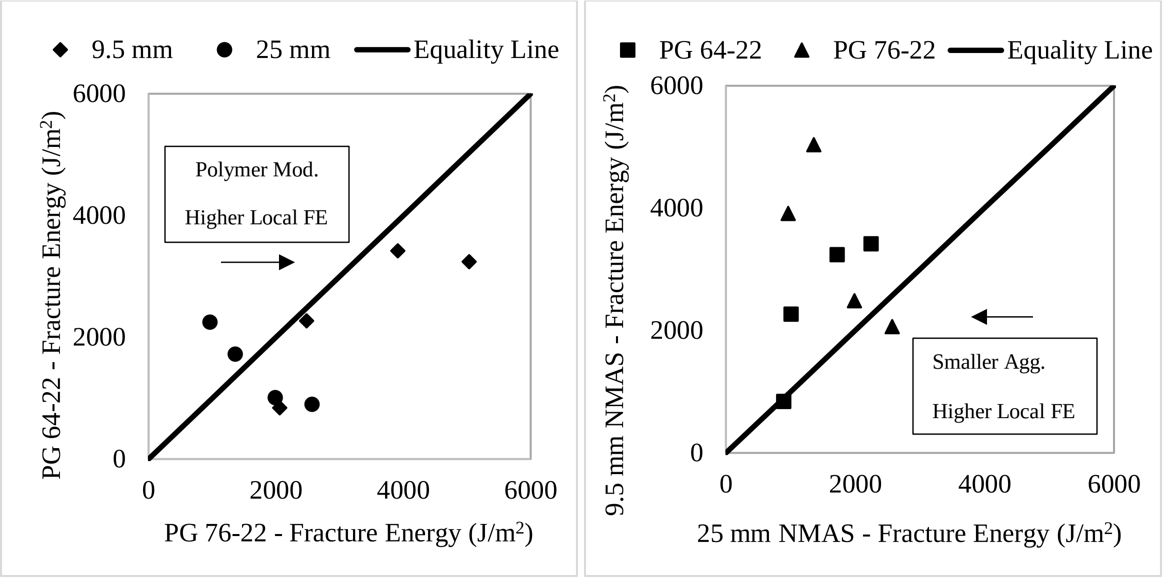

a) Binder type **b) NMAS**

Figure 4.11 Binder Type and NMAS influence on Fracture Energy from local maximum values

Figure 4.12 shows the influence of binder type and NMAS on the loading rate. In Figure 4.12a, the peak loading rate from the maximum local fracture energy was plotted to keep the same NMAS and varying the binder type. The results show only one point of 25 mm NMAS falls on the equality line which is at 25 °C and two points from 9.5 mm are close to the equality line. Most of the points fall below the equality line which means the polymer modified binder has a higher influence on the loading rate.

In Figure 4.12b, the peak loading rate from the maximum fracture energy was plotted to keep the same binder type and varying the NMAS. Most of the points fall above the equality line which means the 9.5 mm has a higher influence on the loading rate. Also, there is more agreement for 9.5 mm NMAS except for the point at 0 °C. In general, there is a trend of increasing the loading rate with the testing temperature except for the 25 mm NMAS value on 0°C.

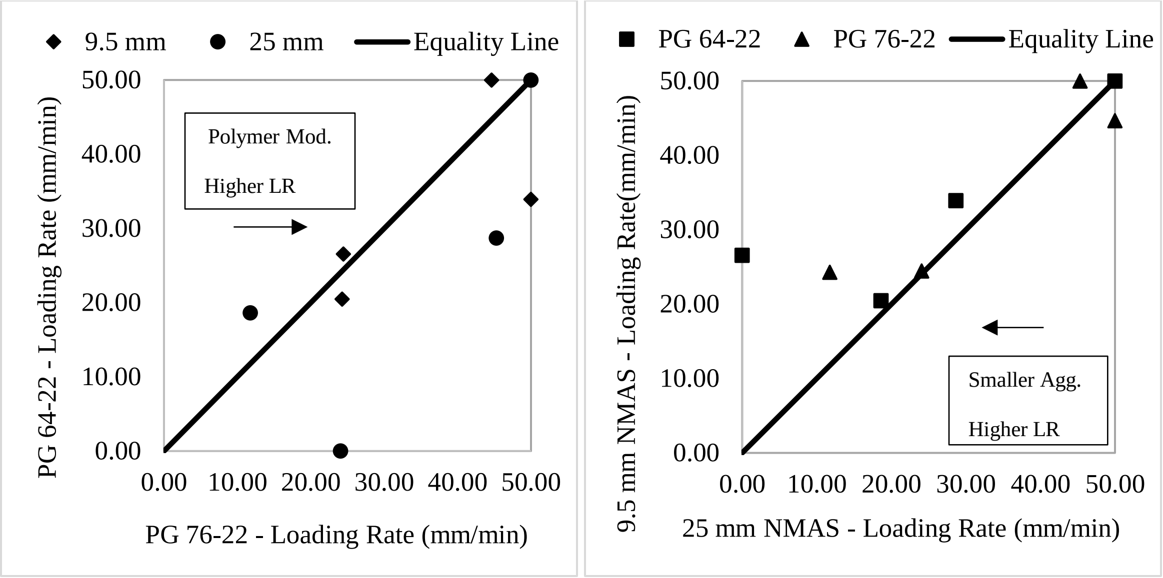

a) Binder Type **b) NMAS**

Figure 4.12 Binder Type and NMAS influence on Loading Rate from local maximum values

The equations and figures of these local fracture energy parabolas for all the testing temperatures and loading rates are going to be presented in Appendix B, but the equations and figures of the global parabolas are going to be analyzed in this chapter in the following sub-section.

4.3.3.2 Global Fracture Energy

The global fracture energy is defined as the whole combinations of testing temperatures and loading rates. The following steps were performed to obtain the global fracture energy parabolas:

- To build global fracture energy, the maximum fracture energy was obtained from the local fracture energy, as seen in Table 4.3.
- The maximum fracture energy was plotted versus the testing temperature as seen in Figure 4.13 and 4.14.

- Then, a second-degree parabola was fitted to the initial global fracture energy parabolas;
- From this fitted parabola, a second-degree equation was obtained which represents the four testing temperatures and the five loading rates for each material type depending on the NMAS and the binder type from this research.

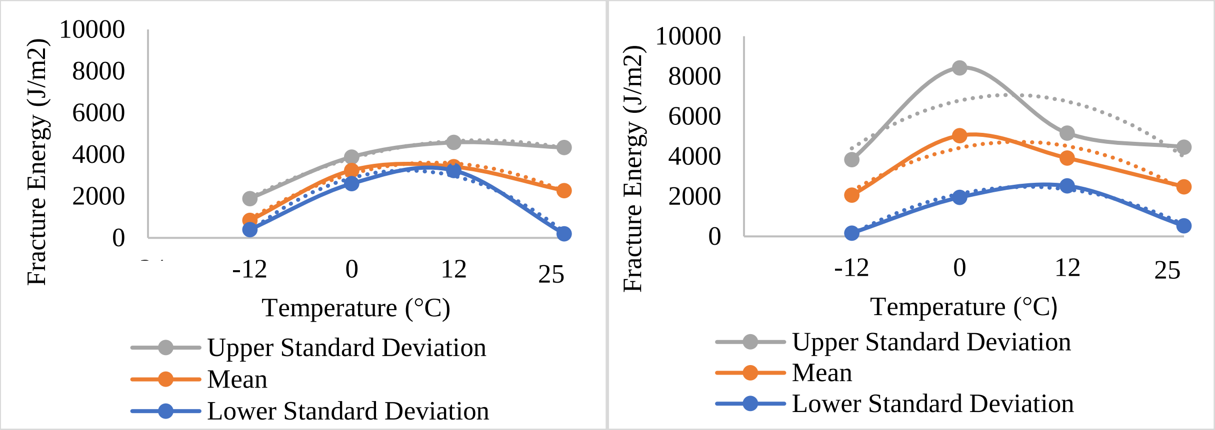

a) 9.5 mm PG 64-22 **b) 9.5 mm PG 76-22**

Figure 4.13 9.5 mm NMAS Global Parabola

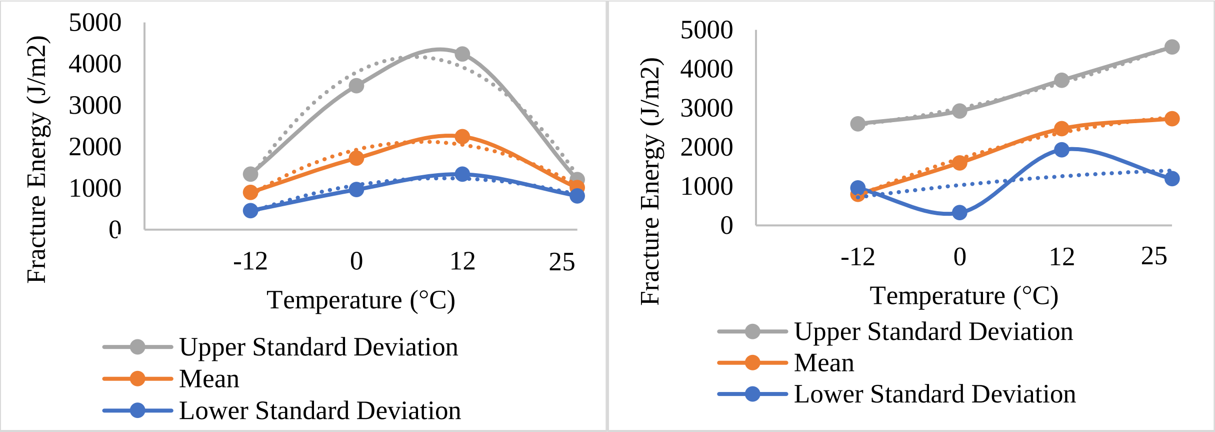

a) 25 mm PG 64-22 **b) 25 mm PG 76-22**

Figure 4.14 25 mm NMAS Global Parabola

Figure 4.13 is the representation of the global fitted parabolas for all the temperatures and loading rates for 9.5 mm NMAS. The graphs plotted for each set were the average fracture energy obtained and the maximum and minimum standard deviation values for each of them. When comparing the graphs with Figure 4.8, a similar trend can be found were the global parabola start increasing until reaches a peak value and then decreases. Also, for 25 mm PG 64-22, a parabolic shape is obtained from the maximum local fracture energy values. However, for 25 mm PG 76-22, shown in Figure 4.14b, the parabola is closer to a straight line that increases slightly with the testing temperature which means that the aggregate is dominating the fracture energy behavior in comparison with the binder. In 2019, Espinosa et al. performed a study where the fracture energy was evaluated depending on the three NMAS: 4.75, 9.5, and 12.5 mm, and the calculation of the ligament fracture area. This study found that the gradation has a significant effect on the fracture energy (Espinosa *et al.*, 2019). In comparison with this research, the NMAS used has a gap of 15.5 mm which is higher than the ones tested on the Espinosa et al. study. However, we can anticipate that the 25 mm NMAS could affect the fracture energy more when combined with a stiffer binder as PG 76-22.

The purpose of building the parabolic function is to be able to predict fracture energy at any given testing temperature assuming the maximum fracture energy for a wide range of loading rates at that temperature. The following are the second-degree equations obtained from the fitted global average parabolas that were used to plot the parabolas in Figure 4.15:

9.5 mm NMAS PG 64-22 Global Average Parabola

$$Fracture\ Energy = -5.8936\, Temp^2 + 111.71\, Temp + 3076.8 \qquad \text{(Eq. 4.2)}$$

9.5 mm NMAS PG 76-22 Global Average Parabola

$$Fracture\ Energy = -7.1204\, Temp^2 + 93.366\, Temp + 4416.5 \qquad \text{(Eq. 4.3)}$$

25 mm NMAS PG 64-22 Global Average Parabola

$$Fracture\ Energy = -3.3047\,Temp^2 + 50.841\,Temp + 1928.7 \qquad \text{(Eq. 4.4)}$$

25 mm NMAS PG 76-22 Global Average Parabola

$$Fracture\ Energy = -1.0012\,Temp^2 + 67.238\,Temp + 1706.7 \qquad \text{(Eq. 4.5)}$$

Figure 4.15 displays the four final average global fracture energy parabolas calculated from the second-degree equation generated from the fitted parabolas. For the 9.5 mm NMAS, the parabolas follow a similar trending of a parabolic shape but the global fracture energy for PG 76-22 binder has a higher fracture energy value for all the testing temperatures except for 25 °C. For the 25 mm NMAS, the parabola for PG 64-22 kept the parabolic trend, but for the PG 76-22 binder type had a straight line that increases with the testing temperature. This behavior could mean that the maximum global fracture energy for this combination may be in higher testing temperatures and loading rates.

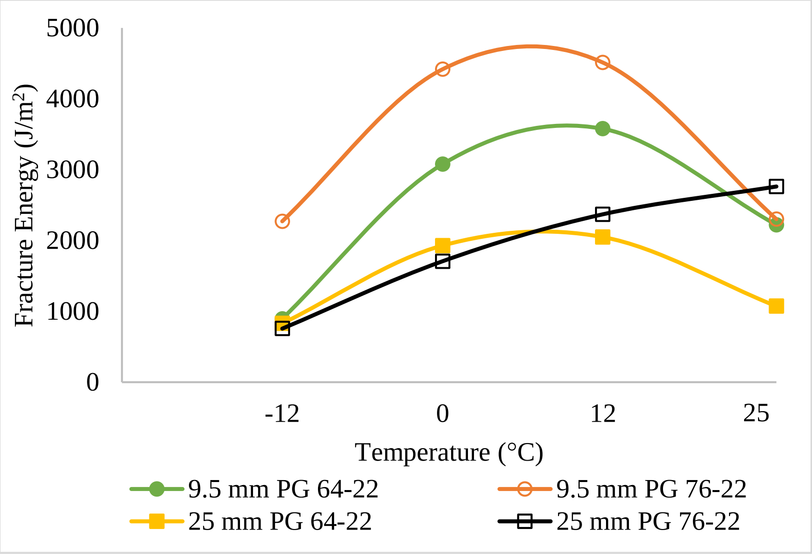

Figure 4.15 Global Fracture Energy Parabolas

From the second-degree equation, the first derivate was calculated to obtain the maximum value from the global fracture energy fitted parabola, which is shown in Table 4.4. The results from the global fitted parabola for 9.5 NMAS, the peak fracture energy obtained was 3,611 J/m^2 for PG 64-22 at 10 ˚C and 4,723 J/m^2 for PG 76-22 at 7 ˚C. For 25 mm NMAS, the peak fracture energy obtained was 2,118 J/m^2 for PG 64-22 at 7˚C and 2,762 J/m^2 for PG 76-22 at 25 ˚C. In 2017, Yang et al. performed a study in which the 9.5 mm and 25 mm NMAS were used with two testing temperatures: 0 and -24°C and two binder types: PG 64-22 and PG 76-22. The authors found that the testing temperature was very significant on fracture energy and at 0°C the higher values were obtained. Other findings were the dominance of 25 mm NMAS and PG 76-22 on fracture energy (Yang *et al.*, 2017b). In comparison with the local fracture energy, the global fracture energy is also dominated by the modified polymer but by 9.5 mm NMAS instead of the 25 mm NMAS. As previously mentioned, the 25 mm NMAS parabola for PG 76-22 may not be completely captured due to the amount of testing temperatures and loading rates performed. Therefore, the 9.5 mm NMAS is influencing both the local and the global fracture energy in this study.

Table 4.4 Maximum Global Fracture Energy values from fitted parabolas

Fracture Energy (J/m^2)							
9.5 mm				25 mm			
PG 64-22	Temp °C	PG 76-22	Temp °C	PG 64-22	Temp °C	PG 76-22	Temp °C
3611	10	4723	7	2118	7	2762	25

4.4 ANOVA Analysis

An ANOVA analysis was performed because general trends from the fitted local and global parabolas may not be visible in the parabolas because the majority of fracture energy looks to be different between the factors. Therefore, three factors were analyzed such as binder type, NMAS and loading rate at four temperatures: -12, 0, 12 and 25 °C as shown in summary in Table 4.5. As a result, for all the testing temperatures, the loading rate is a significant factor that affects the fracture energy. At -12 °C the binder type is a significant factor, and at 0 °C, the NMAS is a significant factor. After performing an analysis per each testing temperature, a single ANOVA analysis was made for each of the local fracture energy to determine the effect of loading rate in fracture energy. From the sixteen analysis, only four of the loading rate p-values from the local fracture energy are significant as shown in Table 4.6. This means that the fracture energy from the majority of the local parabolas are not significant in comparison with the fracture energy from the testing temperature from the global parabolas. The full ANOVA tables can be found in Appendix B.

Table 4.5 P-Value Summary of ANOVA for Fracture Energy

p-value	**Temperature (°C)**			
	-12	**0**	**12**	**25**
Binder Type	**0.0496**	0.0744	0.3753	0.4687
NMAS	0.7151	**0.0135**	0.0894	0.4466
Loading Rate	**0.0284**	**0.0179**	**0.0095**	**0.0001**

Table 4.6 Analysis of Variance of Fracture Energy for Loading Rate at different temperatures

Temperature °C	NMAS mm	Binder Type	p-value
			Loading Rate (mm/min)
-12	9.5	PG 64-22	0.8444
		PG 76-22	0.5808
	25	PG 64-22	0.1859
		PG 76-22	**0.0417**
0	9.5	PG 64-22	**0.0479**
		PG 76-22	0.0812
	25	PG 64-22	0.0950
		PG 76-22	0.8794
12	9.5	PG 64-22	0.1835
		PG 76-22	0.0829
	25	PG 64-22	0.8638
		PG 76-22	0.1093
25	9.5	PG 64-22	**0.0497**
		PG 76-22	0.1947
	25	PG 64-22	**0.0021**
		PG 76-22	0.2789

4.5 Conclusions

The objective of Chapter 4 was to evaluate the fracture energy at multiple temperatures (-12, 0, 12, 25 ˚C) using different loading rates (0.03, 0.5, 1.0, 30.0, and 50.0 mm/min) with two binder types (PG 64-22 and PG 76-22) and two NMAS (9.5 and 25 mm). A 50-mm thickness and a semi-circular notch configuration were kept constant for this chapter.

The conclusions from this chapter are the following:

- After plotting the master curve following the steps from a Dynamic Modulus |E*|, the graphs did not have an S-shaped. This could be because the cracking behavior may not be described using a sigmoidal function. However, a parabolic shaped was found when analyzing fracture energy versus loading rate.

- Two new concepts were defined from the parabolic behavior found in the fracture energy analysis. First, the "local" fracture energy which is the parabolic shape found on a specific testing temperature versus the loading rates. Also, the "global" fracture energy which is the parabolic shape found in all the combinations of four testing temperatures and five loading rates.
- For both local and global fracture energy parabola, a 9.5 mm NMAS and the polymer-modified binder looks to dominate the fracture behavior. From all the combinations, 25 mm PG 76-22 was the only that did not follow a parabolic trending, this could be because the gradation influences fracture energy. Also, the maximum fracture energy value may be obtained at a higher temperature than 25°C and loading rates.

4.6 References

AASHTO (2013). Standard Method of Test for Determining the Fracture Energy of Asphalt Mixtures Using the Semicircular Bend Geometry (SCB). TP 105-13. Washington D.C. Fracture Toughness of Asphalt Concrete Materials. *13th International Conference on Fracture.*

AASHTO (2013). Standard Practice for Developing Dynamic Modulus Master Curves for Asphalt Mixtures. *R 62-13.* Washington D.C.

AASHTO (2016). Determining the Fracture Potential of Asphalt Mixtures Using the Flexibility Index Test (FIT). TP 124-16. Washington D.C.

Al-Qadi, I., Ozer, H., Lambros, J., Khatib, A., Singhvi, P., Khan, T., Rivera-Perez, J., Doll, B. (2015). Testing Protocols to Ensure Performance of High Asphalt Binder Replacement Mixes Using RAP and RAS. Report FHWA-ICT-15-017.

Aragão, F., Kim, Y. (2012). Mode I Fracture Characterization of Bituminous Paving Mixtures at Intermediate Service Temperatures. *Experimental Mechanics*, 52, pp. 1423-1434.

Bayane, B., Yang, E., Yanjun, Q. (2017). Dynamic Modulus Master Curve Construction Using Christensen-Anderson-Marasteanu (CAM) Model. *International Journal of Engineering Research and Application*, 7 (1), pp. 53-63.

Chadbourn, B., Skok, Jr., Newcomb, D., Crow, B., Spindler, S. (1999). The Effect of Voids in Mineral Aggregate (VMA) on Hot-Mix Asphalt Pavements. Report MN/RC – 2000-13.

Clyne, T., Li, X., Marasteanu, M., Skok, E. (2003). Dynamic and Resilient Modulus of Mn/DOT Asphalt Mixtures. Report MN/RC – 2003-09.

Cooper III, S., King, W., Kabir, S. (2016). Testing and Analysis of LWT and SCB Properties of Asphalt Concrete Mixtures. *Louisiana Department of Transportation and Development.* FHWA-LA-536.

Espinosa, L., Wills, J., Caro, S., Braham, A. (2019). Influence of the Morphology of the Cracking Zone on the Fracture Energy of HMA Materials. *Materials and Structures,* 52 (35).

Fakhri, M., Kharrazi, E., Aliha, M. (2018). The Effect of Loading on Fracture Energy of Asphalt Mixture at Intermediate Temperatures and Under Different Loading Modes. *Frattura ed Integrita Strutturale,* 43, pp 113-132.

Kim. Y., Seo, Y., King, M, Momen, M. (2004). Dynamic Modulus Testing of Asphalt Concrete in Indirect Tension Mode. *Transportation Research Record: Journal of the Transportation Research Board,* 1891, pp. 163-173.

Li, X., Marasteanu, M. (2004). Evaluation of the Low Temperature Fracture Resistance of Asphalt Mixtures Using the Semi-Circular Bend Test. *Asphalt Paving Technology: Association of Asphalt Paving Technologists- Proceedings of the Technical Sessions.* 73, pp. 401-426.

Li., X., Marasteanu, M. (2010). Using Semi Circular Bending Test to Evaluate Low Temperature Fracture Resistance for Asphalt Concrete. *Experimental Mechanics* (50), pp 867-876.

Papagiannakis, A., Masad, E. (2008). Pavement Design and Materials. *John Wiley & Sons, Inc.* NJ.

Perez-Jimenez, F., Valdes, G., Miro, R., Martinez, A., Botella, R. (2010). Development of a New Test Procedure for Evaluating Cracking Resistance in Bituminous Mixtures. *Transportation Research Record: Journal of the Transportation Research Board,* 2181, pp. 36-43.

Yang, S., Braham, A., Underwood, S., Hanz, A., Reinke, G. (2017a). Correlating Field Performance to Laboratory Dynamic Modulus from Indirect Tension and Torsion Bar. *Road Materials and Pavement Design,* 8 (1), pp. 104-127.

Yang, S., Braham, A. (2017b). Influence of Binder Grade, Gradation, Temperature and Loading Rate on R-Curve of Asphalt Concrete. *Construction and Building Materials,* 154, pp. 780-790.

Zhou, F., Newcomb, D., Gurganus, C., Banihashemrad, Park, E., Sakhaeifar, M., Lytton, R. (2016). Experimental Design for Field Validation of Laboratory Tests to Assess Cracking Resistance of Asphalt Mixtures. *NCHRP09-57.*

Zhu, Y., Dave, E., Rahbar-Rastegar, R., Daniel, J., Zofka, A. (2017). Comprehensive Evaluation of Low-Temperature Fracture Indices for Asphalt Mixtures. *Road Materials and Pavement Design.*

Chapter 5 Conclusions and Recommendations

5.1 Review of chapter objectives

Cracking is one of the principal distresses that have more effect on asphalt pavements, therefore, multiple research studies have been done to understand the cracking behavior. Fracture mechanics can be applied to multiple engineering fields and since the 1960s have been applied to asphalt concrete. Several fracture tests have been developed to evaluate cracks using different geometries and one of the most popular is the Semi-Circular Bend (SC(B)). Although there are many fracture tests used to obtain fracture energy, the AASHTO TP 105 was the main one used for this study. These fracture tests that use an SC(B) geometry have different parameters such as thickness, testing temperature, and loading rates. Thus, this study looks to evaluate those parameters by applying fracture mechanics concepts and time-temperature superposition, which will give a better understanding of fracture resistance behavior.

To apply fundamental fracture mechanics concepts, three objectives were applied in this study. First, to evaluate the interaction of four asphalt properties factors: NMAS (9.5 and 25 mm), binder grade (PG 64-22 and PG 76-22), loading rate (0.03 and 1.00 mm/min), and temperature (-24 and 0 °C) through ASTM E1169 ruggedness test and compare fracture energy vs. flexibility index results. Then, the results obtained from the ruggedness test were used to set the experimental matrix to enhance the test procedure of AASHTO TP 105 by assessing that fundamental fracture mechanics concepts are applied to the specification by evaluating three thicknesses: 25, 50 and 100 mm, and three notch configurations: rectangular, semi-circular and fatigue pre-cracked, from the SC(B) geometry. Finally, the thickness and notch configuration selected were used to evaluate the fracture behavior by performing AASHTO TP 105 test using four temperatures: -12, 0, 12, 25 ˚C and five loading rates 0.03, 0.5, 1.0, 30.0, and 50.0 mm/min, and with those results to develop a master curve to analyze fracture energy by plotting fracture energy versus loading rate at different temperatures.

5.2 Conclusions

A ruggedness test was performed to evaluate the effects of asphalt properties factors which may affect the performance of asphalt concrete. These factors were evaluated by making a comparison between fracture energy and flexibility index. Then, these results were used to evaluate if proper fracture mechanics concepts were applied to the thicknesses and notch configurations used in the SC(B) test methods. Finally, with the thickness and notch configuration selected, the concept of time-superposition was applied to evaluate the fracture energy at multiple temperatures, using different loading rates to characterize cracking behavior.

Using the ruggedness test method, it was found that the fracture energy and flexibility index had different parameters that affect their results. This has to do with how sensitive those results are depending on an applied factor. For instance, post-peak slope (m), a flexibility index parameter, can be sensitive to temperature, loading rate, and the low PG temperature. On both fracture energy and flexibility index, testing temperature had the most significant effect. However, the loading rate did not have a significant effect on fracture energy. Since asphalt concrete is a viscoelastic material, testing temperature and loading rate relate to each other. A wider range for loading rate and testing temperature were later considered to evaluate the results. Finally, the other two factors, nominal maximum aggregate size (NMAS) and binder had a significant effect only on fracture energy. The influence of the aggregate size appears to become significant between an NMAS difference of 6 mm and 15.5 mm.

Moreover, when evaluating the factors of thickness, notch configuration, and temperature, thickness had a significant effect on fracture energy for an ANOVA factorial design. Notch configuration and temperature did not affect but their interaction with the thickness did influence the fracture energy. The reason for the notch configuration and testing temperature not being significant could be due to the smaller range between the low temperatures tested. In this study, the thickness was evaluated by looking at the representative volume element (RVE) and plain strain. Several factors affect the RVE in an asphalt concrete sample which could be the area of fraction, gradation, orientation and the maximum aggregate size from the mixture. Therefore, a gauge length of 50-60 mm thickness was recommended to be used for a 12.5 mm NMAS since it is the smallest size needed to represent RVE requirements in asphalt concrete. After applying the calculation for plane strain fracture toughness, a 46 mm thickness was found to be appropriate to represent the true material of asphalt concrete.

Since fracture tests are usually performed on notched specimens, most of the fracture test in asphalt concrete uses a rectangular notch; however, this notch forces the crack to occur in a specific zone. From the results, the rectangular notch had a lower angle direction for crack initiation in comparison with the other notch configurations which means that it has less possibility to build a cohesive zone. A semi-circular notch configuration showed to let the crack to initiate from a wider range in comparison with the rectangular notch. Hence, this notch configuration was selected to continue with more analysis of crack initiation.

After selecting a thickness and notch configuration, a master curve was plotted following the steps from a Dynamic Modulus |E*|, the graphs did not follow the S-shaped from the sigmoidal function expected. This could be because the cracking behavior may not be described using a sigmoidal function, but a parabolic function when plotting fracture energy versus loading rate. Two concepts were defined from the parabolic behavior found in the fracture energy analysis. First, the “local” fracture energy which is the parabolic shape found on a specific testing temperature versus the loading rates. Also, the "global" fracture energy which is the parabolic shape found in all the combinations of four testing temperatures. These parabolas were built using a second-degree parabolic function. The results obtained from the global fitted parabola for 9.5 NMAS, the peak fracture energy obtained was 3,611 J/m^2 for PG 64-22 at 10 ˚C and 4,723 J/m^2 for PG 76-22 at 7 ˚C. For 25 mm NMAS, the peak fracture energy obtained was 2,118 J/m^2 for PG 64-22 at 7˚C and 2,762 J/m^2 for PG 76-22 at 25 ˚C. For both local and global fracture energy, the 9.5 mm NMAS and the polymer modified binder dominated the fracture behavior. However, for the global fracture energy parabola at 25 mm NMAS using a modified binder PG 76-22, the fracture energy started increasing until it reaches a peak at 25 ˚C without following a shape of a parabola. This could be due to the shape of the parabola is not completed with the testing temperatures and loading rates performed on this study.

5.3 Recommendations

Multiple fracture tests have been used to capture the fracture behavior and most of them use an SC(B) geometry. However, from these tests, different parameters have been used such as thickness, testing temperature, and loading rates. This study looked to evaluate those and other factors by applying fracture mechanics and time-superposition. When performing the research, some recommendations were encountered that need to be addressed in future studies.

During the analysis of the ruggedness test, the loading rate tested did not affect the fracture energy but influenced the flexibility index. For this reason, a wider range of loading rates may be used to determine if there is or still not an effect on the fracture energy.

Furthermore, when looking at the thickness analysis, NMAS is one of the factors that has more influence in the RVE, multiple studies must be made to determine the optimum thickness depending on the NMAS for SC(B) tests. Also, when calculating the optimal thickness by applying fracture mechanics concepts of plain strain, the value of yield stress and Poisson’s ratio was assumed because asphalt concrete is a viscoelastic material and several properties are not given for the material. For the notch configuration, a 1 in diameter for the semi-circular notch configuration was cored but may be more practical to reduce the diameter because the knives would be glued completely to the asphalt sample for a 10-mm separation according to the AASHTO TP 105 specification.

Finally, when applying the time-temperature superposition and following the Dynamic Modulus |E*| steps to develop a master curve, the plots did not follow a consistency or similarities with each other or the actual Dynamic Modulus |E*| master curve. However, a parabolic trending was shown when plotting the fracture energy for each loading rate. This means that this shape may be better to describe the cracking behavior instead of mimicking the Dynamic Modulus |E*|. Therefore, more testing temperatures and loading rates must be evaluated for different NMAS to compare if there is a parabolic behavior and to determine if there is a peak fracture energy value for the 25 mm NMAS using a PG 76-22 binder type.

Appendix A Tables from Chapter 3

Table A.1 Plane Strain Thickness Calculations at - 24°C

Notch Configuration	a	r	P	t	Yi	Yield	K_I	B	Average B
	mm	mm	KN	mm	-	MPa	MPa * $m^{0.5}$	mm	mm
Rectangular	18.0	74.1	2.68	25	5.40	0.71	0.91	51.61	**45.28**
Rectangular	17.4	73.4	2.57	23	5.38	0.75	0.94	55.03	
Rectangular	18.0	73.7	2.96	27	5.41	0.74	0.94	55.36	
Rectangular	20.3	74.7	1.84	25	5.51	0.50	0.69	29.72	
Rectangular	17.1	73.7	2.54	25	5.37	0.69	0.86	45.56	
Semi-Circular	13.7	76.8	1.43	24	5.20	0.38	0.41	10.49	
Semi-Circular	12.2	76.8	3.91	27	5.15	0.95	0.96	56.61	
Semi-Circular	12.4	75.4	3.30	25	5.17	0.87	0.89	48.82	
Semi-Circular	12.4	74.9	3.27	26	5.17	0.84	0.86	45.40	
Pre-Cracked	17.7	73.7	2.75	25	5.39	0.73	0.93	54.17	
Rectangular	14.3	73.9	5.84	50	5.25	0.79	0.87	47.24	**45.94**
Rectangular	14.3	74.2	5.45	49	5.24	0.74	0.83	42.28	
Rectangular	15.3	74.0	5.76	50	5.28	0.78	0.90	50.16	
Rectangular	14.3	75.2	5.52	50	5.23	0.74	0.82	41.42	
Semi-Circular	12.4	75.0	5.04	50	5.17	0.67	0.68	28.96	
Semi-Circular	12.1	77.1	6.53	50	5.15	0.84	0.84	44.22	
Semi-Circular	12.4	76.0	6.02	50	5.16	0.79	0.80	40.13	
Semi-Circular	11.8	75.1	6.99	51	5.15	0.92	0.91	51.60	
Pre-Cracked	14.6	75.6	5.94	50	5.24	0.78	0.87	47.45	
Pre-Cracked	15.8	75.5	5.70	51	5.29	0.75	0.88	47.93	
Pre-Cracked	14.8	74.8	6.76	51	5.26	0.89	1.02	63.92	
Rectangular	14.4	74.9	13.26	104	5.24	0.85	0.95	55.75	**46.16**
Rectangular	12.1	73.1	12.87	105	5.17	0.84	0.85	44.57	
Rectangular	15.5	75.7	13.70	105	5.28	0.86	1.01	62.90	
Semi-Circular	9.8	74.1	13.10	104	5.09	0.85	0.76	35.69	
Semi-Circular	12.0	75.5	14.16	104	5.15	0.90	0.90	44.86	
Semi-Circular	10.5	74.6	14.12	103	5.11	0.92	0.85	48.98	
Pre-Cracked	14.5	78.4	12.97	104	5.22	0.80	0.89	49.31	
Pre-Cracked	11.8	72.3	13.55	105	5.16	0.90	0.89	36.69	
Pre-Cracked	13.1	74.1	11.32	105	5.20	0.73	0.77	36.69	

Table A.2 Plane Strain Thickness Calculations at - 12°C

Notch Configuration	a	r	P	t	Yi	Yield	Ki	B	Average B
	mm	mm	KN	mm	-	MPa	Mpa * $m^{0.5}$	mm	mm
Rectangular	18.7	75.3	2.52	25	5.42	0.66	0.87	46.76	**47.00**
Rectangular	18.7	74.8	2.52	27	5.43	0.63	0.83	42.57	
Rectangular	18.3	74.3	2.29	28	5.42	0.55	0.72	31.82	
Semi-Circular	15.2	74.8	2.80	24	5.27	0.77	0.88	48.51	
Semi-Circular	13.5	72.5	3.31	28	5.22	0.82	0.89	48.85	
Semi-Circular	13.3	73.5	4.00	27	5.21	1.02	1.08	72.97	
Pre-Cracked	17.6	73.3	2.29	26	5.39	0.60	0.77	36.38	
Pre-Cracked	18.0	73.5	2.75	25	5.41	0.74	0.95	55.96	
Pre-Cracked	17.9	74.0	2.31	25	5.40	0.62	0.80	39.22	
Rectangular	14.4	74.8	7.02	50	5.24	0.94	1.05	68.24	**47.55**
Rectangular	14.4	74.2	5.52	50	5.25	0.75	0.83	43.10	
Rectangular	14.4	76.0	5.79	50	5.23	0.76	0.85	44.39	
Rectangular	14.6	75.1	6.46	51	5.25	0.85	0.96	56.88	
Semi-Circular	11.8	75.3	6.61	51	5.15	0.87	0.86	46.19	
Semi-Circular	12.0	75.5	6.59	51	5.15	0.86	0.86	45.76	
Semi-Circular	12.0	73.9	7.13	50	5.16	0.96	0.96	57.34	
Pre-Cracked	13.9	74.1	5.41	50	5.23	0.72	0.79	38.82	
Pre-Cracked	14.7	73.0	4.66	51	5.27	0.62	0.70	30.68	
Pre-Cracked	14.6	74.4	5.76	50	5.25	0.77	0.86	46.18	
Pre-Cracked	14.4	73.7	5.73	51	5.25	0.77	0.86	45.48	
Rectangular	13.5	74.4	11.94	105	5.21	0.77	0.82	42.06	**44.37**
Rectangular	14.8	73.1	12.66	104	5.27	0.83	0.95	55.65	
Rectangular	11.8	73.4	13.28	104	5.16	0.87	0.87	46.52	
Semi-Circular	13.8	74.3	13.79	104	5.22	0.90	0.97	58.77	
Semi-Circular	13.2	75.8	13.31	104	5.19	0.85	0.89	49.52	
Semi-Circular	13.8	74.9	7.12	103	5.22	0.46	0.50	15.51	
Pre-Cracked	12.2	71.8	12.46	105	5.18	0.83	0.84	43.86	
Pre-Cracked	12.7	75.0	11.99	104	5.18	0.77	0.80	39.44	
Pre-Cracked	13.9	75.6	12.67	104	5.22	0.81	0.88	47.99	

Table A.3 General Factorial Design Matrix

Source of Variation	Sum of Squares	Degree of Freedom	
A (Thickness)	$SS_A = \frac{1}{bcn}\sum_{i=1}^{a} y_{i....}^2 - \frac{y_{.....}^2}{abcn}$	$a - 1$	2
B (Notch Configuration)	$SS_B = \frac{1}{acn}\sum_{i=1}^{b} y_{.j...}^2 - \frac{y_{.....}^2}{abcn}$	$b - 1$	2
C (Temperature)	$SS_C = \frac{1}{abn}\sum_{i=1}^{b} y_{..k..}^2 - \frac{y_{.....}^2}{abcn}$	$c - 1$	1
AB	$SS_{AB} = \frac{1}{cn}\sum_{i=1}^{a}\sum_{j=1}^{b} y_{ij...}^2 - \frac{y_{.....}^2}{abcn} - SS_A - SS_B$	$(a-1)(b-1)$	4
BC	$SS_{BC} = \frac{1}{an}\sum_{j=1}^{b}\sum_{k=1}^{c} y_{.jk..}^2 - \frac{y_{.....}^2}{abcn} - SS_B - SS_C$	$(b-1)(c-1)$	2
AC	$SS_{AC} = \frac{1}{bn}\sum_{i=1}^{a}\sum_{k=1}^{c} y_{i.k..}^2 - \frac{y_{.....}^2}{abcn} - SS_A - SS_C$	$(a-1)(c-1)$	2
ABC	$SS_{ABC} = \frac{1}{n}\sum_{i=1}^{a}\sum_{j=1}^{b}\sum_{k=1}^{c} y_{ijk..}^2 - \frac{y_{.....}^2}{abcn} - SS_A - SS_B - SS_C - SS_{AB} - SS_{BC} - SS_{AC}$	$(a-1)(b-1)(c-1)$	4
Error	$SS_E = Subtraction$	$(abc-1)(n-1)$	36
Total	$SS_T = \sum_{i}\sum_{j}\sum_{k}\sum_{l}\sum_{m} y_{ijklm}^2 - \frac{y_{.....}^2}{abcn}$	$(abcn-1)$	53

Appendix B Tables, Equations and Figures from Chapter 4

Table B.1 Initial Fracture Energy values to fit parabolas

Temperature °C	Loading Rate (mm/min)	Fracture Energy (J/m^2)			
		9.5 mm		25 mm	
		PG 64-22	PG 76-22	PG 64-22	PG 76-22
-12	0.03	967	1248	1111	2571
-12	0.5	1216	1506	1217	1475
-12	1.0	763	1938	797	1334
-12	30.0	588	732	520	300
-12	50.0	693	306	248	1215
0	0.03	340	2578	2150	1341
0	0.5	1237	4746	2969	1107
0	1.0	3150	4711	346	1508
0	30.0	1045	2111	1344	654
0	50.0	1490	509	280	1361
12	0.03	1141	488	1268	965
12	0.5	2982	920	1641	1303
12	1.0	3275	1127	2181	2220
12	30.0	2980	2886	1530	2471
12	50.0	2394	3924	1507	2003
25	0.03	460	249	324	515
25	0.5	1352	461	1811	875
25	1.0	922	1354	547	1475
25	30.0	2288	2245	1037	2742
25	50.0	5038	2474	3004	1991

The following are the second-degree equations from the three fitted local 9.5 NMAS PG 64-22 parabolas, upper standard deviation, mean and lower standard deviation, in function of loading rate (LR) for each testing temperature which are plotted in Figure B.1:

-12°C Local Parabolas

$$Fracture\ Energy_{UpperStDev} = -1.3744\ LR^2 + 57.847\ LR + 1284.6 \quad \text{(Eq. B.1)}$$

$$Fracture\ Energy_{Mean} = -0.3093\ LR^2 + 12.653\ LR + 710.83 \quad \text{(Eq. B.2)}$$

$$Fracture\ Energy_{LowerStDev} = 0.4765\ LR^2 - 18.43\ LR + 130.1 \quad \text{(Eq. B.3)}$$

0°C Local Parabolas

$$Fracture\ Energy_{UpperStDev} = -4.4802\ LR^2 + 230.75\ LR + 913.05 \quad \text{(Eq. B.4)}$$

$$Fracture\ Energy_{Mean} = -4.0176\ LR^2 + 213.29\ LR + 409.33 \quad \text{(Eq. B.5)}$$

$$Fracture\ Energy_{LowerStDev} = -3.541\ LR^2 + 194.69\ LR - 73.199 \quad \text{(Eq. B.6)}$$

12 °C Local Parabolas

$$Fracture\ Energy_{UpperStDev} = -0.1217\ LR^2 + 59.433\ LR + 1912.3 \quad \text{(Eq. B.7)}$$

$$Fracture\ Energy_{Mean} = -1.8559\ LR^2 + 125.86\ LR + 1285.6 \quad \text{(Eq. B.8)}$$

$$Fracture\ Energy_{LowerStDev} = -3.5902\ LR^2 + 192.29\ LR + 658.9 \quad \text{(Eq. B.9)}$$

25 °C Local Parabolas

$$Fracture\ Energy_{UpperStDev} = 1.4148\ LR^2 - 5.1092\ LR + 1052.7 \quad \text{(Eq. B.10)}$$

$$Fracture\ Energy_{Mean} = 1.0404\ LR^2 - 18.668\ LR + 601.15 \quad \text{(Eq. B.11)}$$

$$Fracture\ Energy_{UpperStDev} = 0.2743\ LR^2 - 12.74\ LR + 154.55 \quad \text{(Eq. B.12)}$$

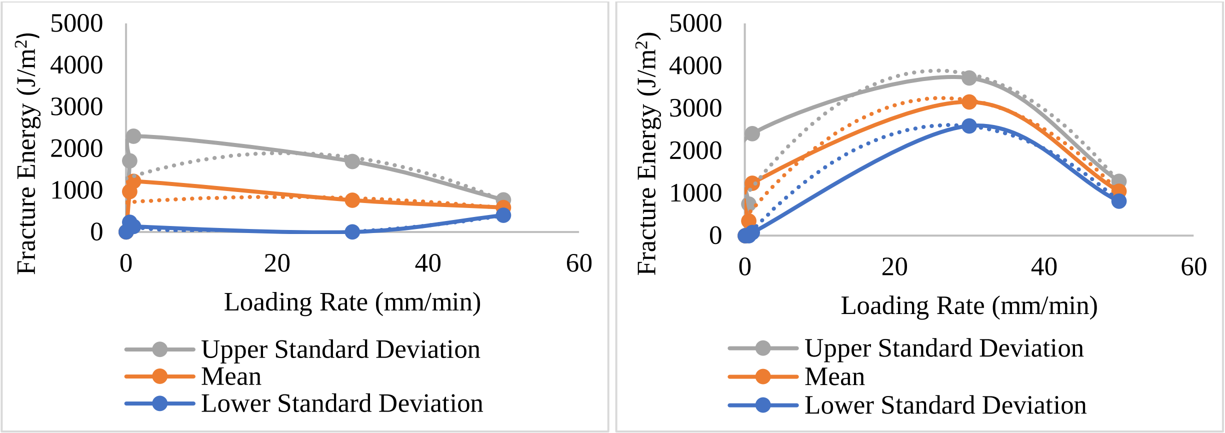

a) -12 °C **b) 0 °C**

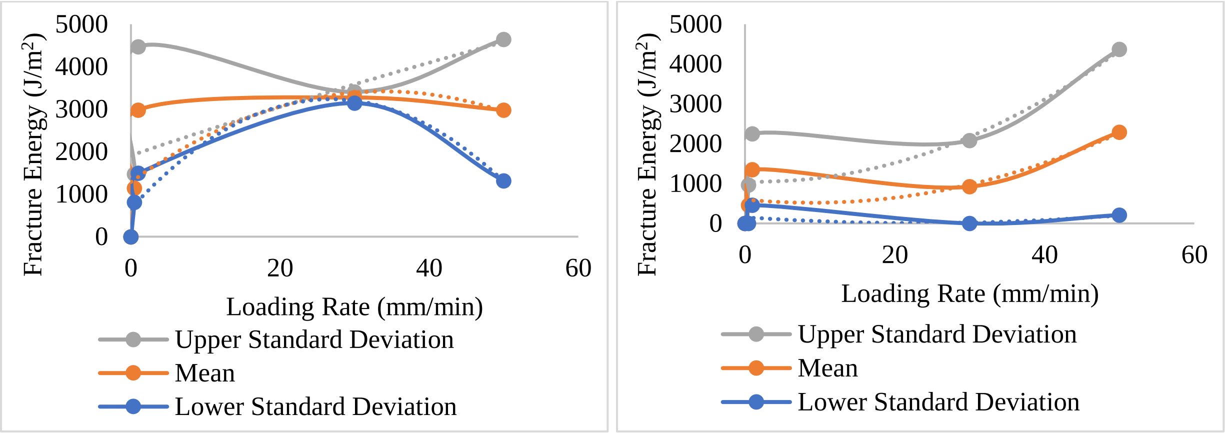

c) 12 °C **d) 25 °C**

Figure B.1 Local Parabola for 9.5 mm PG 64-22

The following are the second-degree equations from the three fitted local 9.5 NMAS PG 76-22 parabolas, upper standard deviation, mean, and lower standard deviation, in function of loading rate (LR) for each testing temperature which are plotted in Figure B.2:

-12°C Local Parabolas

$$Fracture\ Energy_{UpperStDev} = -2.4714\ LR^2 + 140.44\ LR + 1840.2 \quad \text{(Eq. B.13)}$$

$$Fracture\ Energy_{Mean} = -2.0428\ LR^2 + 99.246\ LR + 856.04 \quad \text{(Eq. B.14)}$$

$$Fracture\ Energy_{LowerStDev} = -0.275\ LR^2 + 13.89\ LR - 6.8536 \quad \text{(Eq. B.15)}$$

0°C Local Parabolas

$$Fracture\ Energy_{UpperStDev} = -8.1909\ LR^2 + 433.34\ LR + 2693.4 \quad \text{(Eq. B.16)}$$

$$Fracture\ Energy_{Mean} = -4.5879\ LR^2 + 224.51 LR + 2289.3 \quad \text{(Eq. B.17)}$$

$$Fracture\ Energy_{LowerStDev} = -0.9848\ LR^2 + 15.686\ LR + 1885.2 \quad \text{(Eq. B.18)}$$

12 °C Local Parabolas

$$Fracture\ Energy_{UpperStDev} = 1.8195\ LR^2 - 26.505\ LR + 770.78 \quad \text{(Eq. B.19)}$$

$$Fracture\ Energy_{Mean} = 1.2423\ LR^2 - 14.031\ LR + 467.98 \quad \text{(Eq. B.20)}$$

$$Fracture\ Energy_{LowerStDev} = 0.6651\ LR^2 - 1.557\ LR + 165.19 \quad \text{(Eq. B.21)}$$

25 °C Local Parabolas

$$Fracture\ Energy_{UpperStDev} = 0.197\ LR^2 + 62.179\ LR + 372.21 \quad \text{(Eq. B.22)}$$

$$Fracture\ Energy_{Mean} = 0.0966\ LR^2 + 35.642\ LR + 214.98 \quad \text{(Eq. B.23)}$$

$$Fracture\ Energy_{LowerStDev} = -0.0038\ LR^2 + 9.1055\ LR + 57.753 \quad \text{(Eq. B.24)}$$

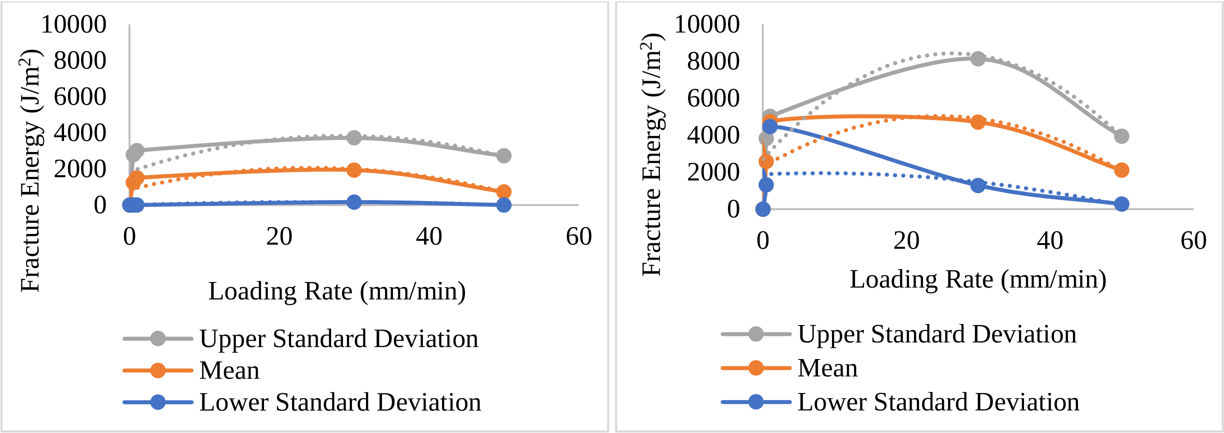

a) -12 °C **b) 0 °C**

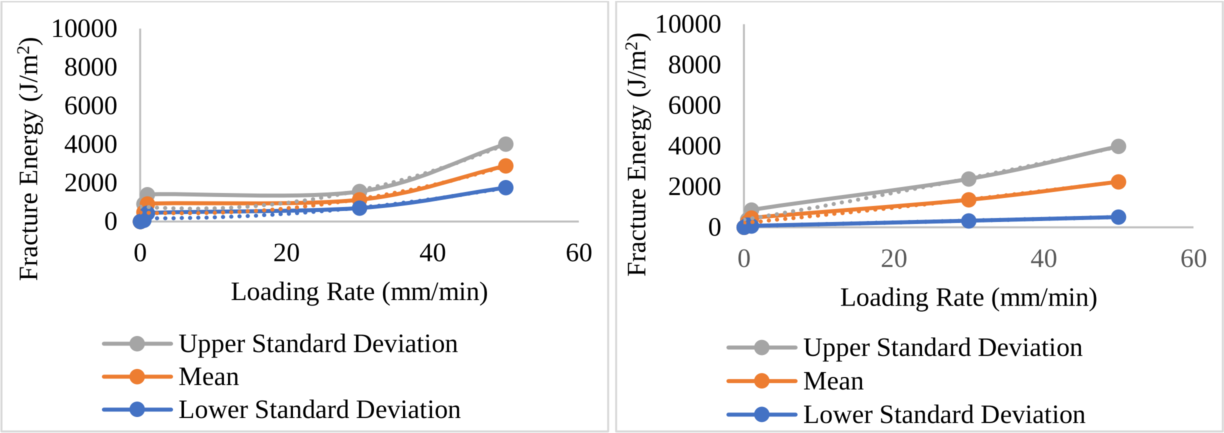

c) 12 °C **d) 25 °C**

Figure B.2 Local Parabola for 9.5 mm PG 76-22

The following are the second-degree equations from the three fitted local 25 NMAS PG 64-22 parabolas, upper standard deviation, mean, and lower standard deviation, in function of loading rate (LR) for each testing temperature which are plotted in Figure B.3:

-12°C Local Parabolas

$$Fracture\ Energy_{UpperStDev} = -0.4342\ LR^2 + 17.286\ LR + 1168.6 \quad \text{(Eq. B.25)}$$

$$Fracture\ Energy_{Mean} = -0.4021LR^2 + 14.99LR + 758.1 \quad \text{(Eq. B.26)}$$

$$Fracture\ Energy_{LowerStDev} = -0.3701\ LR^2 + 12.694\ LR + 347.61 \quad \text{(Eq. B.27)}$$

0°C Local Parabolas

$$Fracture\ Energy_{UpperStDev} = 3.4798\ LR^2 - 154.41\ LR + 2490.9 \quad \text{(Eq. B.28)}$$

$$Fracture\ Energy_{Mean} = 1.668\ LR^2 - 91.915LR + 1725.8 \quad \text{(Eq. B.29)}$$

$$Fracture\ Energy_{LowerStDev} = 0.4737\ LR^2 - 43.637\ LR + 967.55 \quad \text{(Eq. B.30)}$$

12 °C Local Parabolas

$$Fracture\ Energy_{UpperStDev} = -4.4021\ LR^2 + 228.04\ LR + 1283.5 \quad \text{(Eq. B.31)}$$

$$Fracture\ Energy_{Mean} = -1.6252\ LR^2 + 93.23\ LR + 909.23 \quad \text{(Eq. B.32)}$$

$$Fracture\ Energy_{LowerStDev} = 1.1517\ LR^2 - 41.578\ LR + 534.91 \quad \text{(Eq. B.33)}$$

25 °C Local Parabolas

$$Fracture\ Energy_{UpperStDev} = 0.7463\ LR^2 - 36.838\ LR + 1181.3 \quad \text{(Eq. B.34)}$$

$$Fracture\ Energy_{Mean} = 0.444\ LR^2 - 16.069LR + 703.66 \quad \text{(Eq. B.35)}$$

$$Fracture\ Energy_{LowerStDev} = 0.1417\ LR^2 + 4.6993\ LR + 226.04 \quad \text{(Eq. B.36)}$$

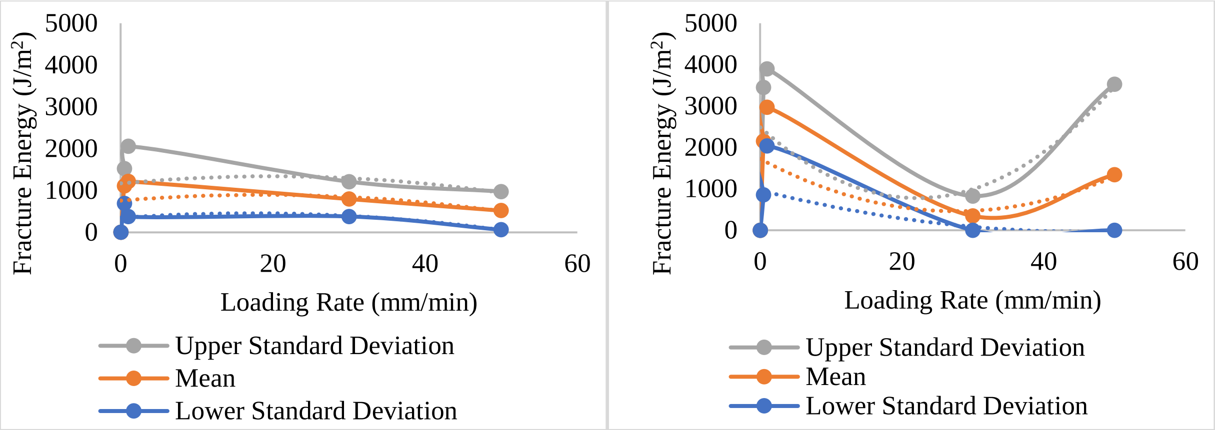

a) -12 °C **b) 0 °C**

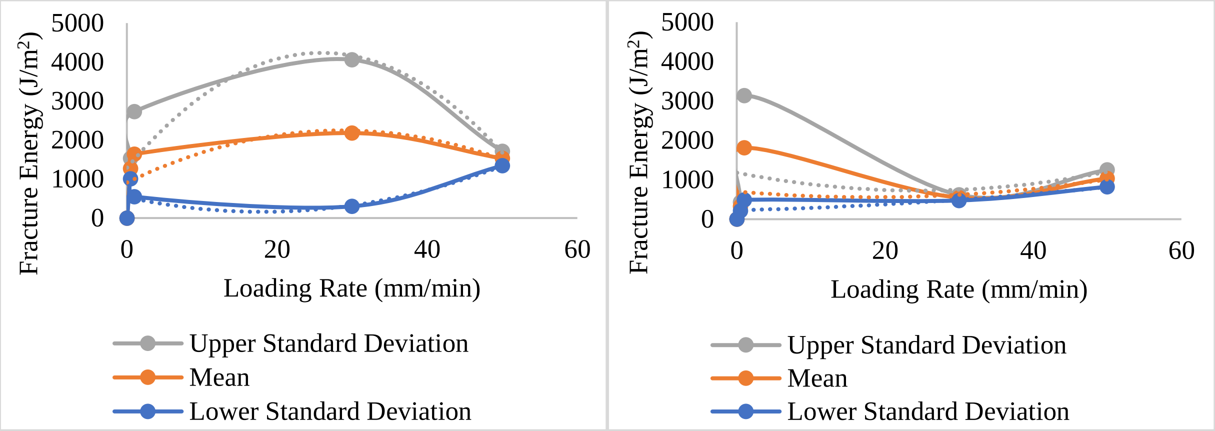

c) 12 °C **d) 25 °C**

Figure B.3 Local Parabola for 25 mm PG 64-22

The following are the second-degree equations from the three fitted local 25 NMAS PG 76-22 parabolas, upper standard deviation, mean, and lower standard deviation, in function of loading rate (LR) for each testing temperature which are plotted in Figure B.4:

-12°C Local Parabolas

$$Fracture\ Energy_{UpperStDev} = -2.3413\ LR^2 + 92.633LR + 1679.4 \quad \text{(Eq. B.37)}$$

$$Fracture\ Energy_{Mean} = -1.1623\ LR^2 + 37.344\ LR + 1317.7 \quad \text{(Eq. B.38)}$$

$$Fracture\ Energy_{LowerStDev} = 0.0168LR^2 - 17.945\ LR + 955.97 \quad \text{(Eq. B.39)}$$

0°C Local Parabolas

$$Fracture\ Energy_{UpperStDev} = -2.7539\ LR^2 + 128.15\ LR + 1434.2 \quad \text{(Eq. B.40)}$$

$$Fracture\ Energy_{Mean} = -1.4288\ LR^2 + 68.778LR + 772.63 \quad \text{(Eq. B.41)}$$

$$Fracture\ Energy_{LowerStDev} = -0.1038\ LR^2 + 9.4037\ LR + 111.06 \quad \text{(Eq. B.42)}$$

12 °C Local Parabolas

$$Fracture\ Energy_{UpperStDev} = 0.0447\ LR^2 + 51.473\ LR + 1023.1 \quad \text{(Eq. B.43)}$$

$$Fracture\ Energy_{Mean} = -0.8598\ LR^2 + 77.929\ LR + 705.94 \quad \text{(Eq. B.44)}$$

$$Fracture\ Energy_{LowerStDev} = -1.7644\ LR^2 + 104.39\ LR + 388.74 \quad \text{(Eq. B.45)}$$

25 °C Local Parabolas

$$Fracture\ Energy_{UpperStDev} = 1.9733\ LR^2 - 21.534\ LR + 701.83 \quad \text{(Eq. B.46)}$$

$$Fracture\ Energy_{Mean} = 0.5112\ LR^2 + 20.13\ LR + 445.55 \quad \text{(Eq. B.47)}$$

$$Fracture\ Energy_{LowerStDev} = -0.9511\ LR^2 + 61.794\ LR + 189.27 \quad \text{(Eq. B.48)}$$

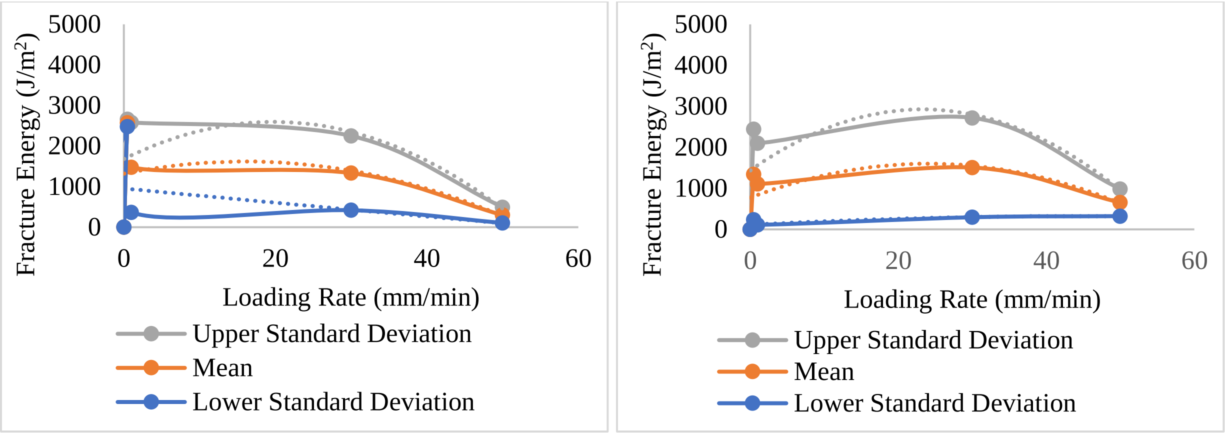

a) -12 °C **b) 0 °C**

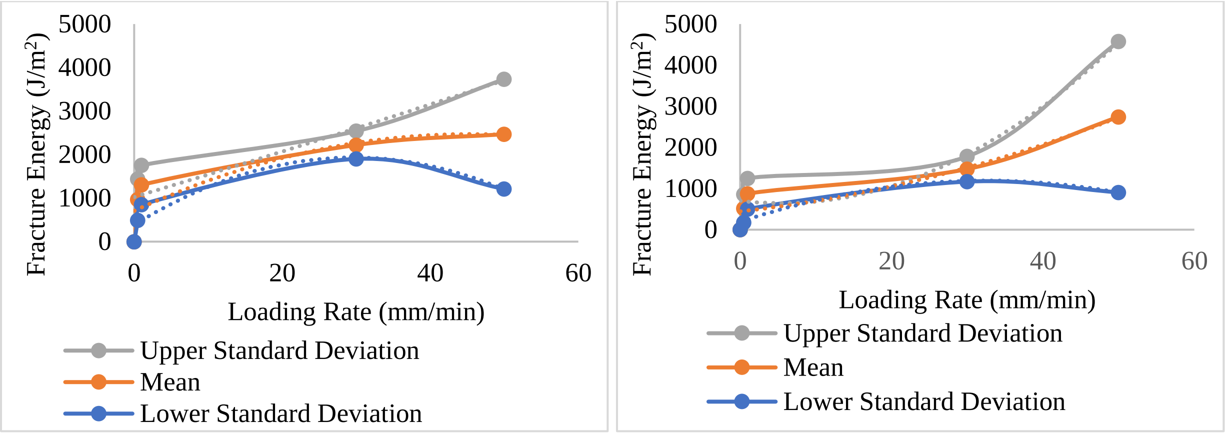

c) 12 °C **d) 25 °C**

Figure B.4 Local Parabola for 25 mm PG 76-22

The following are the second-degree equations obtained from the fitted upper and lower standard deviation parabolas that were used to plot the parabolas in Figure 4.15 from Chapter 4:

9.5 mm NMAS PG 64-22 Global Parabolas

$$Fracture\ Energy_{UpperStDev} = -3.752\ Temp^2 + 113.63\ Temp + 3819.1 \qquad \text{(Eq. B.49)}$$

$$Fracture\ Energy_{LowerStDev} = -8.5846\ Temp^2 + 110.99\ Temp + 2875.7 \qquad \text{(Eq. B.50)}$$

9.5 mm NMAS PG 76-22 Global Parabolas

$$Fracture\ Energy_{UpperStDev} = -8.414\ Temp^2 + 97.982\ Temp + 6778.9 \qquad \text{(Eq. B.51)}$$

$$Fracture\ Energy_{LowerStDev} = -6.2142\ Temp^2 + 93.51\ Temp + 2125.4 \qquad \text{(Eq. B.52)}$$

25 mm NMAS PG 64-22 Global Parabolas

$$Fracture\ Energy_{UpperStDev} = -8.4771\ Temp^2 + 112.17\ Temp + 3796.9 \qquad \text{(Eq. B.53)}$$

$$Fracture\ Energy_{LowerStDev} = -1.715 Temp^2 + 33.835\ Temp + 1073.3 \qquad \text{(Eq. B.54)}$$

25 mm NMAS PG 76-22 Global Parabolas

$$Fracture\ Energy_{UpperStDev} = 0.7531 Temp^2 + 44.501\ Temp + 2996.9 \qquad \text{(Eq. B.55)}$$

$$Fracture\ Energy_{LowerStDev} = -0.2961\ Temp^2 + 22.407\ Temp + 1028.8 \qquad \text{(Eq. B.56)}$$

Table B.2 Analysis of Variance of Fracture Energy at -12 °C

Source of Variation	**Sum of Squares**	**Degrees of Freedom**	**Mean Square**	**Fo**	**P-Value**
A, Binder Type	3058387.20	1	3058387.2	4.10	**0.0496**
B, NMAS	100770.93	1	100770.9	0.14	0.7151
C, Loading Rate	9037739.97	4	2259435.0	3.03	**0.0284**
AB	342734.78	1	342734.8	0.46	0.5018
AC	1903559.35	4	475889.8	0.64	0.6384
BC	2096548.86	4	524137.2	0.70	0.5947
ABC	2503807.56	4	625951.9	0.84	0.5085
Error	29834252.74	40	745856.3		
Total	48877801.39	59			

Table B.3 Analysis of Variance of Fracture Energy at 0 °C

Source of Variation	Sum of Squares	Degrees of Freedom	Mean Square	Fo	P-Value
A, Binder Type	5913805.04	1	5913805.0	3.36	0.0744
B, NMAS	11766358.38	1	11766358.4	6.68	**0.0135**
C, Loading Rate	23828506.64	4	5957126.7	3.38	**0.0179**
AB	10865769.03	1	10865769.0	6.17	**0.0173**
AC	3334988.36	4	833747.1	0.47	0.7551
BC	19374565.25	4	4843641.3	2.75	**0.0413**
ABC	23357501.92	4	5839375.5	3.31	**0.0195**
Error	70475739.31	40	1761893.5		
Total	168917233.92	59			

Table B.4 Analysis of Variance of Fracture Energy at 12 °C

Source of Variation	Sum of Squares	Degrees of Freedom	Mean Square	Fo	P-Value
A, Binder Type	1006133.27	1	1006133.3	0.80	0.3753
B, NMAS	3792340.51	1	3792340.5	3.03	0.0894
C, Loading Rate	19348793.00	4	4837198.3	3.86	**0.0095**
AB	2723973.42	1	2723973.4	2.18	0.1480
AC	10945280.03	4	2736320.0	2.19	0.0879
BC	5691674.28	4	1422918.6	1.14	0.3530
ABC	4788253.26	4	1197063.3	0.96	0.4419
Error	50062886.83	40	1251572.2		
Total	98359334.60	59			

Table B.5 Analysis of Variance of Fracture Energy at 25 °C

Source of Variation	Sum of Squares	Degrees of Freedom	Mean Square	Fo	P-Value
A, Binder Type	3058387.20	1	3058387.2	4.10	**0.0496**
B, NMAS	100770.93	1	100770.9	0.14	0.7151
C, Loading Rate	9037739.97	4	2259435.0	3.03	**0.0284**
AB	342734.78	1	342734.8	0.46	0.5018
AC	1903559.35	4	475889.8	0.64	0.6384
BC	2096548.86	4	524137.2	0.70	0.5947
ABC	2503807.56	4	625951.9	0.84	0.5085
Error	29834252.74	40	745856.3		
Total	48877801.39	59			

Table B.6 Analysis of Variance for Fracture Energy at -12 ºC, 9.5 mm PG 64-22

Source of Variation	**Sum of Squares**	**Degrees of Freedom**	**Mean Square**	**Fo**	**P-Value**
Loading Rate	745019.5796	4	186254.8949	0.34088512	0.8444
Error	5463861.096	10	546386.1096		
Total	6208880.676	14			

Table B.7 Analysis of Variance for Fracture Energy at -12 ºC, 9.5 mm PG 76-22

Source of Variation	**Sum of Squares**	**Degrees of Freedom**	**Mean Square**	**Fo**	**P-Value**
Loading Rate	4934834.842	4	1233708.71	0.7487564	0.5808
Error	16476770.77	10	1647677.077		
Total	21411605.61	14			

Table B.8 Analysis of Variance for Fracture Energy at -12 ºC, 25 mm PG 64-22

Source of Variation	**Sum of Squares**	**Degrees of Freedom**	**Mean Square**	**Fo**	**P-Value**
Loading Rate	1992576.38	4	498144.0951	1.9066817	0.1859
Error	2612623.219	10	261262.3219		
Total	4605199.6	14			

Table B.9 Analysis of Variance for Fracture Energy at -12 ºC, 25 mm PG 76-22

Source of Variation	**Sum of Squares**	**Degrees of Freedom**	**Mean Square**	**Fo**	**P-Value**
Loading Rate	7869224.938	4	1967306.235	3.7252549	**0.0417**
Error	5280997.65	10	528099.765		
Total	13150222.59	14			

Table B.10 Analysis of Variance for Fracture Energy at 0 ºC, 9.5 mm PG 64-22

Source of Variation	**Sum of Squares**	**Degrees of Freedom**	**Mean Square**	**Fo**	**P-Value**
Loading Rate	12999157.95	4	3249789.487	3.5343878	**0.0479**
Error	9194773.468	10	919477.3468		
Total	22193931.42	14			

Table B.11 Analysis of Variance for Fracture Energy at 0 ºC, 9.5 mm PG 76-22

Source of Variation	Sum of Squares	Degrees of Freedom	Mean Square	Fo	P-Value
Loading Rate	39379959.88	4	9844989.971	2.8571499	0.0812
Error	34457379.53	10	3445737.953		
Total	73837339.42	14			

Table B.12 Analysis of Variance for Fracture Energy at 0 ºC, 25 mm PG 64-22

Source of Variation	Sum of Squares	Degrees of Freedom	Mean Square	Fo	P-Value
Loading Rate	16175316.63	4	4043829.159	2.6661894	0.0950
Error	15167073.88	10	1516707.388		
Total	31342390.52	14			

Table B.13 Analysis of Variance for Fracture Energy at 0 ºC, 25 mm PG 76-22

Source of Variation	Sum of Squares	Degrees of Freedom	Mean Square	Fo	P-Value
Loading Rate	1341127.693	4	335281.9233	0.2876349	0.8794
Error	11656512.42	10	1165651.242		
Total	12997640.12	14			

Table B.14 Analysis of Variance for Fracture Energy at 12 ºC, 9.5 mm PG 64-22

Source of Variation	Sum of Squares	Degrees of Freedom	Mean Square	Fo	P-Value
Loading Rate	8720865.314	4	2180216.328	1.9206911	0.1835
Error	11351207.78	10	1135120.778		
Total	20072073.1	14			

Table B.15 Analysis of Variance for Fracture Energy at 12 ºC, 9.5 mm PG 76-22

Source of Variation	Sum of Squares	Degrees of Freedom	Mean Square	Fo	P-Value
Loading Rate	25840510.89	4	6460127.722	2.8308	0.0829
Error	22820855.32	10	2282085.532		
Total	48661366.2	14			

Table B.16 Analysis of Variance for Fracture Energy at 12 ºC, 25 mm PG 64-22

Source of Variation	Sum of Squares	Degrees of Freedom	Mean Square	Fo	P-Value
Loading Rate	1378654.875	4	344663.7187	0.311677	0.8638
Error	11058361.81	10	1105836.181		
Total	12437016.69	14			

Table B.17 Analysis of Variance for Fracture Energy at 12 ºC, 25 mm PG 76-22

Source of Variation	Sum of Squares	Degrees of Freedom	Mean Square	Fo	P-Value
Loading Rate	4833969.493	4	1208492.373	2.5007799	0.1093
Error	4832461.919	10	483246.1919		
Total	9666431.413	14			

Table B.18 Analysis of Variance for Fracture Energy at 25 ºC, 9.5 mm PG 64-22

Source of Variation	Sum of Squares	Degrees of Freedom	Mean Square	Fo	P-Value
Loading Rate	39803089.16	4	9950772.289	3.4874288	**0.0497**
Error	28533262.82	10	2853326.282		
Total	68336351.98	14			

Table B.19 Analysis of Variance for Fracture Energy at 25 ºC, 9.5 mm PG 76-22

Source of Variation	Sum of Squares	Degrees of Freedom	Mean Square	Fo	P-Value
Loading Rate	12195195.9	4	3048798.975	1.8569448	0.1947
Error	16418360.98	10	1641836.098		
Total	28613556.88	14			

Table B.20 Analysis of Variance for Fracture Energy at 25 ºC, 25 mm PG 64-22

Source of Variation	Sum of Squares	Degrees of Freedom	Mean Square	Fo	P-Value
Loading Rate	14238030.9	4	3559507.725	9.3605375	**0.0021**
Error	3802674.504	10	380267.4504		
Total	18040705.4	14			

Table B.21 Analysis of Variance for Fracture Energy at 25 ºC, 25 mm PG 76-22

Source of Variation	Sum of Squares	Degrees of Freedom	Mean Square	Fo	P-Value
Loading Rate	9428953.318	4	2357238.329	1.4826622	0.2789
Error	15898687.23	10	1589868.723		
Total	25327640.55	14			